

Fall November 2014

## Production of renewable chemicals and energy from waste biomass

Sheng Chu  
*Chemical Engineering*

Follow this and additional works at: [https://scholarworks.umass.edu/dissertations\\_2](https://scholarworks.umass.edu/dissertations_2)

 Part of the [Catalysis and Reaction Engineering Commons](#)

---

### Recommended Citation

Chu, Sheng, "Production of renewable chemicals and energy from waste biomass" (2014). *Doctoral Dissertations*. 169.  
<https://doi.org/10.7275/b7ck-a140> [https://scholarworks.umass.edu/dissertations\\_2/169](https://scholarworks.umass.edu/dissertations_2/169)

This Open Access Dissertation is brought to you for free and open access by the Dissertations and Theses at ScholarWorks@UMass Amherst. It has been accepted for inclusion in Doctoral Dissertations by an authorized administrator of ScholarWorks@UMass Amherst. For more information, please contact [scholarworks@library.umass.edu](mailto:scholarworks@library.umass.edu).

**PRODUCTION OF RENEWABLE CHEMICALS AND ENERGY FROM WASTE BIOMASS**

A Dissertation Presented

by

SHENG CHU

Submitted to the Graduate School of the  
University of Massachusetts Amherst in partial fulfillment  
of the requirements for the degree of

DOCTOR OF PHILOSOPHY

September 2014

Chemical Engineering

© Copyright by Sheng Chu 2014

All Rights Reserved

**PRODUCTION OF RENEWABLE CHEMICALS AND ENERGY FROM WASTE BIOMASS**

A Dissertation Presented

by

SHENG CHU

Approved as to style and content by:

---

Paul J. Dauenhauer, Chair

---

T.J. Mountziaris, Member

---

Wei Fan, Member

---

Erin Baker, Member

---

T.J. Mountziaris, Department Head  
Chemical Engineering

## DEDICATION

This thesis is dedicated to my parents and Yujie Liu.

## ACKNOWLEDGMENTS

I would like to thank my advisor, Paul J. Dauenhauer, for his thoughtful, patient guidance and for his advices on my career development. His enthusiasm on research is contagious. I want to thank my former advisor, George W. Huber, for bringing me into the research world of thermochemical conversion of biomass and also thank for his helpful instructions on my first project. I also would like to extend my gratitude to my committee members, T.J. Mountziaris, Wei Fan, and Erin Baker, for their insight comments and suggestions on my projects.

I would like to express my appreciation to Dr. Geoffrey Tompsett, who taught me how to conduct the lab work from simple tube cutting to complex reactor construction. You always gave me critical feedbacks on the research and I learned so much from you. I also would like to thank Dr. Ayyagari Subrahmanyam for giving me the instructions on organic synthesis. I am very grateful to Dr. Joungmo Cho for his helpful comments on my research.

I also would like to thank all my lab mates from Paul Dauenhauer's group and George Huber's group for bringing useful discussions and inspirations on my research. A special thank you to all those people from department of chemical engineering, chemistry, and polymer science who provided me with the useful suggestions.

## ABSTRACT

PRODUCTION OF RENEWABLE CHEMICALS AND ENERGY FROM WASTE BIOMASS

SEPTEMBER 2014

SHENG CHU, B.S., DALIAN UNIVERSITY OF TECHNOLOGY

Ph.D., UNIVERSITY OF MASSACHUSETTS AMHERST

Directed by: Professor Paul J. Dauenhauer

With the rapid growth of world population and developing industries, the production of wastes has dramatically increased in the past decades. Due to environmental concerns and limited landfill space, the disposal of wastes has been subjected to strict regulations. Beneficial uses of wastes such as recycling/reuse, land applications, energy production, and resource recovery have been advocated greatly. This thesis presents the utilization of two types of solid waste: lignin and waste paper/plastic. Through thermochemical conversion, wastes can be converted to chemicals and energy. This aims at reducing the energy dependence on fossil fuels while achieving effective waste management.

Lignin is the main byproduct from pulping and paper industry and is usually combusted to provide the heat for the pulping process. However, its poly-methoxylated phenylpropane structure makes lignin a potential natural source for phenolic and aromatic chemicals. Obtaining high yield of chemicals from lignin is a challenge due to its complex structure and unreactive nature. In this thesis, the pyrolysis behavior of lignin extracted from maple wood and a  $\beta$ -O-4 oligomeric lignin model compound is presented. Advanced analytical techniques were utilized to obtain a comprehensive characterization of pyrolysis products. The results show that carbon concentrated solid char is the major pyrolysis product for both extracted lignin and  $\beta$ -O-4 oligomeric lignin model compound. Reaction chemistry is proposed based on a free radical reaction mechanism.

Additionally, a new coal combustion technology utilizing Re-Engineered Feedstock™ (ReEF), was evaluated for pulverized coal combustion emission control. The ReEF consists of non-recyclable fibers/plastics and commercialized flue gas desulfurization (FGD) sorbent. This novel feedstock is combusted to produce energy while capturing the sulfur dioxide generated during coal combustion. It is demonstrated that up to 85% of sulfur dioxide reduction was achieved when co-firing coal with ReEF in a lab scale fluidized bed combustor. The kinetics of FGD sorbent in ReEF was studied in a drop tube reactor. The results show that combustion of waste fibers/plastics accelerates the sorbent sintering in ReEF which leads to a lower total sulfur uptake compared with pure FGD sorbent. However, the time of maximum reaction rate of sorbent sulfation is delayed in ReEF which indicates the ReEF can prevent the sorbent from early time sulfation. The application of ReEF will have positive impacts on the environment and society by supplementing coal combustion, reducing greenhouse gas emissions, and minimizing wastes that will go to landfill.

## TABLE OF CONTENTS

	Page
ACKNOWLEDGMENTS.....	v
ABSTRACT.....	vi
LIST OF TABLES.....	x
LIST OF FIGURES.....	xi
CHAPTER	
1. INTRODUCTION.....	1
1.1 World Energy Outlook .....	1
1.2 Waste Biomass: New Energy Resource.....	3
1.3 Thermochemical Conversion .....	6
2. PYROLYSIS OF LIGNIN AND LIGNIN MODEL COMPOUND.....	11
2.1 Introduction .....	11
2.1.1 Lignin.....	11
2.1.2 Pyrolysis of lignin .....	14
2.1.3 Pyrolysis of lignin model compound.....	16
2.2 Materials and Methods.....	19
2.2.1 Lignin Preparation.....	19
2.2.2 Synthesis of Lignin Model Compound .....	20
2.2.3 Analytical Methods .....	21
2.2.3.1 Thermogravimetric Analysis .....	21
2.2.3.2 Pyroprobe-GC-MS System .....	22
2.2.3.3 <sup>1</sup> H-NMR and <sup>13</sup> C-NMR .....	22
2.2.3.4 DP-MAS <sup>13</sup> C NMR .....	22
2.2.3.4 Gel Permeation Chromatograph .....	23
2.2.3.5 FTIR .....	23
2.2.3.6 Total Organic Carbon Analysis (TOC) .....	23
2.3 Pyrolysis of Lignin.....	23
2.3.1 Thermo gravimetric Analysis .....	23
2.3.2 Pyrolysis in Pyroprobe .....	31
2.3.3 Conclusions .....	35
2.4 Pyrolysis of lignin model compound.....	37
2.4.1 Characterization of oligomeric lignin model compound .....	37
2.4.2 Thermogravimetric analysis.....	40
2.4.3 Pyroprobe GC-MS Analysis .....	47
2.4.4 Conclusion.....	55



3. REENGINEERED FEEDSTOCK™ FOR COAL COMBUSITON EMISION CONTROL .....	57
3.1 Introduction .....	57
3.1.1 Refused Derived Fuel (RDF) .....	57
3.1.2 Co-firing coal and RDF.....	58
3.1.5 ReEngineered Feedstock™ .....	59
3.1.3 Flue Gas Desulfurization .....	61
3.1.4 Sorbents for Flue Gas Desulfurization .....	62
3.2 Fluidized Bed Combustion .....	63
3.2.1 Materials .....	64
3.2.2 Experimental Apparatuses and Procedure .....	65
3.2.3 Analytical Methods .....	68
3.2.4 Results and Discussions .....	69
3.2.4.1 Mechanism of Co-combustion of Coal and ReEF.....	69
3.2.4.2 Combustion Efficiency .....	70
3.2.4.3 Sulfur Dioxide Reduction .....	72
3.2.4.4 NO Reduction.....	74
3.2.5 Conclusion.....	78
3.3 Drop tube Reactor .....	78
3.3.1 Materials .....	79
3.3.2 Experimental Apparatus and Procedure.....	85
3.3.2.1 Drop tube reactor .....	85
3.3.2.2 Calcination Reactor.....	86
3.3.3 Results and Discussions .....	87
3.3.3.1 Sulfation of ReEF.....	87
3.3.3.2 Calcination/Combustion of ReEF .....	95
3.3.3.3 Kinetic Modelling of Sulfation of Calcined ReEF.....	99
3.3.4 Conclusions .....	102
3.4 Economic Analysis.....	103
3.4.1 Fuel Cost .....	104
3.4.2 Capital Cost .....	105
3.4.3 Operation and Maintenance Cost.....	107
3.4.4 Other Benefits.....	107
3.4.5 Conclusion.....	109
4. CONCLUSION AND FUTURE RESEARCH.....	110
4.1 Conclusions .....	110
4.1.1 Pyrolysis of lignin and lignin model compound .....	110
4.1.2 ReEngineered Feedstock™ for Coal Combustion Emission Control .....	111
4.2 Future research on pyrolysis of lignin.....	113
4.2.2 Pyrolysis of Oligomeric lignin model compound .....	113
4.2.1 Slow pyrolysis of lignin for bio-char production.....	114
4.3 Future research on Re-Engineered Feedstock™ .....	114
4.3.1 Enhance carbon conversion.....	114
4.3.2 Metal issues in the combustion .....	115
4.3.3 Gasification of ReEF .....	117

APPENDICES

A. UNREACTED SHRINKING CORE MODEL .....	119
B. NOMENCLATURE .....	122
BIBLIOGRAPHY .....	125

## LIST OF TABLES

Table	Page
Table 1. Comparison of thermochemical conversion .....	7
Table 2. Major linkages in lignin .....	13
Table 3 Elemental analysis for original Maplewood lignin and solid products .....	27
Table 4 Characterization of FT-IR spectrum.....	29
Table 5 NMR chemical shift of solid lignin residue from enzymatic hydrolysis.....	30
Table 6 Percentage of total spectral area assigned to methoxy group and nonprotonated aromatic carbon.....	31
Table 7. Weight distribution of lignin pyrolysis products from pyroprobe reactor.....	32
Table 8 Carbon balance of lignin pyrolysis products from pyroprobe reactor.....	33
Table 9 Carbon selectivity of condensed liquid products from a Py-GC-MS analysis.....	34
Table 10 Characterization of FTIR spectra of lignin model compound.....	45
Table 11. Weight balance of pyrolysis of lignin model compound in pyroprobe .....	48
Table 12. Carbon balance of pyrolysis of lignin model compound in pyroprobe .....	49
Table 13. Carbon selectivity of liquid products detected by Py-GC/MS.....	49
Table 14: Elemental analysis of Coal and ReEF.....	64
Table 15: Properties of ReEF and sorbent feedstock.....	65
Table 16: Temperature profile of the combustion reactor.....	68
Table 17: Gas flow rate and feeding conditions for combustion.....	68
Table 18: Elemental analysis of ReEngineered Feedstock containing Sorbocal lime .....	80
Table 19: Surface area of ReEF and calcium hydroxide .....	80
Table 20 kinetics parameters of sulfation for calcined sorbent in 21% O <sub>2</sub> .....	101
Table 21: Economic Analysis on the ReEF and Conventional Coal Power Plant.....	105
Table 22: Carbon tax on ReEF process and conventional coal plant .....	108

## LIST OF FIGURES

Figure	Page
Figure 1. World energy consumption outlook.....	1
Figure 2. Electricity generation by renewables in USA.....	2
Figure 3. Waste management hierarchy.....	5
Figure 4. Conversion of biomass.....	6
Figure 5. Products selection from conversions.....	10
Figure 6 Hypothetical structure of enzymatic lignin residue and common linkage types .....	12
Figure 7 Major products obtained from lignin pyrolysis .....	15
Figure 8 Monomeric lignin model compounds.....	17
Figure 9. Dimer model compound .....	19
Figure 10. Synthesize of oligomeric lignin model compound.....	21
Figure 11. Thermogravimetric and differential thermal curves for pyrolysis study. Maplewood (green), solid lignin residue after enzymatic hydrolysis (brown) and lignin extracted from Maplewood by organosolv method (orange) at heating ramps of 1 (a and d) 15 (b and e) and 150 K·min <sup>-1</sup> (c and f).....	24
Figure 12. TGA for the pyrolysis of Maplewood lignin residue from enzymatic hydrolysis .....	26
Figure 13. FT-IR spectrum of solid samples. (a) solid lignin residue from enzymatic hydrolysis, and solid product samples obtained at (b) 648 K, (c) 713 K, and (d) 773 K during the pyrolysis at a heating ramp of 150 K min <sup>-1</sup> . .....	28
Figure 14. Direct polarization/magic angle spinning (DP/MAS) spectra of solid samples. (a) solid lignin residue from enzymatic hydrolysis, and solid product samples obtained at (b) 648, (c) 713, and (d) 773 K during the pyrolysis at a heating ramp of 150 K min <sup>-1</sup> . .....	31
Figure 15 Proposed reaction pathway of lignin pyrolysis.....	35
Figure 16 <sup>1</sup> H NMR of β-O-4 lignin model compound .....	38
Figure 17 <sup>13</sup> C NMR of β-O-4 lignin model compound .....	39
Figure 18 GPC of β-O-4 lignin model compound .....	40

Figure 19 Thermogravimetric and differential thermal curves for the pyrolysis study. Lignin model compound (dash line) and lignin residue after enzymatic hydrolysis (solid line) at temperature ramps of 1 (a and b) 15 (c and d) and 150°C/min (e and f).....	41
Figure 20 GPC of lignin model compound and intermediate products. Model compound (solid) , product from 250 °C(dash), product from 350 °C(dot).....	42
Figure 21 <sup>1</sup> H NMR of lignin model compound and intermediate products. (a) lignin model compound, (b) product from 250 °C, (c) product from 350 °C.....	43
Figure 22. FTIR spectrum of lignin model compound and solid residues. (a) lignin model compound (b)350 °C, (c)450 °C, (d)550 °C. ....	46
Figure 23: Mass spectroscopy of mass to charge ratios in TGA. Solid-18, dash-28, dot-44. ....	47
Figure 24:..Proposed reaction mechanism of pyrolysis of lignin model compound .....	55
Figure 25: Schematic of Fluidized Bed Combustion Reactor set up. (a) a flow diagram of the combustion system; (b) a 3D rendering of the reactor. ....	66
Figure 26. The mechanism of co-combustion of coal and ReEF materials. ....	70
Figure 27. Carbon conversion of coal and coal/ReEF mixtures combustion .....	71
Figure 28. Sulfur dioxide reduction of co-firing ReEF and coal. The left column is SO <sub>2</sub> flue gas concentrations for different feedstock at temperatures, 1200, 1400, 1600°C: (a) coal and coal/ReEF mixtures; (b) coal and mixtures with Ca-based sorbent; (c) coal and mixtures with Na-based sorbent. The right column is the corresponding SO <sub>2</sub> reduction for different feedstock at temperatures, 1200, 1400, 1600°C: (d) coal/ReEF mixtures; (e) mixtures with Ca-based sorbent; (f) mixtures with Na-based sorbent. ....	73
Figure 29. NO reduction in co-firing ReEF and coal. (a) coal and coal/ReEF mixtures; (b) coal and mixtures with Ca-based sorbent; (c) coal and mixtures with Na-based sorbent. ....	76
Figure 30. Particle size distribution of ReEF.....	81
Figure 31. Calcium hydroxide and carbon content in ReEF at different particle sizes .....	81
Figure 32. Images of ReEF. (a) ReEF pellet, (b) Particle size larger than 1 mm, (c) Particle size between 212 μm and 500 μm, (d) Particle size between 25 μm and 53 μm .....	82
Figure 33. Microscopic images of ReEF. (a) less than 25 μm, (b) 25-53 μm, (c) 53-212 μm, (d) 212-500 μm .....	83
Figure 34. SEM-EDX of Reengineered feedstock. a) SEM image of ReEF, b) Enlarged SEM image of area in white box in (a), c) EDX mapping of white box in (b), d) Spectrum of EDX of white box in (b) .....	84

Figure 35. Drop tube sulfation reactor setup. 1) Feeding rotary valve 2) Swagelok tee 3) 1 inch quartz tube 4) Thermocouple 5) ATS furnace 6) Quartz frit 7) ¼ inch quartz tube .....	86
Figure 36. Calcination reactor setup. 1) quartz rod, 2) Swagelok ultr-torr fitting, 3) gas inlet, 4) furnace, 5) gas outlet, 6) sample collection vial, 7) quartz boat, 8) Thermocouple .....	87
Figure 37. Reactions of ReEF dropping into the furnace. ....	89
Figure 38. The sulfur dioxide concentration profile for a typical run .....	90
Figure 39. Conversion of sorbent with reaction time at 900 °C. Pure sorbent (dash line) and sorbent in ReEF (solid line) under 5% O <sub>2</sub> (a), 10% O <sub>2</sub> (b), 20% O <sub>2</sub> (c) and 30% O <sub>2</sub> (d). ....	92
Figure 40. Conversion of Calcium hydroxide in ReEF after 5min run .....	93
Figure 41. Maximum reaction rate of sorbent sulfation in ReEF is delayed by biomass combustion .....	94
Figure 42. Time delay on the maximum reaction rate. (□ 25-53 μ m, ○ 53-212 μ m, Δ 212-500 μ m) .....	95
Figure 43. XRD pattens of calcined sorbents from calcination reactor (21%O <sub>2</sub> ). a) calcination of sorbacal in 30s, b) calcination of sorbacal in 60s, c) calcination of ReEF in 60s, d)calcination of ReEF in 120s. ....	97
Figure 44. SEM Images of calcined ReEF: a) Calcined ReEF at 800C, 120s, 21% O <sub>2</sub> , b) Calcined ReEF at 800C, 120s, 100% O <sub>2</sub> . ....	98
Figure 45. The sulfation behavior of calcined ReEF. a) ReEF calcined at 800C, 120s, 21%O <sub>2</sub> . b) ReEF calcined at 800C, 120s, 100%O <sub>2</sub> . ....	99
Figure 46. The Unreacted shrinking core model and grain model .....	100
Figure 47. The modelling of sulfation behavior of calcined ReEF. a) ReEF calcined at 800C, 120s, 21%O <sub>2</sub> . b) ReEF calcined at 800C, 120s, 100%O <sub>2</sub> . ....	102
Figure 48. The schematic process flow of conventional coal power plant and ReEF process...	104
Figure 49: The reaction steps of pyrolysis of lignin model compound .....	111
Figure 50. Unreacted shrinking core model.....	119

# CHAPTER 1

## INTRODUCTION

### 1.1 World Energy Outlook

With the fast growth of world population and developing industries, the energy demand has been dramatically increased in the past decades and it will keep increasing in the next twenty years as shown in Figure 1<sup>1,2</sup>. The major energy supply are and still will be from fossil fuels including oil, natural gas and coal. Currently, other formats of energy sources like nuclear, hydro power, and renewable materials only occupy about 15% of total energy consumption. It is predicted that one fifth of the energy will be supplied from these non-fossil fuel feedstock in 2035.

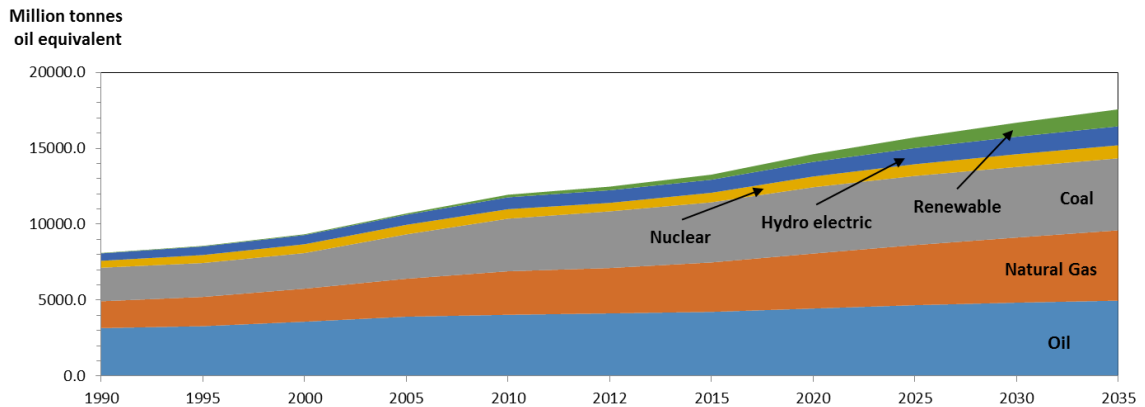


Figure 1. World energy consumption outlook

Problems associating with fossil fuels application are proposed and paid more and more attention by society. The formation of the fossil fuels usually takes million years. The exploiting rate far overpasses their regeneration rate. The depletion of the fossil fuel can be predicted in next a few generations. Reserve to production ratio (R/P ratio) is commonly used to predict the future availability of a resource. The R/P ratio presents a ratio of the amount of a resource known to exist in an area and this resource used in one year at the current rate. Take coal for example,

the current R/P ratio in the North America area is 250, which means coal can be utilized in next 250 years at current rate in North America<sup>3</sup>. This R/P ratio of coal is much lower in other areas such as Asia. Despite some deviations may happen on the statistics, the problems of fossil fuels depletion need to be seriously considered. Other than that, environmental impacts are another big concern when utilizing fossil fuels. Currently, the world is facing the global warming due to the greenhouse gases emission. In some areas, the pollutant emissions such as SO<sub>x</sub>, NO<sub>x</sub>, and PM lead to a poor air quality that damages environment and human health. Additionally, the chemical processes relying on the fossil fuels are sensitive to the price of the fuels. Price of crude oil increased from 30 \$/barrel to 105 \$/barrel in the last 10 years<sup>3</sup>, which results in the negative influences on the economics. To achieve economic growth, energy security, and environment benefits, a long term sustainable development need to be established. Meanwhile, other energy sources need to be developed to supplement or replace the traditional fossil fuels in the future.

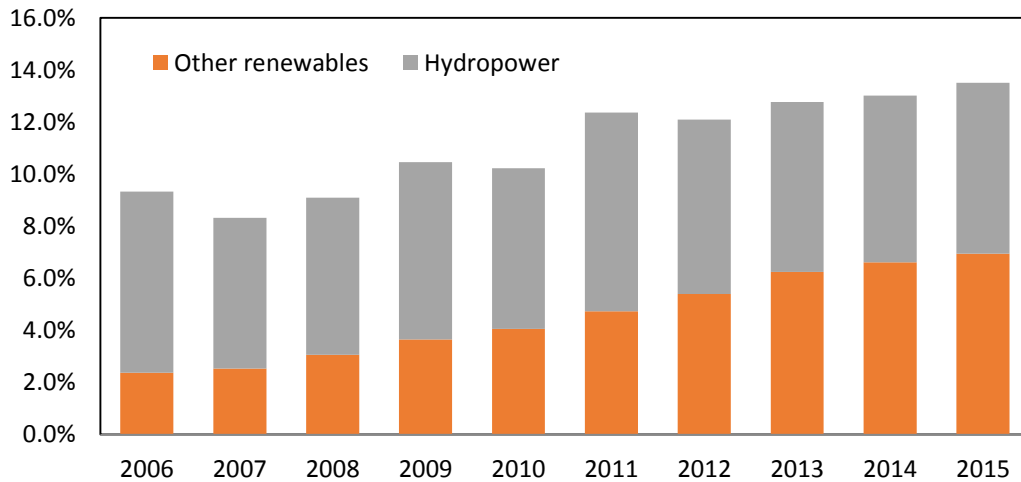


Figure 2. Electricity generation by renewables in USA

Renewable energy is derived from natural processes. They can be constantly replenished and do not consume exhaustible resources. Renewable energy has replaced the conventional fossil fuels in electricity generation, space heating, motor fuels, and rural energy services<sup>4</sup>. A low



carbon footprint is achieved in renewable energy applications. Figure 2 shows the electricity generation by renewables in USA<sup>5</sup>. Statistics shows that a gradual increase in electricity generation by the renewables. Hydropower generates half of the electricity in total electricity generation. The development of technologies allow us to harvest renewable energy from various sources including bioenergy, hydropower, wind energy, ocean energy, geothermal energy, and solar energy. In the past decades, most of the technologies are successfully deployed and functioning to produce power. It is quite promising that renewable resources will become an important energy supply in the future mainly due to they are abundant, cheap, and environmental friendly.

### **1.2 Waste Biomass: New Energy Resource**

Biomass is defined as organic materials that comes from plants and animals. The major compositions of biomass are hydrocarbon compounds, which potentially can be converted to chemicals and energy. Among the energy production from biomass, about 65% of the biomass is utilized by residence<sup>6</sup>, mainly for the cooking and heating. Biomass can be mainly categorized into four types. Woods are the products or byproducts from trees or forest including logs, bark, sawdust, wood chips, and wood pellets. Energy crops such as short rotation crops, sugar, and starch crops are dedicated to make biofuels such as bioethanol. They are densely planted, high yielding, and require low cost and maintenance on harvesting. Agricultural residues like straw, corn stover, and poultry litter were used to burn on the farm site. This caused a lot of environmental issues while the energy was utilized in a low efficiency. Today, these agriculture wastes can be utilized in boilers or gasifiers to produce power and chemicals in a more efficient way. The last type of biomass is wastes. Municipal wastes are generated from every aspect of people life from dinning, drinking to working. Industrial wastes include all the byproducts

produced in the process. With the growing demand from fast growth of population, the wastes generation increases dramatically. The fundamental concept of waste management has been changed. Wastes, as new resources, are beneficially used in bioenergy generation and land applications.

250 million tons of municipal solid waste (MSW) was produced in 2012 in U.S., which equals 4.4 pounds of waste per person per day<sup>7</sup>. Half a century ago, the major treatment on the waste was disposal. This consumed landfill spaces and caused environmental issues. Today, several options are developed to make the waste management more efficient and environmental friendly as shown in Figure 3<sup>8</sup>. Source reduction and reuse is the most preferred way due to the reduction of the total waste generation. For example, most of the service documents going paperless greatly reduces the paper usage in the banking system. Reuse and recycling involves making the materials that would otherwise be disposed into new products. Reuse and recycling has environmental benefits at every stage in the life cycle of products. Meanwhile, it reduces the greenhouse gas emission from waste combustion. In 2012, 34.5 % of the municipal solid waste were recycled<sup>7</sup>. As we mentioned, waste is one of the biomass that can be converted into chemicals and energy. The conversion process is often called waste-to-energy (WTE) process. A variety of processes have been applied to treat wastes including combustion, gasification, pyrolysis, anaerobic/aerobic digestion, and landfill gas recovery. Among them, combustion is commonly used to reduce the volume of the wastes and produce electricity from the combined heat and power (CHP) process. However, only a small portion, 11.7 % of the MSW was subjected to energy recovery in 2012<sup>9</sup>. The regulations on the emissions from combustion of waste become stricter considering the environmental impacts. This would bring burdens to the plants that burn the wastes. Advanced flue gas cleaning system is required to meet the regulation. However it would increase their capital investment and operation cost. The combustion process mainly

generates heat and flue gas. However, other technologies like anaerobic digestion or gasification can produce the biogas or syngas which can be further used in other industries. Both technologies are promising alternatives options other than combustion. About 53.8% of MSW were discarded in 2012<sup>9</sup>. This requires the usage of landfill space. With limited land space and high tipping fee, the disposal of MSW won't be more economic benefit than other waste treatments.

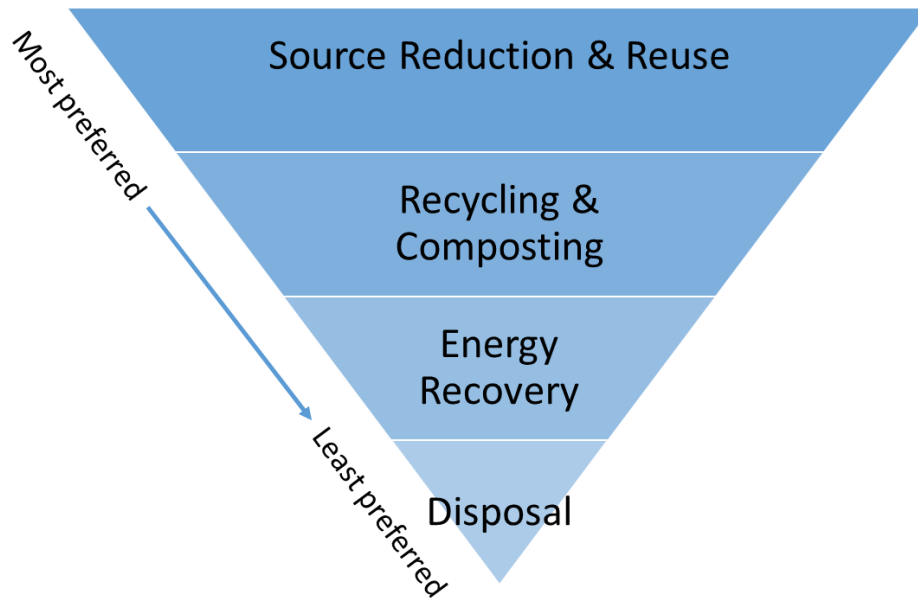


Figure 3. Waste management hierarchy

Traditional treatments on the waste disposal are no longer advocated. The efficient waste management is established on the concept of treating wastes as a new valuable resource. The wastes can be either reused or recycled. Alternatively, to reduce the dependence on the fossil fuels, wastes, as one of biomass resources, can be converted to chemicals, fuels and energy. Meanwhile, this requires the development of the technologies that are efficient on the conversion, environmental friendly and accepted by society.

### 1.3 Thermochemical Conversion

Renewable energy production from biomass requires a certain chemical conversion process. Depending on the characterization of feedstock, various conversion processes can be selected as presented in Figure 4<sup>10</sup>. For each process, a major direct product is produced such as syngas or bio-gas. More often, the direct products are used as intermediates for further upgrades and processes. Thermochemical conversion mainly refers to combustion, gasification, and pyrolysis. The comparisons are listed in Table 1.

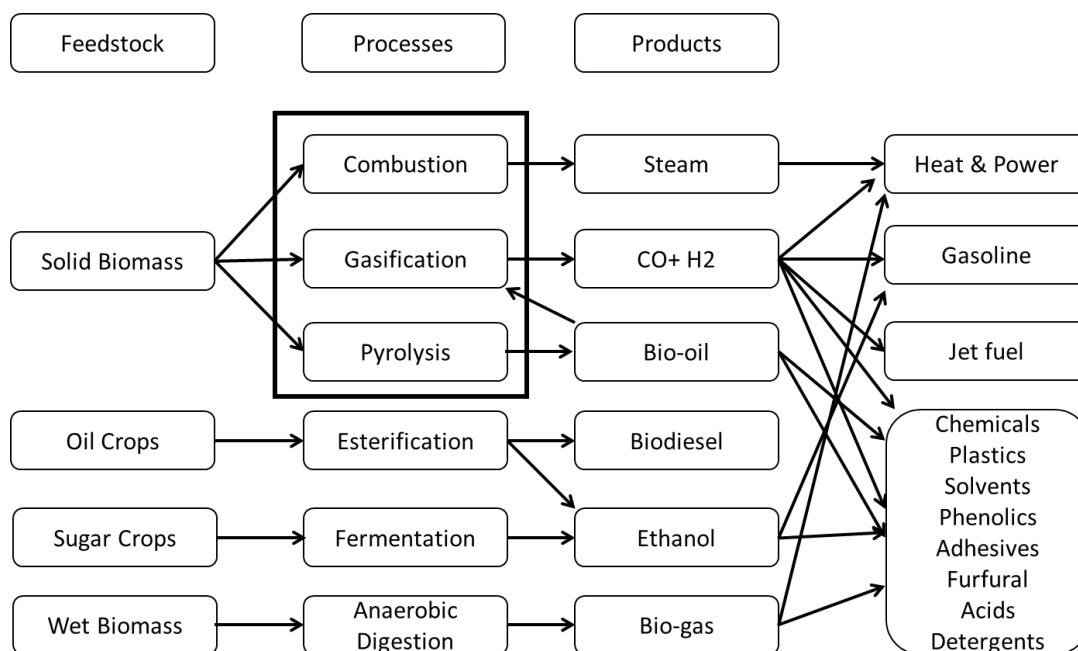


Figure 4. Conversion of biomass

Combustion is the thermal conversion of organic matters with an oxidant to produce primarily carbon dioxide and water. Usually, to achieve the complete combustion, the excess oxidant is required. Combustion is an extreme exothermal reaction. It releases the energy stored in the chemical bonds. The temperature of the combustion usually is over 1000 °C. In some coal boiler, the temperature reaches above 1500 °C. If the gas and solid are mixed well in the reactor,

the final products are all in their oxidized form. The flue gas mainly consists of non-combustible carbon dioxide and water. The sulfur and nitrogen in the feedstock are converted to  $\text{SO}_x$  and  $\text{NO}_x$ , respectively. The emission of  $\text{SO}_x$  and  $\text{NO}_x$  to the atmosphere leads to the severe environmental issues such as acid rain and smog formation. Flue gas cleaning system is required to reduce  $\text{SO}_x$  and  $\text{NO}_x$  to a level below emission limit. Due to the extreme high temperature, most of the metal elements in the feed melt and even vaporize in the combustion. Slagging and fouling caused by volatilization of metals are the major operation issues in the power plant. Low boiling point metals like mercury need to be captured using additional sorbent. The heat generated from combustion of the feedstock is recovered for steam production. High temperature and pressure steam is sent to a steam turbine for electricity generation.

Table 1. Comparison of thermochemical conversion

		Combustion	Gasification	Pyrolysis
Major Products		$\text{CO}_2$ and $\text{H}_2\text{O}$	Syngas: $\text{CO}$ and $\text{H}_2$	Bio-oil Bio-char
Oxygen Requirement		Excess air Oxidizing environment	Controlled amount Reducing environment	In the absence of oxygen
Reaction Temperature		1000 – 1600 °C	800 – 1200 °C	200-800 °C
Emissions	N Element	$\text{NO}_x$	$\text{NH}_3$ , $\text{N}_2$ , $\text{HCN}$	$\text{NH}_3$ , $\text{N}_2$ , $\text{HCN}$
	S Element	$\text{SO}_x$	$\text{H}_2\text{S}$ , $\text{COS}$	$\text{H}_2\text{S}$ , $\text{COS}$

Gasification mainly converts the organic matters into carbon monoxide and hydrogen (syngas) under a controlled amount of oxygen. One of the advantages that gasification over combustion is that syngas can be utilized to produce diverse products as shown in Figure 4. The produced syngas can be directly used in a thermal oxidizer for combustion. Additionally, clean syngas can be combusted in a gas turbine. Integrated gasification combined cycle (IGCC) plant utilizes combusted syngas to produce power and steam, which improves the efficiency of power generation compared to traditional pulverized coal power plant. Other than combustion, syngas

is the important intermediate in synthesizing other products. Waxes, Olefins, Diesel and gasoline can be synthesized by syngas through Fischer-Tropsch process. Pure hydrogen can be obtained by water gas shift reaction, which is further used in ammonia production. Through the catalytic reactions, methanol can be converted from syngas. Methanol is another key industry intermediate to produce dimethyl ether (DME), methyl tertiary butyl ether (MTBE), and acetic acid<sup>11</sup>. In the gasification, the air to fuel equivalent ratio is between 0.2 and 0.4. With more oxidant in the system, the more complete combustion will achieve with carbon dioxide and water generation. This would lower down the heating value of the product gas stream, which is not desirable in the gasification process. Due to the partial oxidation in the gasification, the temperature is lower than that in combustion process, usually between 800 °C- 1200 °C, except for plasma gasification. The fate of sulfur and nitrogen ends up in their reducing form: sulfides and ammonia, respectively. The sulfur and nitrogen is easy to remove and recovered in other processes. The gasification of biomass gives more opportunities on products selection than combustion. Meanwhile, gasification is considered as a more environmental friendly technology than combustion.

Pyrolysis is thermal destruction of organic materials at elevated in the absence of oxygen. The major products from the pyrolysis of organics are pyrolysis oil (bio-oil) and solid char (bio-char) depending on the heating rate. In fast pyrolysis and short resident time, more bio-oil is produced. Bio-oil produced from biomass fast pyrolysis is a dark-brown fluid. It contains a mixtures of acids, alcohols, aldehydes, furans, ketones, oxygenates, phenols and aromatics. Bio-oil is not stable in the atmosphere and degrading and polymerizing with time. Due to the high oxygen and water content in the bio-oil, oil upgrading process is required to remove the oxygen and water from bio-oil before further applications. Bio-oil can be separated into water soluble part and water insoluble part. Both of streams can be subjected to the catalytic upgrading process.

Due to the high diversity of the bio-oil, the catalytic upgrading is a complicated reaction network. A series of reactions including catalytic cracking, hydrogenation, hydrodeoxygenation, decarboxylation, decarbonylation and polymerization have been reported in the literatures<sup>12-14</sup>. Noble metal catalysts and zeolites are commonly used as catalysts. The upgraded bio-oil can be further processed for gasoline, diesel and jet fuel production. The technology of catalytic fast pyrolysis (CFP) is promising in converting the biomass into bio-oil. By using the catalysts in the pyrolysis process, a high degree of deoxygenation is achieved compared to the situation without catalysts. CFP directly produces gasoline-range olefins and aromatics. To obtain a high yield and selectivity of products, the proper catalyst should be selected. Otherwise, the undesirable products like coke would be majorly formed. Bio-char is the major product when applying a slow heating rate and long resident time. Bio-char is active and its porous structure can be beneficially used in adsorptions and species captures/retains. Applications of bio-char are carbon sink for CO<sub>2</sub> capture, soil amendment, syngas production, etc. Contrast to combustion, pyrolysis is endothermic reaction which requires the additional energy input for the process. The temperature of pyrolysis usually is between 200 °C and 800 °C. High temperature is not favorable for bio-oil production.

As we mentioned above, three major thermochemical conversion technologies can convert biomass into chemicals, fuels and energy. Figure 5 presents the carbon, hydrogen, and oxygen ternary diagram with three major thermochemical conversion technologies. Biomass is cycled in the diagram by its composition. For the char production, the slow pyrolysis is required. Fast pyrolysis produces the light gases such as methane, ethylene and bio-oil. Using different mediums (O<sub>2</sub>, H<sub>2</sub>O or H<sub>2</sub>) in gasification process, the composition of syngas would be varied. With excess oxygen input to the process, the combustion is enhanced resulting in the production of CO<sub>2</sub>. The choice of technology should be considered majorly based on the product demand.

Thermochemical conversions on the fossil fuels are proven technologies in the production of chemicals and energy. However, applications of these technologies on the waste biomass are still not quite mature. Great efforts from field tests while fundamental research needs to be done before commercializing these technologies on waste biomass conversion.

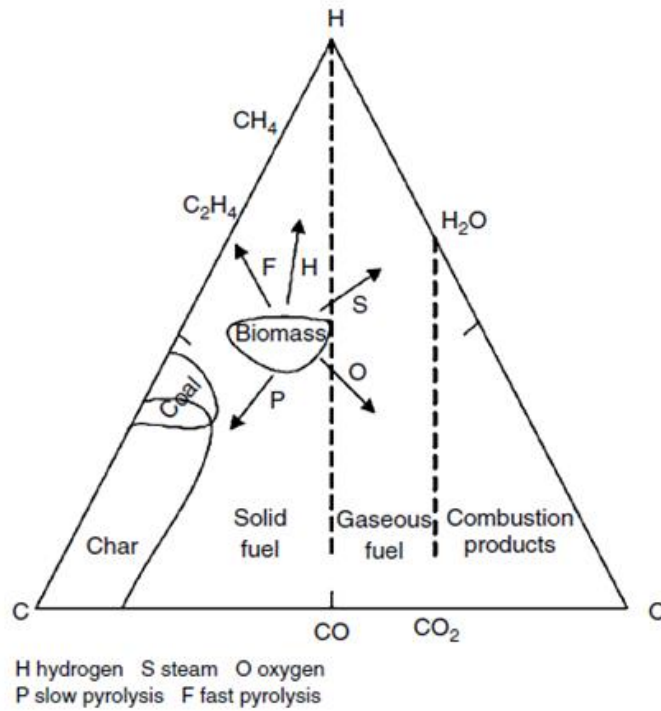


Figure 5. Products selection from thermochemical conversions



## CHAPTER 2

### PYROLYSIS OF LIGNIN AND LIGNIN MODEL COMPOUND

Lignin is the major byproduct from pulping and paper industry and is usually combusted to provide the heat for the pulping process as a waste. However, its poly-methoxylated phenylpropane structure makes lignin a potential natural source for phenolic and aromatic chemicals. Obtaining high yield of chemicals from lignin is a challenge due to its complex structure and unreactive nature. In this chapter, the pyrolysis behavior of lignin extracted from maple wood and a  $\beta$ -O-4 oligomeric lignin model compound is presented.

#### 2.1 Introduction

##### 2.1.1 Lignin

Lignin along with cellulose and hemicellulose are the three major components in lignocellulosic biomass. In plant cell wall, lignin fills the space between cellulose and hemicellulose. The major function of lignin is holding the lignocellulose matrix together<sup>15</sup>. Lignin is the second abundant component and occupies about 15 % - 30 % in biomass by dry weight<sup>16</sup>. Lignin has a complex amorphous structure that mainly consists of methoxylated phenylpropane units connected by various linkages. Advanced spectroscopy technologies have been applied to elucidate the detailed structure of lignin. Although the fundamental constituents and linkages in lignin are revealed, the exact structure of untreated protolignin is still unknown. From the biosynthesis study, formation of lignin is considered to involve polymerization steps of three monolignols: p-coumaryl, coniferyl and sinapyl alcohols<sup>17</sup>. Figure 6 shows the hypothetical structure of lignin and common linkages<sup>18</sup>. Ether linkages occupy the largest proportion of lignin regardless of its origin, i.e. softwood or hardwood lignin. Among them  $\beta$ -O-4 is the most common ether linkage as summarized in Table 2<sup>19</sup>. In addition to the ether linkages, C-C bonds including  $\beta$ -

5, 5-5,  $\beta$ -1 and  $\beta$ - $\beta$  also play a role in connecting lignin monomeric aromatic substructure.

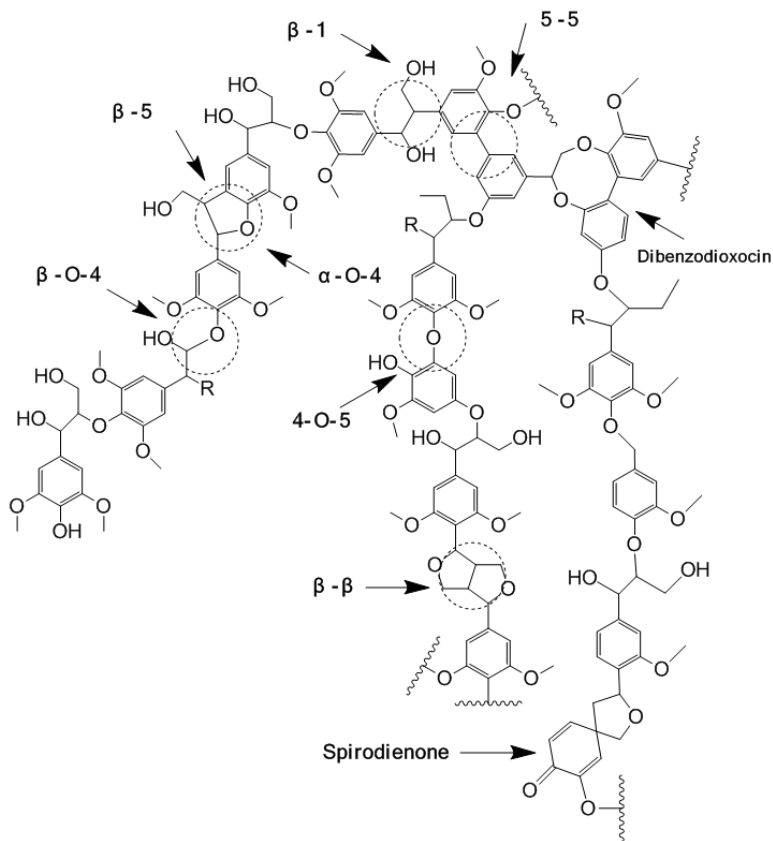


Figure 6 Hypothetical structure of enzymatic lignin residue and common linkage types

Lignin structures and compositions of functional groups widely vary depending on the origin of biomass and extraction methods. It is generally known that the isolation of lignin compounds from original biomass is impossible to achieve without chemical modification. Based on the extraction method, lignin can be categorized as alkali lignin, lignosulfonates, organosolv lignin, and milled wood lignin<sup>20</sup>. First three types of lignin are involved in chemical process while last one are mechanical. In pulping and paper industry, Kraft and organosolv process are widely applied. Kraft lignin is generated from Kraft pulping process. The process employs the sodium hydroxide and sodium sulfide as agents. The high PH breaks the bonds between lignin and cellulose. Gierer et al. described the structure changes of lignin during the Kraft pulping process<sup>21</sup>.

Most weak oxygen-carbon linkages break while the carbon-carbon bond such as 5-5 biphenyl survives during the process. Meanwhile, some new functional groups will be introduced in the process. Organosolv lignin is obtained from organosolv process. Organosolv process involves the usage of organic solvent such as acetone, methanol, ethanol, and acetic acid. The fragments of lignin dissolve in the solvent and then are precipitated in the downstream. One of the advantages of organosolv process is that it generates three separate streams which are cellulose, hemicellulose and lignin, respectively. Compared to the Kraft lignin, organosolv lignin contains low sulfur. In a short sum, lignin extractives are mainly classified into two different categories based on the separation methods<sup>20</sup>. One is the lignin extracted by its dissolution in solvent and the other is the lignin residue obtained after removal of sugar components by hydrolysis. In the former method, lignin linkages are broken by strong acid<sup>22</sup>, base catalysts<sup>23</sup> or mechanical stress<sup>24</sup>. Resulting smaller fragments of lignin are dissolved in the solvent to be extracted like Kraft and organosolv lignin. In the latter method, cellulose and hemicelluloses is hydrolyzed by acids<sup>25</sup> or enzymes<sup>16</sup>. Resulting sugar monomers are soluble in a liquid mixture and the lignin compound remains as an insoluble solid residue. Thus it is expected that the lignin residue obtained from hydrolysis is more similar to the original lignin than the lignin extracted in a solvent since the lignin residues are exposed to less severe chemical reactions.

Table 2. Major linkages in lignin

Linkages	Type	Softwood (%)	Hardwood (%)
$\beta$ -O-4-aryl ether	C-O-C	46	60
$\alpha$ -O-4-aryl ether	C-O-C	6-8	6-8
4-O-5-diaryl ether	C-O-C	3.5-4	6.5
$\beta$ -5-phenylcoumaran	C-C	9-12	6
5-5-biphenyl	C-C	9.5-11	4.5
$\beta$ -1-(1,2-diarylpropane)	C-C	7	7
$\beta$ - $\beta$ -(resinol)	C-C	2	3
Other	-	13	5

### 2.1.2 Pyrolysis of lignin

Pyrolysis of lignin has been studied by a handful of people over the decades. The behaviour of pyrolysis lignin can be affected by type of lignin, pyrolysis temperature, heating rate, and additives<sup>26-28</sup>. Due to the complex structure of lignin, pyrolysis products are highly diverse. Gases, liquids, and solids are produced from the lignin pyrolysis. Gases includes carbon monoxide, carbon dioxide, hydrogen and methane. Liquids, or bio-oil part, are a mixture of acids, alcohols, monolignols, monophenols and other polysubstituted phenols. The structure of lignin consists of mainly aromatic and phenolic units. Thus, the production of aromatic or phenolic monomers or polymers are characteristics of pyrolysis of lignin<sup>29</sup> as shown in Figure 7. A fraction of lignin is converted to stable solid product called char. The production of char is higher at lower temperature<sup>30</sup>.

In 1970s, Iatridis et al. pyrolyzed Kraft lignin in a “captive sample” reactor at temperature of 400 °C-700 °C and only identified a few compounds by gas chromatography including hydrocarbons, methanol, acetone, phenol and guaiacol due to the limited analytical technology<sup>31</sup>. In 1980s, Nunn et al. studied the yields, composition of major products from pyrolysis of milled wood lignin in a batch pyrolysis. A temperature range of 600-1400 K under 5 psi helium were applied in the experiments. They concluded that tar was the major product above 800 K and it achieved maximum of 53% of yield. The pyrolysis gases including CO, CH<sub>4</sub>, C<sub>2</sub>H<sub>4</sub>, and CO<sub>2</sub> were found to form in the secondary cracking of tar<sup>32</sup>. However, they didn’t analyze the composition of liquid tar. In 1990s, with the development of analytical techniques, a more comprehensive product characterization were obtained<sup>33-36</sup>. TGA coupled with MS, and pyroprobe attached to GC-MS were commonly used in the pyrolysis analysis. Recently, Guozhan Jiang et al. identified about 50 compounds from lignin pyrolysis at a temperature range of 400 °C-800 °C<sup>37</sup>. The phenolic compounds yield was 17.2 % for Alcell lignin and individual yield of most of the compounds were

less than 1%. The thermal decomposition and weight loss of various lignin sources were studied by D. J. Nowakowski<sup>38</sup>. He found the major decomposition of lignin occurred at a temperature range of 350 °C to 450 °C and that the heating rate affected the amount of volatile products.

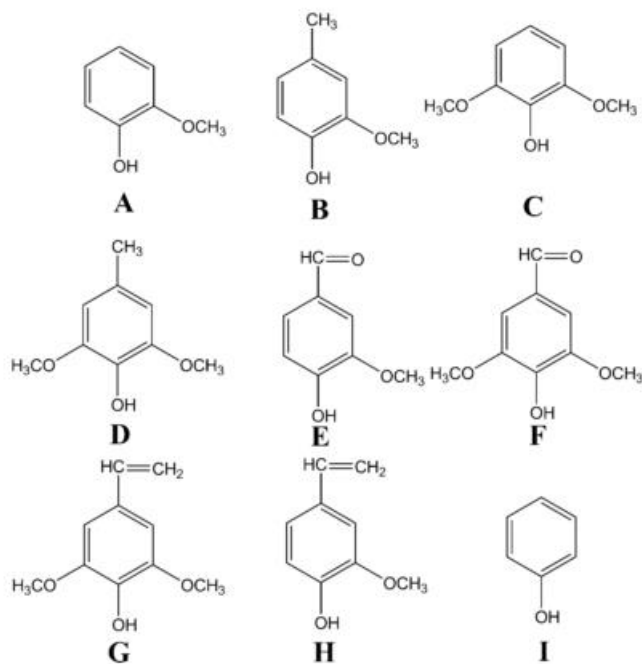


Figure 7 Major products obtained from lignin pyrolysis

The kinetics of pyrolyzing various types of lignin have been extensively studied<sup>20,39-45</sup>. Unlike understanding the chemistry and kinetics of the pyrolysis of cellulose and hemicelluloses<sup>38,46-48</sup>, the complexity of the lignin structure and its high molecular weight present new difficulties to the study. To obtain the kinetic parameter, thermogravimetric analysis (TGA) is commonly used in experiments. It records sample weight loss as a function of time and temperature. By fitting the experimental data with a lumped model, the reaction rate and activation energy can be estimated. Most literatures assume the reaction is first order with respect to the weight loss. This brings the most uncertainty to the estimation<sup>20</sup>. A large variations of estimated activation energy are reported from a range from 60 kJ/mol to 300 kJ/mol. Several

reasons could cause this situation. First, different types of lignin are used in the study. As mentioned above, the structure, functional groups and molecular weight of lignin varies largely on the methods by which is extracted. Second, for a large load of sample piled in the sample boat, the mass and heat transfer could involve in the pyrolysis. However, if a small amount with a thin layer is applied, the measured apparent kinetics could be different. Finally, the selection of model affects the kinetic parameters estimation. For example, some researchers applied distributed activation energy model instead of a fixed activation energy model<sup>39,40,49</sup>. This results in a better fit to the experimental data. However, in the analysis, empirical equations are commonly employed. It is still difficult to use the lumped kinetic parameter to interpret the pyrolysis mechanism.

### **2.1.3 Pyrolysis of lignin model compound**

The complex structure and high molecular weight of lignin make it difficult to study of its pyrolysis chemistry. However, to improve the conversion of lignin to bio-oil, study of its pyrolysis chemistry is imperative. Lignin model compounds have simple structures and product distributions compared to actual lignin. Studying reaction chemistry of lignin model compounds can help us achieve a deep insight of lignin pyrolysis mechanism and determine the stability of intermediate products. The simplest model compound of lignin is monomeric products from pyrolysis of lignin. The study of pyrolysis of monomeric model compounds started thirty years ago. Guaiacol is the simplest model compound and has been studied extensively. The characteristic monomeric model compounds are shown in Figure 8. Vuori et al. studied the substituted anisole with hydroxyl group on o-, m-, and p- position<sup>50</sup>. The experiments were tested in a temperature from 623 to 673 K. The major products were catechol and cresol. The formation of anisole by direct demethoxylation was also significant. The results showed that guaiacol (o-

hydroxyanisole) had the highest reactivity. A major free radical with a concerted reaction mechanism were suggested to explain guaiacol pyrolysis. Dorrestijn and Mulder conducted the pyrolysis of guaiacol in a temperature between 680 and 790 K. Based on the products methane and 1, 2-dihydroxybenzene, they proposed a homolytic route involving the cleavage of methoxyl C-O bond. Klein tested twenty lignin model compounds including substituted monomeric phenolic compound such as syringol, isoeugenol, vanillin, anisole and benzaldehyde. The results showed different functional groups have effects on reactivity<sup>51</sup>. Both free radical reaction and concerted reaction mechanism were proposed in his study. With the development of computational technique, density function theory (DFT) has been used in predicting the reaction pathway in pyrolyzing model compound. Recently, five possible pathways of pyrolysis of guaiacol are proposed by Liu et al<sup>52</sup>. The analysis shows the demethoxylation of guaiacol most likely happens through hydrogen radical abstraction to the carbon atom in the benzene ring where the methoxyl group is located. This route has the lowest energy barrier of guaiacol demethoxylation.

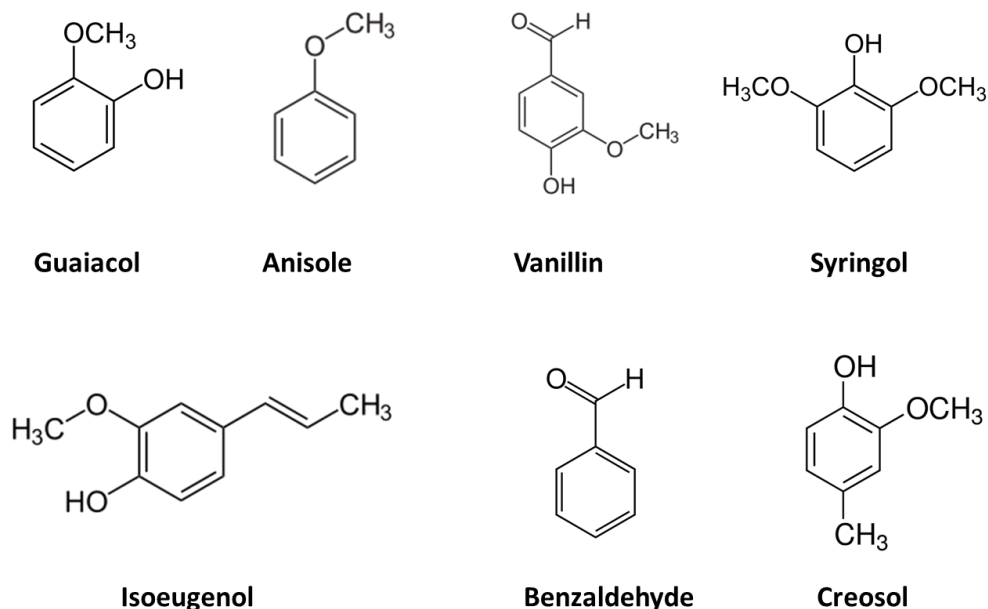


Figure 8 Monomeric lignin model compounds

Dimers containing specific linkage are more preferred as lignin model compounds in pyrolysis study. Dimeric compounds with  $\beta$ -O-4 linkage, carbon-carbon linkage,  $\beta$ -5 linkage,  $\alpha$ -O-4 linkage and 4-O-5 linkage were reported in the literatures.  $\beta$ -O-4 is the most common linkage existing in lignin. The dimers containing only  $\beta$ -O-4 linkage were widely studied. Figure 9 presents the  $\beta$ -O-4 type dimer with various substitute functional groups. Phenethyl phenyl ether (PPE) is the simplest example representing the dominant  $\beta$ -O-4 ether linkage without any substitute functional groups. The research shows that the decomposition of PPE starts with the cleavage of weakest bond, which is C-O bond in  $\beta$ -O-4 linkage. It is estimated that the dissociation energy of C-O bond is 65 kcal/mol compared to 72 kcal/mol for C-C bond in PPE<sup>53,54</sup>. Homolysis of C-O bond generates two radicals which are phenoxy radical and phenethyl radical. They then pick up a hydrogen atom to form final product styrene and phenol<sup>55</sup>. Based on the free radical reaction mechanism, a series of computational study on the key reaction steps have been conducted by Beste including homolytic cleavage, hydrogen abstraction, and oxygen-carbon phenyl migration<sup>56-60</sup>. The understanding of the reaction pathway and mechanism has been greatly enhanced. The effects of different functional groups on pyrolysis reactivity have been studied. Kawamoto and coworkers studied the influence of  $C_\gamma$ -OH on  $C_\beta$ -O cleavage with various p-substitutes. The results show that depending on the  $C_\gamma$  structure, the  $C_\beta$ -O homolysis can happen through quinone methide or direct cleavage<sup>61,62</sup>. The effects of substitutes on the phenethyl ring on the reaction rates of hydrogen pick up has been studied. From the computational calculations, the methoxy substituents decelerate the hydrogen abstractions by the phenoxy radicals<sup>60</sup>. The product distribution of pyrolyzing dimers is more complex than that of monomers. This is due to radicals are reactive, which may lead to secondary reactions. H-abstraction, double bond formation, rearrangement and isomerization diversify the products distribution<sup>63</sup>



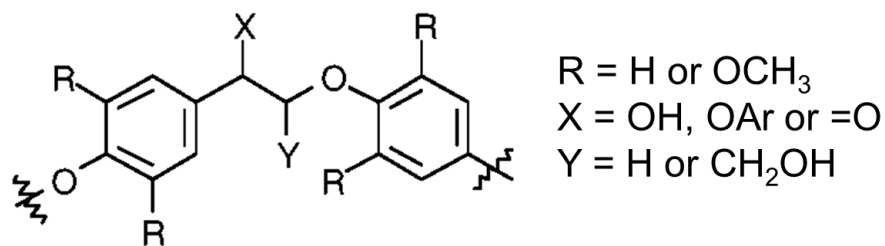


Figure 9. Dimer model compound

Although pyrolysis of monomers and dimers can provide insights on the chemistry of lignin pyrolysis, we cannot ignore the effects of structure distinctions on the pyrolysis behavior between model compounds and lignin. Oligomeric lignin model compounds are more similar to real lignin than monomeric and dimeric model compounds. However, very few research has been done on the pyrolysis of oligomeric lignin model compound. Liu et al. studied the pyrolysis response of  $\beta$ -O-4 lignin model polymer<sup>64</sup>. The H-type and G-type linear synthetic polymers were tested in a tubular reactor. The results show that products from H-type lignin model compound only have p-hydroxyphenyl structure without any methoxyl groups, and the products from G-type models only have guaiacol structure with methoxyl groups.

## **2.2 Materials and Methods**

### **2.2.1 Lignin Preparation**

In this thesis, two different types of lignin from Maplewood were prepared to study the reaction chemistry. One is lignin residue after enzymatic hydrolysis and the other is ethanol organosolv lignin (hereafter they will be designated by 'solid lignin residue' and 'organosolv lignin' for brevity)

The solid lignin residue was prepared by removal of hemicellulose and cellulose compounds by hydrolysis of Maplewood. The hemicellulose compounds were removed by a hot water pre-treatment in a pressurized Parr reactor (620-1517 kPa; 1L volume) followed by

overnight pre-soaking of 10 wt% of Maplewood in water. Filtration and washing produced a solid fraction that mainly contained cellulose and lignin. The pre-treated solid was then hydrolysed by enzymes (Spezyme and Novozyme) to remove the cellulose at pH 4.8 and 50 °C to obtain the solid Maplewood lignin residue. The detailed procedures for enzymatic hydrolysis and the composition analysis are described by Jae et al<sup>16</sup>. The major impurities in the lignin residue sample was glucose (11.6 wt%) and xylose (3.3 wt%).

Organosolv lignin was prepared according to the method of Pan et al.<sup>22</sup>. Maplewood was reacted with ethanol and water mixture (1:1) in the presence of 1.25% of sulfuric acid at the temperature of 180 °C for one hour. The resulting liquid mixture was diluted with water to precipitate organosolv lignin. Finally, a solid organosolv lignin sample was prepared by filtration and drying in the oven at 110 °C overnight.

### **2.2.2 Synthesis of Lignin Model Compound**

The oligomeric lignin model compound was synthesized according to the method of Katahira et al.<sup>65</sup> as shown in Figure 10. The first step involved synthesizing t-butoxycarbonylmethyl vanillin by reacting vanillin with t-butyl-2-bromoacetate and K<sub>2</sub>CO<sub>3</sub>/KI (Step 1 in Figure 10). Polymerization of t-butoxycarbonylmethyl vanillin was conducted in the presence of lithium diisopropylamide solution by the nucleophilic addition of carbanion to an aldehyde group (Step 2 in Figure 10). In the third step, t-butyl group was reduced to hydroxyl group by lithium aluminum hydride. And after acetylation, the oligomeric lignin model compound was synthesized.

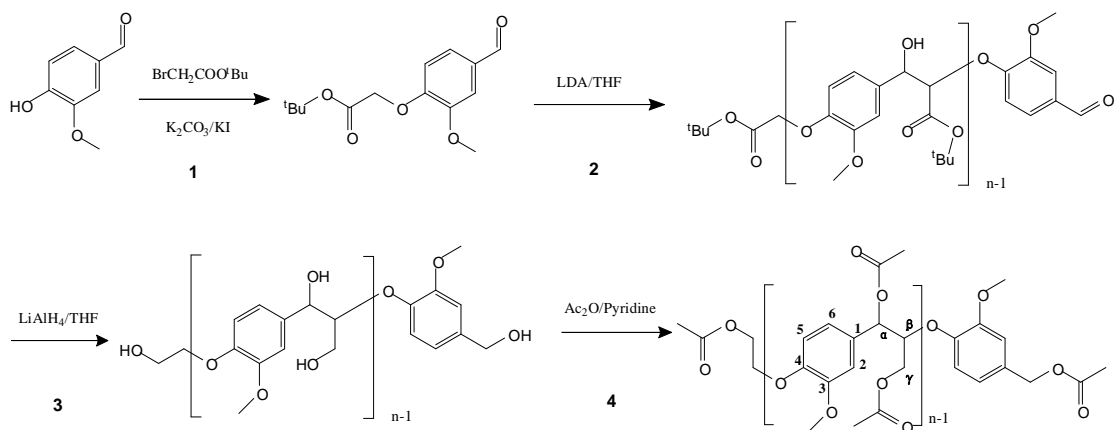


Figure 10. Synthesize of oligomeric lignin model compound.

## 2.2.3 Analytical Methods

### 2.2.3.1 Thermogravimetric Analysis

The pyrolysis of lignin and lignin model compound was performed in a TGA-DSC (TA instruments SDT Q600 system) to measure the weight loss under dynamic or isothermal conditions. A helium gas (ultra-high-purity grade; 100 ml/min) was used as a carrier gas sweeping volatile and gas products out of furnace continuously. Different weight loadings (between five to twenty five mg of sample) was used for to check for mass transfer limitations in the TGA-MS. The effect of mass transfer was negligible since all samples sizes had similar pyrolysis characteristics. A typical amount of biomass used for the other experiments in the TGA was about 10 mg. Each sample was pre-dried in the TGA at 110 °C for one hour. Gaseous products leaving the TGA were analyzed by a quadrupole mass spectrometry (Extorr XT 300 with an electron ionization voltage at 27 eV). SDT Q600 system was also used to collect intermediate solid samples during the pyrolysis. The sample was heated up to the predetermined final temperature at a heating rate of 150 °C min<sup>-1</sup> and a fast air-cooling system to stop the pyrolysis rapidly as soon as it reached the reaction temperature. The weight difference right before and after the cooling step was measured to confirm any further unwanted decomposition. A negligible amount of weight loss (less than 3

wt%) was detected at this step. The intermediate solid products were recovered and stored in a closed ampoule for further analysis.

### **2.2.3.2 Pyroprobe-GC-MS System**

The pyrolysis of lignin and lignin model compound experiments were conducted using a model 2000 pyroprobe analytical pyrolyzer (CDS Analytical Inc.). The pyroprobe was connected to a model 5890 gas chromatograph (GC) interfaced with a Hewlett Packard model 5972A mass spectrometer (MS) to quantify the volatile products. A capillary column (Restek Rtx-5sil MS) was used as a stationary phase and a helium gas was used for an inert pyrolysis gas as well as a mobile phase for the GC analysis. Pyroprobe experiments were also done in a 20 ml glass vial which was soaked in a liquid nitrogen trap to collect the liquid samples. The same heating ramps done in the TGA-DSC experiments were applied to most pyrolysis experiments.

### **2.2.3.3 $^1\text{H-NMR}$ and $^{13}\text{C-NMR}$**

The liquid intermediates from pyrolysis of lignin and lignin model compounds were collected and analyzed by  $^1\text{H-NMR}$  and  $^{13}\text{C-NMR}$ . Samples were dissolved in  $\text{CDCl}_3$  and scanned by magnetic resonance spectrometer (Bruker 400, AV400).  $^1\text{H}$  scan was carried out with a transmitter frequency at 400 MHz with a receiver gain at 362 and dwell time at 60  $\mu\text{s}$ .  $^{13}\text{C}$  signal was collected at a frequency of 100 MHz with a receiver gain at 32768 and dwell time at 20  $\mu\text{s}$ .

### **2.2.3.4 DP-MAS $^{13}\text{C}$ NMR**

Direct polarization-magic angle spinning was used in this work to analyze intermediate solid product samples obtained from TGA. Samples were packed in a 4-mm-diam zirconia rotor with a Kel-F cap and run at a  $^{13}\text{C}$  frequency of 75.47 MHz in a Bruker DSX-300 spectrometer at a spinning speed of 9 kHz for 24h. The  $^{13}\text{C}$  180° pulse length was 8  $\mu\text{s}$  and 90° pulse was 4  $\mu\text{s}$ . The decoupling strength of DP-MAS was 60 kHz.

#### **2.2.3.4 Gel Permeation Chromatograph**

Gel permeation chromatograph was used to measure the molecular weight distribution. Samples were dissolved in tetrahydrofuran (THF) and injected into Shimadzu HPLC system (SIL-20A auto sampler, LC-20AD Solvent Delivery Module, DGU-20A5 Degasser, CTO-20A Column Oven, SPD-M20A UV-Vis detector) with mesopore column from Agilent at a flow rate of 0.5 ml/min. Polystyrene was used as calibration standard and the signal wave length for UV-Vis is 254 nm.

#### **2.2.3.5 FTIR**

FT-IR spectra for intermediate solid products from lignin and lignin model compound pyrolysis were obtained using a Bruker Equinox 55 infrared spectrometer with DRIFTS cell (Praying Mantis™ from Harrick Scientific). The number of scans was set at 100 with a resolution of 4 cm<sup>-1</sup>, over the range 4000 – 400 cm<sup>-1</sup>. Dry powder samples were used directly without dilution in KBr. KBr was used to obtain a background spectrum prior to sample measurements.

#### **2.2.3.6 Total Organic Carbon Analysis (TOC)**

The carbon content of the solid products from pyrolysis was quantified in the TOC analyzer. Solids were combusted under 900 °C in the oxygen flow rate in Shimadzu Solid Sample Module SSM-5000A. Carbon dioxide was quantified with Shimadzu TOC-V CPH. Potassium hydrogen phthalate was used as calibration standard.

### **2.3 Pyrolysis of Lignin**

#### **2.3.1 Thermo gravimetric Analysis**

The pyrolysis behaviours of raw Maplewood, solid lignin residue, and organosolv lignin were measured by TGA as shown in Fig. 11. A significant weight loss by multiple decompositions was observed at a temperature range between 400-1000 K. With a slow heating rate of 1 K min<sup>-1</sup>, decompositions of both Maplewood and solid lignin residue are completed at about 775 K.

However, organosolv lignin shows a slower decomposition and completely disappears at 900 K. The decompositions occurred at higher temperatures for the faster heating rates. During lignin pyrolysis, more than 25% of initial weight was volatilized at a low temperature (<700 K) and a slow weight loss was found at a higher temperature. Only a small fraction (20-30%) of raw Maplewood is converted into the solid intermediate products. The lignin samples produce more solid intermediate products at the faster heating rate. The organosolv lignin produced more solid intermediate products than the solid lignin residue.

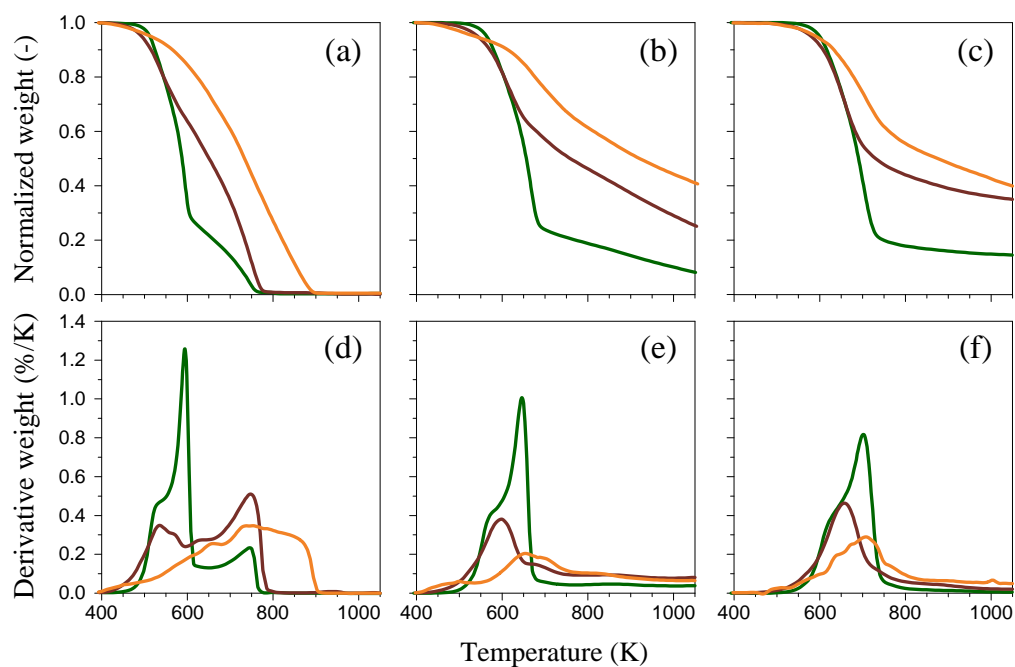


Figure 11. Thermogravimetric and differential thermal curves for pyrolysis study. Maplewood (green), solid lignin residue after enzymatic hydrolysis (brown) and lignin extracted from Maplewood by organosolv method (orange) at heating ramps of 1 (a and d) 15 (b and e) and 150 K·min<sup>-1</sup>(c and f).

A DTG curve for biomass pyrolysis gives another insight into the pyrolysis of each macro component. Hemicellulose and cellulose decompose at 495-590 K and at 590-673 K at 10 K min<sup>-1</sup>, respectively<sup>66,67</sup>. Lignin decomposes at a broad temperature range from 400 to 1273K, which mostly varies depending on the lignin type. The first decomposition peak for Maplewood pyrolysis

at  $1 \text{ K min}^{-1}$  appears around 525 K, and a sharper and narrower peak appears at 590 K. These first two peaks correspond to the decomposition of hemicellulose and cellulose, respectively<sup>68</sup>. With the increase of temperature, the decomposition is continued till it reaches 775 K. The corresponding DTG curve (at 600-775 K) is broad compared to peaks of hemicellulose and cellulose. The maximal decomposition rate at this range shows up at 740-750 K. This matches with those of solid lignin residue and ethanol organosolv lignin. The DTG curve for organosolv lignin shows a wider decomposition pattern at a higher temperature than the solid lignin residue. This implies that a lignin residue is more relevant than organosolv lignin to study the kinetics of lignin in the original biomass.

The pyrolysis of lignin results in a weight loss of sample by releasing volatile products and accumulating a highly carbonized material in a residual solid mixture which we will call polyaromatic char. The polyaromatic char yield from cellulose increases with decreasing temperature or decreasing heating rates<sup>69,70</sup>. The polyaromatics yield from lignin pyrolysis increases with heating rate as shown in Fig. 11. In contrast the polyaromatics yield for cellulose pyrolysis decreases with increasing heating rate. We employed a TGA to collect and characterize three intermediate solid product samples of the solid lignin residue as a function of time at the heating rate of  $150 \text{ K min}^{-1}$  as shown in Fig. 12. Elemental analysis of each sample is summarized in Table 3. The weight percent of carbon in the samples increased with increasing temperature. The weight percent of oxygen and hydrogen in the samples decreased with increasing temperature.

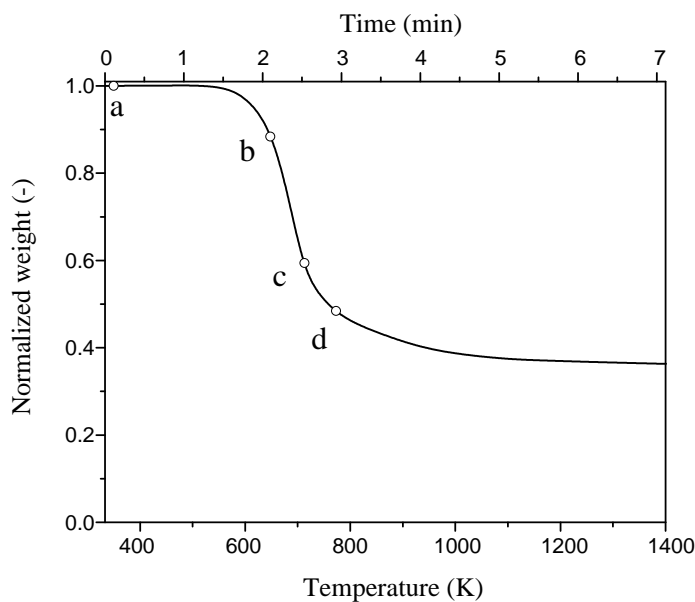


Figure 12. TGA for the pyrolysis of Maplewood lignin residue from enzymatic hydrolysis

More than 40 wt% of lignin residue can be volatilized in the first decomposition step (Shown as point C in Fig. 12). As a result, a significant amount of carbon is concentrated in a solid mixture. Several phenolic compounds are detected as condensable liquid products and their analyses are discussed in the later sections. Carbon monoxide, carbon dioxide and water were the major gases species identified by the MS connected to TGA via a heated line preventing condensation of light molecules.

The effective hydrogen-to-carbon ratio ( $H/C_{eff}$ ) is a measure of the effective amount of hydrogen in a biomass feedstock<sup>71</sup>. The ratio is defined by

$$\frac{H}{C_{eff}} = \frac{H-2O}{C} \quad (1)$$

where H, C, and O are molar number of hydrogen, carbon, and oxygen atoms, respectively.



Table 3 Elemental analysis for original Maplewood lignin and solid products

Sample	C (Wt %)	H (Wt %)	O (Wt %)	H/C <sub>eff</sub>
Organosolv lignin	64.94	5.39	29.67	0.31
Maple Wood	48.59	5.92	45.49	0.06
373 K <sup>a</sup>	58.81	5.70	35.49	0.26
648 K	66.37	4.89	28.74	0.23
713 K	72.20	4.12	23.68	0.19
773 K	74.25	3.60	22.15	0.13
a: pre-dried sample				

Most biomass feedstocks have H/C<sub>eff</sub> ratios lower than 0.5 due to high oxygen contents while petroleum-based feedstocks have the value between 1-2<sup>72</sup>. The Maplewood has a low value, 0.06 due to a high oxygen content. The organosolv lignin has H/C<sub>eff</sub> ratio five times that of original Maplewood. This implies that lignin compounds have a high relative hydrogen content compared to the cellulose and hemicellulose fraction of the biomass. The H/C<sub>eff</sub> ratio in the solid lignin residues decreases with increasing pyrolysis temperature.

The IR spectra of solid lignin residue and its intermediate solid pyrolysis products were measured at room temperature to examine how the functional groups of the solid residue change with temperature as shown in Figure 13. The characteristic wavelengths of various functional groups listed in Table 4. There are two characteristic wavenumber regions (2800-3500 cm<sup>-1</sup> and 600-1750 cm<sup>-1</sup>) that indicative of the structure of lignin and the thermal degradation due to pyrolysis.

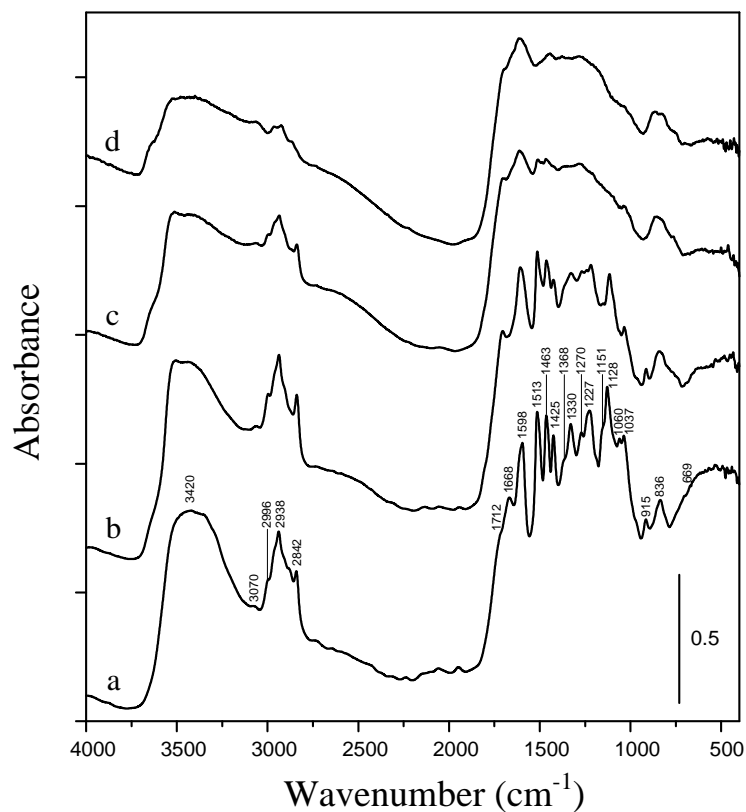


Figure 13. FT-IR spectrum of solid samples. (a) solid lignin residue from enzymatic hydrolysis, and solid product samples obtained at (b) 648 K, (c) 713 K, and (d) 773 K during the pyrolysis at a heating ramp of 150 K min<sup>-1</sup>.

The broad band at 3420 cm<sup>-1</sup> (OH stretching vibration) decreases with increasing pyrolysis temperature. However, this band still exists at higher temperatures. The OH stretching vibration is due to phenolic groups and adsorbed water. The bands at 3070 and 2938 cm<sup>-1</sup> indicate aromatic and aliphatic CH stretching respectively. It is notable that the band at 3070 cm<sup>-1</sup> indicating aromatic CH stretching increases with pyrolysis temperature while the band at 2938 cm<sup>-1</sup> decreases. This implies that the carbon from lignin pyrolysis is accumulated in a form of polyaromatic rings. There was a clear disappearance of the band at 2842 cm<sup>-1</sup> indicating methoxyl group decrease with increasing temperature.

A carbonyl group characterized by bands at 1712 and 1668  $\text{cm}^{-1}$  decreases with increasing temperature. The syringyl and guaiacyl group bands appear at 1330 and 1270  $\text{cm}^{-1}$ , respectively. These two are characteristic bands for lignin compounds. Similar to a previous IR spectral study of lignin pyrolysis<sup>68</sup>, it was observed that the predominant intensities of syringyl and guaiacyl groups disappear first with the pyrolysis temperature increase. This indicates that the mechanism of lignin pyrolysis initially occurs through the loss of ether linkages.

Table 4 Characterization of FT-IR spectrum

Band ( $\text{cm}^{-1}$ )	Characteristics	Changes	Ref.
3420	OH stretching	Decrease	73,74
3070	Aromatic CH stretching	Increase	74
2938	Aliphatic CH stretching	Decrease	
2842	Methoxyl	Disappear	
1712, 1668	C=O stretching (aromatic ring)	Decrease	73
1598, 1513,1425	Aromatic ring vibration	Decrease	73,74
1463,1368	CH deformation	Decrease	73
1330	Syringyl	Disappear	
1270	Guaiacyl	Decrease	
1060,1037	CH & CO deformation	Decrease	
915,836	Aryl CH wags	Persist	74
669	OH out of plane bending	Disappear	

DP-MAS results and the chemical shifts of the major peaks of the solid pyrolysis samples are shown in Fig. 14 and Table 5. Peak 1 belongs to methoxy groups. This peak disappears as the temperature increases. Peak 2 is an overlap of the C $\alpha$ -OR in lignin and CHOH of carbohydrates. We can also see a cellulose peak at 104 PPM (labelled Peak 3). This peak decreases at 648 K, which is the temperature where most cellulose decomposes. The C $\alpha$ -OR peak, which corresponds to  $\alpha$  ether bond, disappears with increasing temperature. The  $\beta$ -O-4 linkage is in the range of 82-86

PPM. We can observe this peak disappear at a temperature of 648 K. Peak 3 in the 98-142 PPM is the nonprotonated aromatic C-C and some carbohydrates peaks. A broad peak, at 98-142 PPM, with an aromatic chemical shift forms at 773K. This demonstrates that the solid left after the lignin pyrolysis has an aromatic-based structure with lots of nonprotonated aromatic C-C bond. Table 6 summarizes the quantitative analysis of lignin characteristic peak during its pyrolysis. The fraction of spectral area for methoxy group decreases from 21.95% to 2.3% as temperature increases while that of the nonprotonated aromatic C-C increases from 31.4% to 61.64%. These results imply that the intermediate solid products obtained from lignin pyrolysis are mainly composed of cyclic polyaromatics. These results are consistent with the work by Sharma et al.<sup>74</sup>. Wang and Low<sup>75</sup> claimed that small reactive fragments (alkene-like compounds) and monomeric aromatic rings are evolved at a lower temperature and form nuclei which could be a precursor of cyclic polycarbon structure. At a higher temperature, these units are further polymerized to form larger polyaromatics. Other researchers<sup>76,77</sup> have concluded that homolytic bond cleavages, such as O-CH<sub>3</sub> and ether bonds, cause radical formation, which subsequently forms polycyclic aromatic ring.

Table 5 NMR chemical shift of solid lignin residue from enzymatic hydrolysis.

Peak Number	Chemical shift (ppm)	Moiety
1	56	Methoxy group
2	73	C <sub>α</sub> -OR of lignin and CHOH of carbohydrates
3	82-86	C <sub>β</sub> -OR of lignin
4	104	OCHO of carbohydrates
5	135	Aromatic carbon
6	147,152	Aromatic C-O

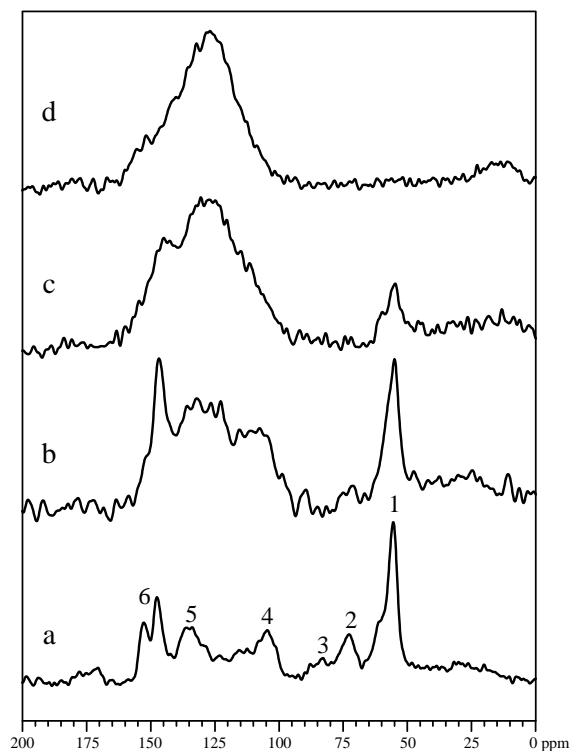


Figure 14. Direct polarization/magic angle spinning (DP/MAS) spectra of solid samples. (a) solid lignin residue from enzymatic hydrolysis, and solid product samples obtained at (b) 648, (c) 713, and (d) 773 K during the pyrolysis at a heating ramp of 150 K min<sup>-1</sup>.

Table 6 Percentage of total spectral area assigned to methoxy group and nonprotonated aromatic carbon

Sample	48-61.2ppm (Methoxy Group)	98-142ppm (Nonprotonated Aromatic C-C)
Hydrolysis residue	21.95%	31.4%
648 K	16.95%	43.34%
713 K	7.17%	52.68%
773 K	2.3%	61.64%

### 2.3.2 Pyrolysis in Pyroprobe

The lignin samples were pyrolyzed in a pyroprobe GC-MS system under three temperatures at a heating ramp of 150 K min<sup>-1</sup>. Table 7 shows the mass balance for pyrolysis of these samples. Between 68 to 93 wt% of the products produced by pyrolysis in the pyroprobe reactor were solids. In general, the pyrolysis of biomass in the pyroprobe produces more coke

than the pyrolysis in a TGA system. This is because a high concentration of pyrolysis vapors form in the pyroprobe which induces further repolymerization or condensation, followed by secondary reaction steps forming gas and coke. Between 0.2 to 6.7 wt% of the products were gases. The detected components in the gas include carbon monoxide, carbon dioxide and water. Liquid products were collected by conducting the experiments in a 20 ml vial that was in a He atmosphere, which was soaked in the liquid nitrogen to condense vapour products. In each experiment, 6 to 24 wt % of liquid products can be collected. A lower amount of liquid and gaseous products were produced from the ethanol organosolv lignin compared to the solid lignin residue.

Table 7. Weight distribution of lignin pyrolysis products from pyroprobe reactor.

T (K)	Solid lignin residue				Ethanol organosolv lignin		
	Gas <sup>a</sup>	Liquid	Solid		Gas <sup>a</sup>	Liquid	Solid
648	1.58	6.11	92.31		0.21	6.49	93.3
713	4.37	8.15	87.48		1.46	8.24	90.3
773	6.73	24.42	68.85		3.09	16.01	80.9
<sup>a</sup> . Estimated by the balance							

Table 8 shows the carbon balance for pyrolysis of the lignin samples in the pyroprobe reactor. The solid products (unreacted lignin and solid polyaromatic products) contained most of the carbon (64-87%). The gaseous products contained less than 6 % of the carbon. Gaseous products mainly contain carbon monoxide and carbon dioxide. Ethanol organosolv lignin had much less gas production than solid lignin residue at the same pyrolysis conditions. 12 to 30 % of carbon was collected as liquid condensates. Table 9 shows the carbon selectivity of each quantifiable product in the liquid sample which are analysed by GC-MS. Carbon selectivity is defined by carbon content in each species divided by the overall carbon amount summed over detectable liquid and unidentified products. We were only able to quantify 14 to 36 carbon % of the products in the liquid product with most of these products being monomeric aromatics. Guaiacol, syringol and vanillic acid are the highest observable detectable compounds even though

each of these compounds has a carbon selectivity of less than 6.0 %. These results agree with the recent analysis of volatile products from lignin pyrolysis reported by Bridgwater et al.<sup>61</sup> They mentioned that unidentifiable products in their analysis are most likely larger molecular weight compounds that are formed from lignin pyrolysis while monomeric products come from the ether bond cleavages in lignin. The ether bond is easy to break due to low dissociation energy. Kawamoto et al.<sup>61</sup> proposed the reaction mechanism that the bond cleavages during lignin pyrolysis results from radical reactions including H-abstraction on phenolic group. They claimed that C<sub>β</sub>-O bond homolysis generating radical species in chain reactions.

Table 8 Carbon balance of lignin pyrolysis products from pyroprobe reactor

Solid lignin residue				
T (K)	Gas <sup>a</sup>	Liquid <sup>b</sup>	Solid	Unidentified <sup>c</sup>
648	0.46	1.73	87.43	10.38
713	5.39	2.67	80.59	11.35
773	6.00	10.68	64.34	18.98
Ethanol organosolv lignin				
T (K)	Gas <sup>a</sup>	Liquid <sup>b</sup>	Solid	Unidentified <sup>c</sup>
648	0.04	0.38	87.18	12.40
713	0.36	1.01	82.90	15.73
773	0.75	4.00	81.94	13.31
a. Gases are a mixture of CO and CO <sub>2</sub> b. Products detected from GC-MS c. Heavy liquid condensates which can't be detected in GC-MS; Carbons are estimated based on the balance				

Table 9 Carbon selectivity of condensed liquid products from a Py-GC-MS analysis

Product	Formula	Solid lignin residue			Ethanol organosolv lignin		
		648K	713K	773K	648K	713K	773K
Furfural	C <sub>5</sub> H <sub>4</sub> O <sub>2</sub>	0.00	0.00	0.00	0.00	0.01	1.59
5-methylfurfural	C <sub>6</sub> H <sub>6</sub> O <sub>2</sub>	0.00	0.00	0.00	0.02	0.01	0.10
Furfural alcohol	C <sub>5</sub> H <sub>6</sub> O <sub>2</sub>	0.60	2.34	1.61	0.00	0.00	0.00
Phenol	C <sub>6</sub> H <sub>6</sub> O	0.00	0.00	0.33	0.00	0.00	0.13
3-Methyl-1,2-cyclopentanedione	C <sub>6</sub> H <sub>8</sub> O <sub>2</sub>	0.00	0.00	0.00	0.02	0.02	0.22
4-methylphenol	C <sub>7</sub> H <sub>8</sub> O <sub>1</sub>	0.00	0.00	0.00	0.00	0.00	0.07
Guaiacol	C <sub>7</sub> H <sub>8</sub> O <sub>2</sub>	0.06	0.18	3.02	0.04	0.08	0.93
Benzoic acid	C <sub>7</sub> H <sub>6</sub> O <sub>2</sub>	0.13	0.10	0.13	0.05	0.10	0.44
2-methoxy-4-methylphenol	C <sub>8</sub> H <sub>10</sub> O <sub>2</sub>	0.21	0.01	1.24	0.12	0.36	1.95
2,3-dimethoxy toluene	C <sub>9</sub> H <sub>12</sub> O <sub>2</sub>	0.08	0.02	1.06	0.00	0.00	0.00
3-methoxy-1,2-benzenediol	C <sub>7</sub> H <sub>8</sub> O <sub>3</sub>	0.36	0.04	2.13	0.00	0.06	0.80
4-Ethyl-2-methoxyphenol	C <sub>9</sub> H <sub>12</sub> O <sub>2</sub>	0.00	0.00	0.00	0.06	0.05	0.70
4-Methylcatechol	C <sub>7</sub> H <sub>8</sub> O <sub>2</sub>	0.00	0.00	0.00	0.05	0.09	0.26
4-hydroxy-3-methylacetophenone	C <sub>9</sub> H <sub>10</sub> O <sub>2</sub>	0.26	0.20	1.55	0.07	0.03	0.41
Syringol	C <sub>8</sub> H <sub>10</sub> O <sub>3</sub>	2.53	2.51	5.76	0.03	0.24	2.67
Vanillin	C <sub>8</sub> H <sub>8</sub> O <sub>3</sub>	1.55	1.18	1.68	0.05	0.18	1.19
Vanillic acid	C <sub>8</sub> H <sub>8</sub> O <sub>4</sub>	2.81	2.00	5.10	0.16	0.61	3.97
1-[4-hydroxy-3-methoxyphenyl]-ethanone	C <sub>9</sub> H <sub>10</sub> O <sub>3</sub>	0.30	0.42	0.90	0.65	0.96	3.27
1,2,3-trimethoxy-5-methylbenzene	C <sub>10</sub> H <sub>14</sub> O <sub>3</sub>	1.94	1.20	3.60	0.04	0.47	1.41
4-methyl-2,5-dimethoxybenzaldehyde	C <sub>10</sub> H <sub>12</sub> O <sub>3</sub>	0.45	0.27	1.27	0.22	0.06	1.66
Diethyl phthalate	C <sub>12</sub> H <sub>14</sub> O <sub>4</sub>	0.55	2.38	1.18	0.00	0.00	0.00
4-hydroxy-3,5-dimethoxybenzaldehyde	C <sub>9</sub> H <sub>10</sub> O <sub>4</sub>	1.01	1.75	1.54	0.59	0.08	0.21
Phenol, 2,6-dimethoxy-4-[2-propenyl]-	C <sub>11</sub> H <sub>14</sub> O <sub>3</sub>	0.85	2.04	1.96	0.68	0.17	0.23
1-[4-hydroxy-3,5-dimethoxyphenyl]ethanone	C <sub>10</sub> H <sub>12</sub> O <sub>4</sub>	0.04	0.64	0.54	0.06	0.16	0.01
1-[2,4,6-trihydroxy-3-methyl]-1-butanone	C <sub>10</sub> H <sub>12</sub> O <sub>4</sub>	0.46	1.62	1.34	1.10	0.10	0.83
Unidentified		85.81	81.1	64.06	95.99	96.16	76.95

Figure 15 shows the reaction pathway of lignin pyrolysis based on our experimental observation. The molecular formula of Maplewood lignin was estimated from the average molecular weight measured by GPC and from elemental analysis of lignin residue. Maplewood lignin undergoes a fast decomposition at a low temperature and produces solid polyaromatic hydrocarbons and volatile products. Overall material and carbon balance equations are used to calculate the stoichiometric



coefficients in the proposed reaction pathways. The major volatile species include gaseous products mainly composed of water, carbon dioxide and carbon monoxide as well as condensable liquid products mainly composed of guaiacol, syringol and vanillic acid. The vapor composition is calculated based on the detectable products accumulated after the pyrolysis of lignin residue from ambient to a high temperature at 773K. The weight fraction converted into volatile species ( $1 - f_p$ ) was about 0.36. This value coincides with the estimated value obtained from the kinetic model fit to dynamic experimental data in TGA which will be discussed in the later. The molecular formula of solid polyaromatic products is calculated based on the Sharma's work<sup>74</sup> and carbon balance of lignin residue pyrolysis at 773 K.

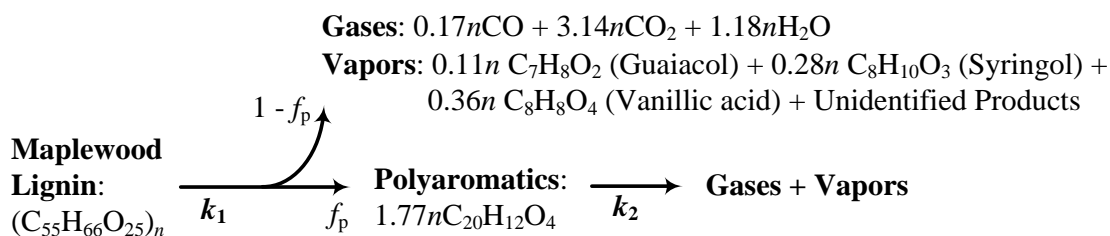


Figure 15 Proposed reaction pathway of lignin pyrolysis

### 2.3.3 Conclusions

We tested two types of lignin extracted from Maplewood (solid lignin residue after enzymatic hydrolysis and organosolv lignin) and compared their pyrolysis behaviours with the Maplewood. For the analysis of pyrolysis product distributions, pyroprobe reactor and TGA system were used to collect intermediate products. The most probable reaction pathways are proposed based on the product analysis and TGA experiments. The kinetic model was developed and compared with the weight changes in isothermal and dynamic TGA-DSC experiments to estimate kinetic parameters and reaction heats for each step.

It was observed that the pyrolysis of lignin involves two series decomposition steps. At the first step, lignin was decomposed into volatiles and solid products, and then further decomposition of solid products occurs at a high temperature above 600 K. The volatile species are comprised of light gases and condensable liquid mixture. The evolution of light gaseous products was measured through Py-GC-MS and TGA-MS. CO, CO<sub>2</sub>, and H<sub>2</sub>O were major gaseous species. Small amounts of H<sub>2</sub> and CH<sub>4</sub> release were also found at the first step when a TGA-MS system was used. A CO<sub>2</sub> release was continued to the decomposition at a higher temperature. Condensable liquid products were captured by a nitrogen trap in a pyroprobe reactor and their concentrations are quantitatively measured as a function of pyrolysis temperature by GC-MS. The condensable liquid species were mainly composed of identifiable monomeric phenolics (14-36 carbon %) and unidentifiable heavy tars. The major detectable products were guaiacol, syringol and vanillic acid which result from the cleavage of ether linkages. When pyrolysis temperature was increased with a heating ramp of 150 K min<sup>-1</sup>, higher carbon selectivity was observed for such monomeric phenolic compounds while that of unidentified heavy tar decreased at below 800 K (or the onset of second decomposition). Non-volatile solid products, polyaromatics, were collected as a solid mixture with unreacted lignin at various pyrolysis temperatures programmed in a dynamic TGA system. Resulting solid mixtures were characterized using several analytical tools including elemental analysis, FT-IR, DP-MAS <sup>13</sup>C NMR, and TOC. Elemental analysis and TOC results showed that a larger amount of carbon transferred to solid mixture and a larger amount of oxygen transferred to volatile species. FT-IR and DP-MAS <sup>13</sup>C NMR analysis of the solid intermediate products indicated disappearance of methoxy groups and accumulation of nonprotonated aromatic C-C bonds with the progress of pyrolysis. From these results, we can conclude that lignin decomposition through pyrolysis occurs primarily based on the cleavage of ether bonds and leaves solid products containing high concentration of aromatic carbons, called polyaromatics.

## **2.4 Pyrolysis of lignin model compound**

The objective of this paper is to study the pyrolysis of an oligomeric lignin model compound that contains  $\beta$ -O-4 linkage. We will compare these model compounds to the pyrolysis of a real lignin sample derived from the enzymatic hydrolysis of maple wood. We will also characterize the products produced from pyrolysis of this model compound and propose a reaction pathway. This paper strives to provide the scientific basis to understand the chemistry of the pyrolysis of lignin.

### **2.4.1 Characterization of oligomeric lignin model compound**

Figures 16 and 17 show the  $^1\text{H}$ -NMR and  $^{13}\text{C}$ -NMR spectrum of the lignin model compound. The acetyl group peak is at 2.0ppm in Figure 16. The methoxyl group peak is around 3.8ppm which shows the same chemical shift as in real lignin<sup>78</sup>. The peaks at 4.6ppm and 6.0ppm demonstrate the existence of  $\text{H}_\beta$  and  $\text{H}_\alpha$ , which proves that the  $\beta$ -O-4 linkage is synthesized. The chemical shift of side chain protons are from 4.0ppm to 5.0ppm. Aromatic peaks are around 7.0ppm. The peak of each carbon in the lignin model compound is labeled in Figure 17. The peaks at 80ppm and 74ppm also indicate a  $\beta$ -O-4 structure in the compound. All the peaks have the same chemical shift as the work of Katahira et al with the exception of an extra peak at 1.3 ppm<sup>65</sup> in Figure 16. This is the peak of tert-butyl group which was not reduced to the hydroxyl group probably due to steric hindrance effects.

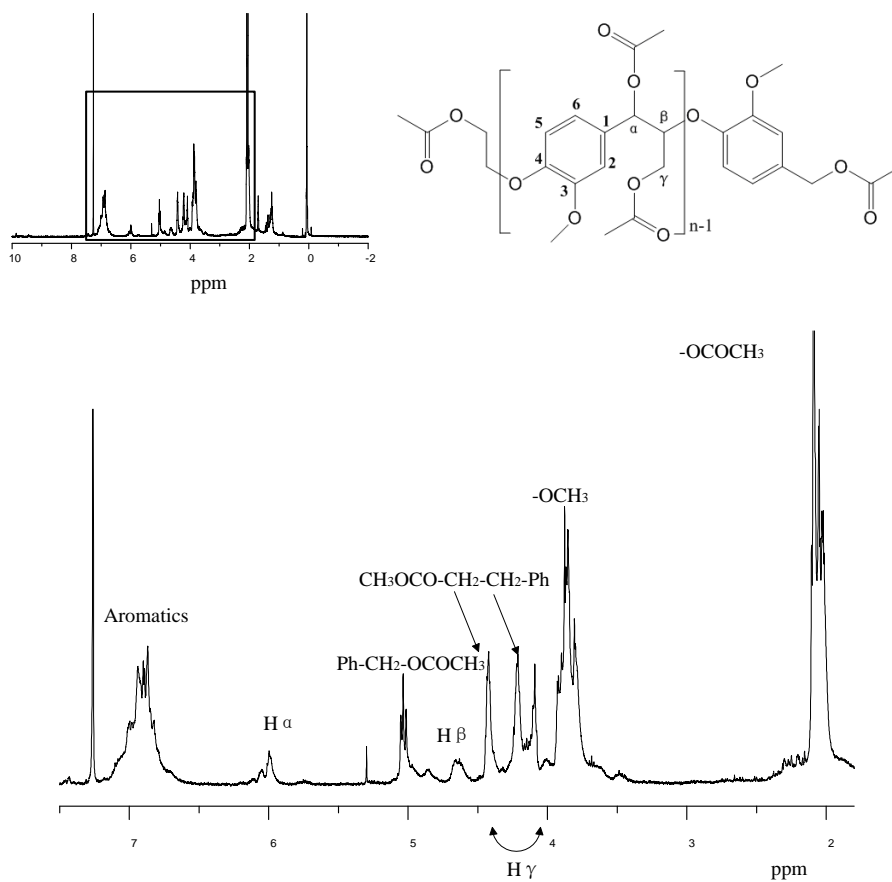


Figure 16  $^1\text{H}$  NMR of  $\beta$ -O-4 lignin model compound

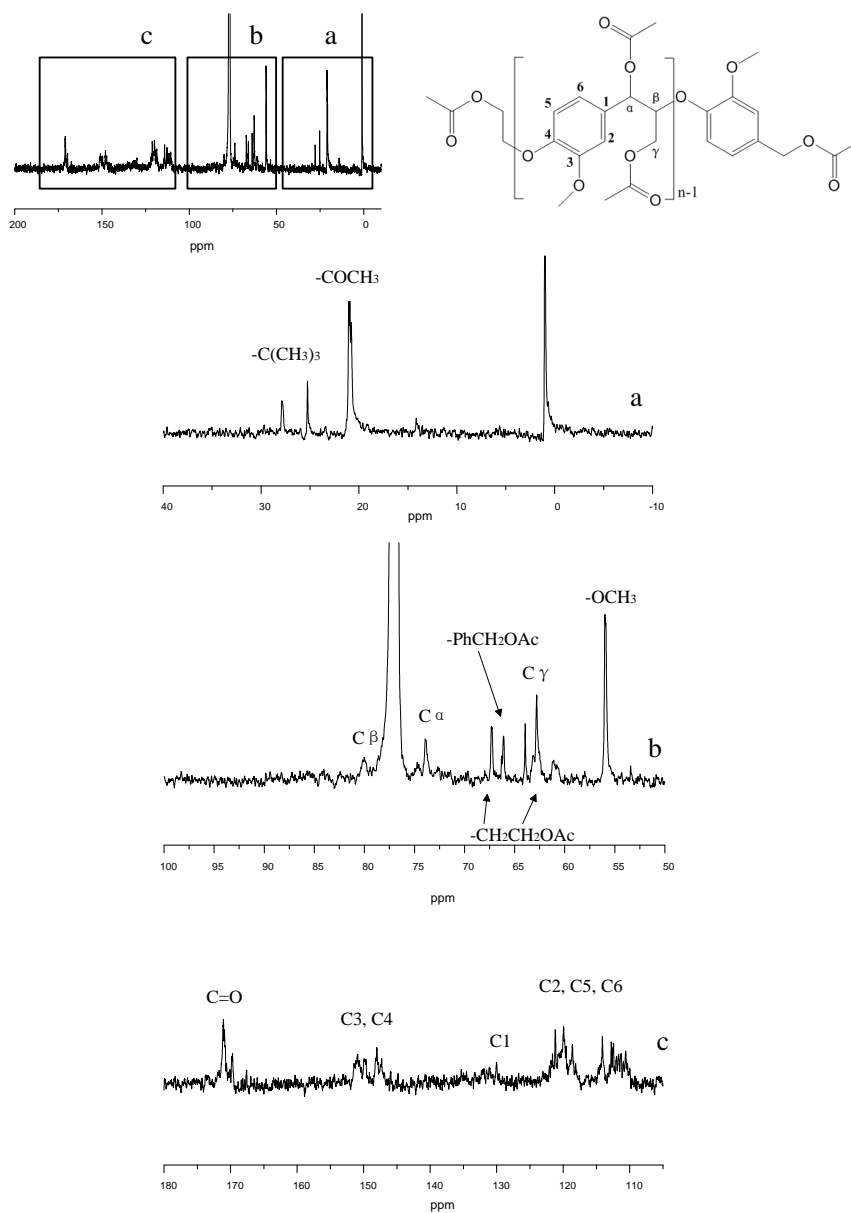


Figure 17  $^{13}\text{C}$  NMR of  $\beta$ -O-4 lignin model compound

Figure 18 shows the GPC data of the lignin model compound. The model compound was soluble in THF. The peak range is from 200Da to 10,000Da. The average number molecular weight ( $M_n$ ) is 1,264Da and the average weight molecular weight ( $M_w$ ) is 1,755Da. The polydispersity is 1.38 and the degree of polymerization is 4.51. D. Meier et al produced pyrolytic lignin from pyrolysis of beech wood at a temperature of 470°C with a molecular weight range from 162 to

50,000 Da<sup>78</sup>. Our lignin model compound is within this Mw range. There is a small peak at Mw of 200 to 300 Da which indicates that a small part of the vanillin-based monomer did not polymerize correctly.

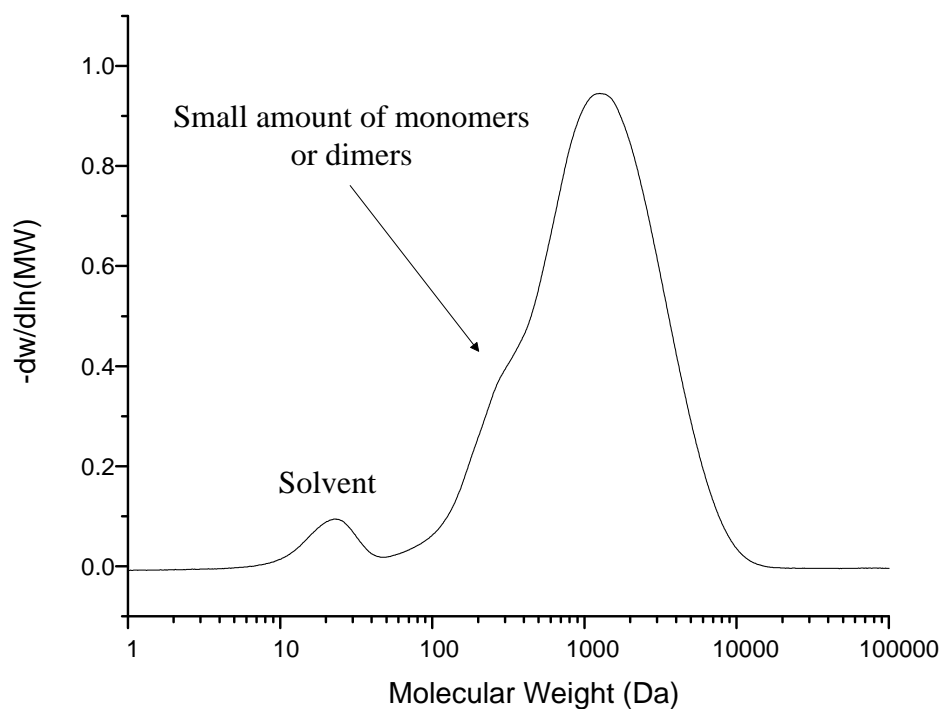


Figure 18 GPC of  $\beta$ -O-4 lignin model compound

#### 2.4.2 Thermogravimetric analysis

The lignin model compound and the lignin residues from enzymatic hydrolysis of maple wood were pyrolyzed in a TGA at different heating rates as shown in Figure 19. The pyrolysis of the lignin residue after enzymatic hydrolysis of maple wood has previously been characterized in detail by Cho et.al<sup>43</sup>. Under a temperature ramp of 1°C/min both the lignin model compound and the lignin residue show different decomposition peaks (Figure 19 (a) and (b)). The lignin model compound decomposes at a lower temperature than the lignin residue. Three major weight losses for the lignin model compound are at peak temperatures of 190°C, 260°C and 550°C whereas lignin residue has two major weight losses at peaks of 260°C and 470°C, respectively. At the temperature ramp of 15°C/min, the weight loss peaks shift to higher temperature (Figure 19 (c))

and (d)). The lignin model compound starts to decompose at 230°C followed by decompositions peaks at 300°C and 650°C. The lignin residue only has one major weight loss peak at 320°C and a very slow decomposition above 400°C. When applying higher temperature ramp (150°C/min), the major decomposition peak for the lignin model compound shifts to 350°C-380°C with a shoulder around 300°C (Figure 19 (e) and (f)). The decomposition at high temperature disappears. The major weight loss for the lignin residue is around 400°C. The lignin model compound decomposes at a lower temperature and faster than the lignin residue (Figure 19 (a), (c) and (e)). Less char forms in the pyrolysis of the model compound than the actual lignin residue. This is due the relatively simpler structure and smaller molecular weight of the model compound. However, the lignin model compound has similar pyrolysis behavior as the lignin residue (Figure 19 (d) and (f)) with the major decomposition for both of them happening in the same temperature region.

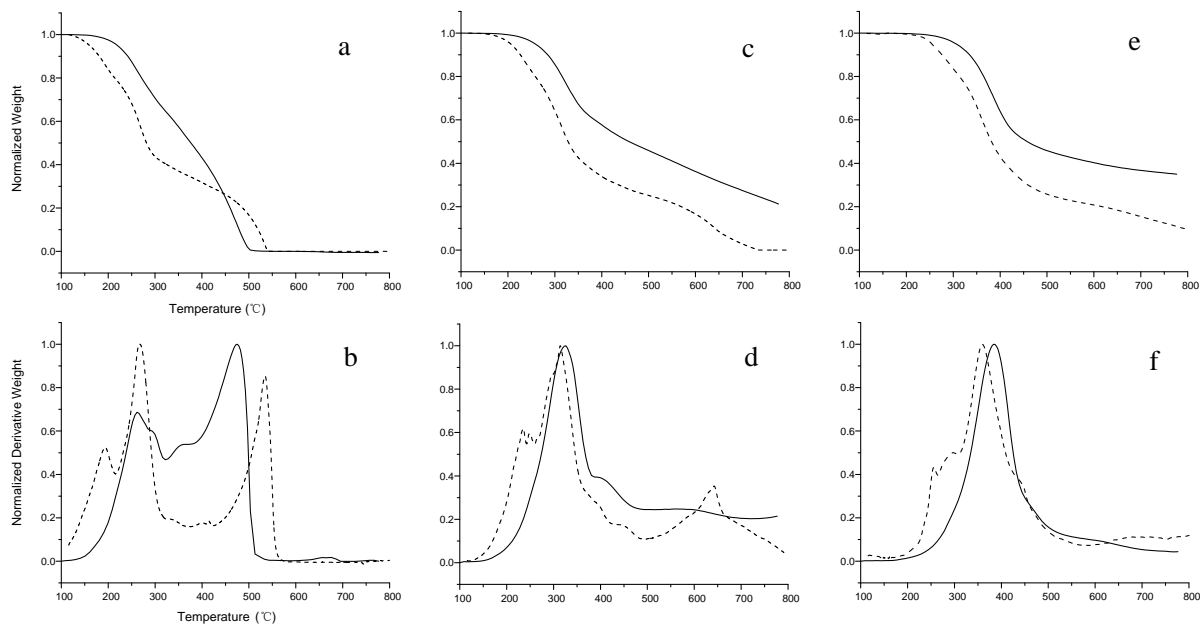


Figure 19 Thermogravimetric and differential thermal curves for the pyrolysis study. Lignin model compound (dash line) and lignin residue after enzymatic hydrolysis (solid line) at temperature ramps of 1 (a and b) 15 (c and d) and 150°C/min (e and f).

The reactions were stopped at different temperatures during the pyrolysis at a temperature ramp of 150 °C/min and the solid products composition was measured. The temperature programming in the TGA was set at four final temperatures (250 °C, 350 °C, 450 °C and 550 °C), maintained this temperature for three minutes and then was cooled down to room temperature. After the reaction, we collected all the products. The products consisted of two phases with one phase which was soluble in a solvent and the other was not. The soluble phase dissolved in an organic solvent such as THF and chloroform are called soluble part of product. The insoluble fraction is named solid char. The pyrolyzed product at 250 °C was completely soluble in the organic solvent (THF or chloroform). The solid black char formation began at the temperature of 350 °C. The products obtained from 450 °C and 550 °C did not dissolve in the organic solvent.

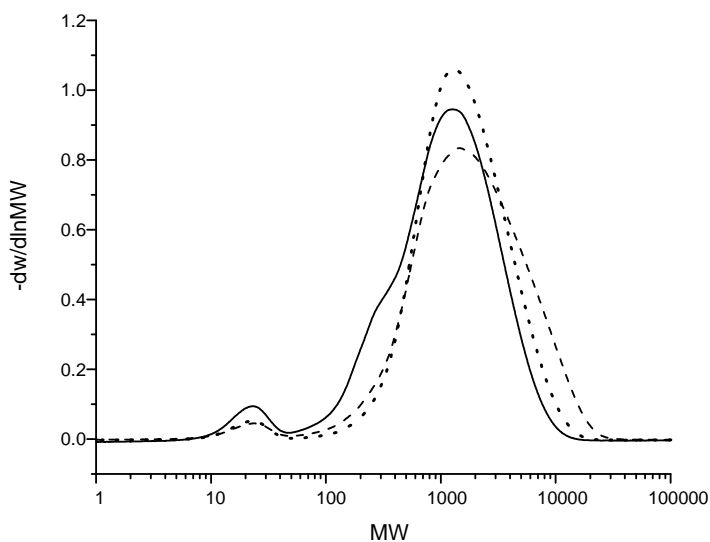


Figure 20 GPC of lignin model compound and intermediate products. Model compound (solid) , product from 250 °C(dash), product from 350 °C(dot).

Figure 20 shows the GPC data for the soluble products. The black line is the original model compound. The low molecular weight disappears at 250 °C indicating that these monomers are very volatile and pyrolyzed at temperatures less than 250 °C. Thus, we can conclude that the first weight loss peak in Figure 19 (b) and (d) at temperatures of 190 °C and 230 °C is caused by the



monomers volatilization. The peak width of the product at the temperature of 250 °C is broader than that of original model compound. This indicates heavier polymers being formed around 250 °C. As the pyrolysis temperature increases to 350 °C, the peak width decreases. This suggests that the heavy polymeric compounds continue polymerizing to form char which doesn't dissolve in THF at the temperature above 250 °C.

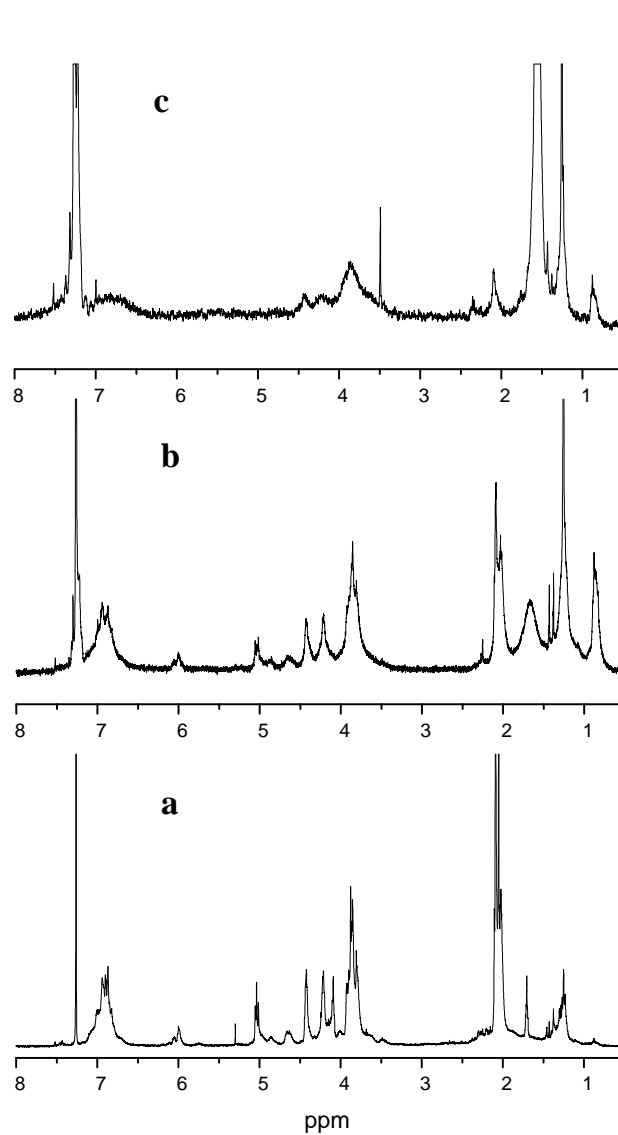


Figure 21 <sup>1</sup>H NMR of lignin model compound and intermediate products. (a) lignin model compound, (b) product from 250 °C, (c) product from 350 °C

The soluble products taken from 250 °C and 350 °C were dissolved in d-chloroform and analyzed by <sup>1</sup>H-NMR as shown in Figure 21. The original lignin model compound and the soluble product obtained from 250 °C have a very similar structure based on the <sup>1</sup>H-NMR spectra. The peak of H<sub>β</sub> at 4.6ppm still exists in the product, which means the β-O-4 linkage of lignin model compound doesn't break below 250 °C. We can also observe the H<sub>α</sub> at 6ppm, which is the proof of the existing C<sub>α</sub>-C<sub>β</sub> bond. There are some changes in the lower chemical shift. This can be explained by aliphatic side chain reactions reacted by unreduced tert-butyl group or monomeric volatilization. The spectrum of sample obtained from 350 °C is shown in Figure 21 (c). Compared with starting materials, the product structure has obviously changed. We cannot observe the peak at 4.6ppm or 6.0ppm which means β-O-4 is cleaved and lignin model compound decomposes around 350 °C. This is consistent with the major weight loss observed in thermal curve at 350 °C (Figure 19 (f)), which is the major reaction stage after the first monomer decomposition stage. From the NMR spectrum, we can conclude the soluble products still contains aromatic based structure with methoxyl group (3.8ppm) and aliphatic side chain (low chemical shift). We also observe water generation at around 1.6ppm.

Solid products were taken from the 350 °C to 550 °C reactions and analyzed by FTIR. The results are shown in Figure 22. Table 10 shows the characterization of peaks in the spectrum. The band at 3471 cm<sup>-1</sup> represents the –OH stretch and it decreases in size from 350 °C to 550 °C (Figure 22 (b) to (d)). However, a small proportion of this band still exists in the sample collected at higher temperature suggesting it still contains hydroxyl groups in the product structure. The bands of –CH stretch in aliphatic chain and methoxyl group are at 2940 cm<sup>-1</sup> and 2840 cm<sup>-1</sup>, respectively. These bonds also decrease with increasing temperature. A small amount of aliphatic stretching exists in the sample collected at higher temperature. The carbonyl group in the lignin model compound shows at the band of 1740 cm<sup>-1</sup>. This peak decreases and almost disappears in the

sample pyrolyzed at higher temperature. The aromatic ring vibration bands appear at a range from 1400  $\text{cm}^{-1}$  to 1600  $\text{cm}^{-1}$ . In the lignin model compound(Figure 22 (a)), the aromatic ring vibration peaks are separate. However, the peaks merge to a broad band in the sample collected at higher temperature which implies that a polyaromatic structure forms. The typical guaiacol band appears at 1226  $\text{cm}^{-1}$ . This peak is in the original compound but disappears in the solid products. The deformation of C-H bond in aromatic ring is at 1032  $\text{cm}^{-1}$ . This band also disappears when the pyrolysis temperature is above 350 °C. This indicates the formation of a nonproton polyaromatic ring. It is noticed that obvious changes happen to the solid structure from 350 °C to 450 °C which indicates the major reaction happens in this temperature range, which corresponds to the huge weight loss in Figure 19 (f). From the previous work of lignin pyrolysis, a polycyclic aromatic hydrocarbon structure has been identified to form at higher temperature<sup>46</sup>. It is clearly observed that even with a simple lignin model compound with a single type of linkage, we observe similar char formation as has been observed in pyrolyzing lignin.

Table 10 Characterization of FTIR spectra of lignin model compound

wave number ( $\text{cm}^{-1}$ )	characteristics
3471	OH group
2940	CH (aliphatic and aromatic)
2840	CH (methoxy group)
1740	C=O group
1592	Aromatic ring vibration
1513	Aromatic ring vibration
1422	C-H deformation and aromatic ring vibrations
1373	OH in-plane bending and CH bending
1226	Guaiacol unit(G ring and C=O vibrations)
1141	Guaiacol unit(CH in-plane deformation)
1032	Aromatic C-H deformation and C-O,C-C stretching

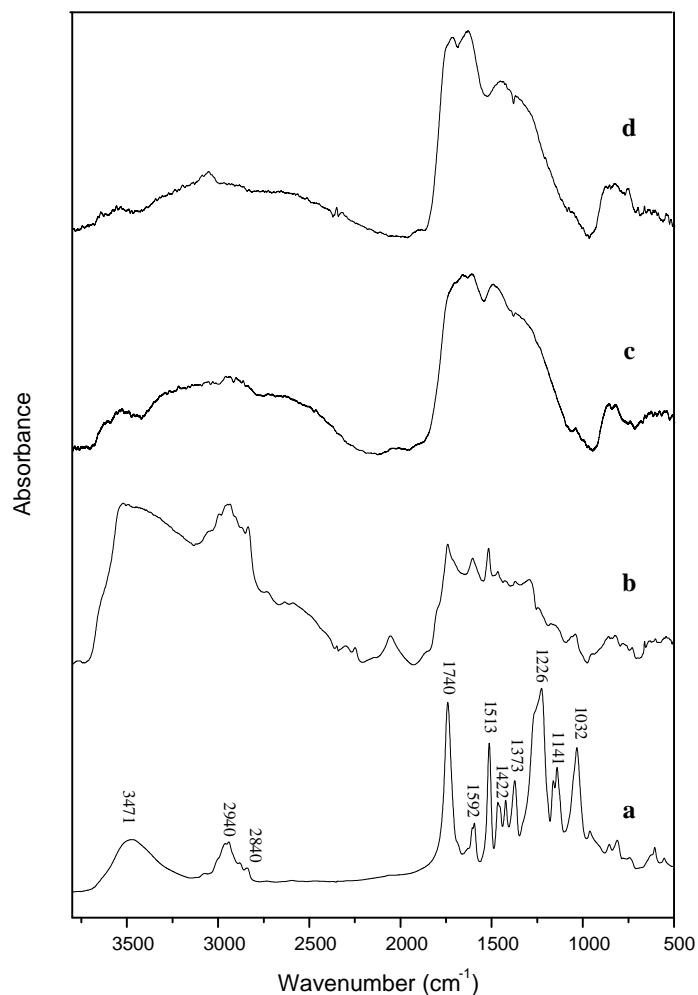


Figure 22. FTIR spectrum of lignin model compound and solid residues. (a) lignin model compound (b)350 °C, (c)450 °C, (d)550 °C.

The gas phase species produced from pyrolysis in the TGA were measured with mass spectroscopy. The major species observed including water (MW = 18), carbon monoxide (MW = 28) and carbon dioxide (MW = 44). Figure 23 shows these products as a function of reaction temperature at a temperature ramp of 15°C/min. Water is produced primarily at a temperature range of 350 °C-400 °C. This corresponds with the -OH peak decreasing in solid char (Figure 22 from b to c). A small amounts of water is also produced at higher temperature. A large amount of carbon dioxide is observed at temperatures from 600 °C to 800 °C. The mass charge ratio of 28 represents carbon monoxide and it increases with temperature until it reaches a plateau. This is

probably caused by char reduction and water gas shift reaction. However, we cannot detect other species in our system due to the low concentration of products.

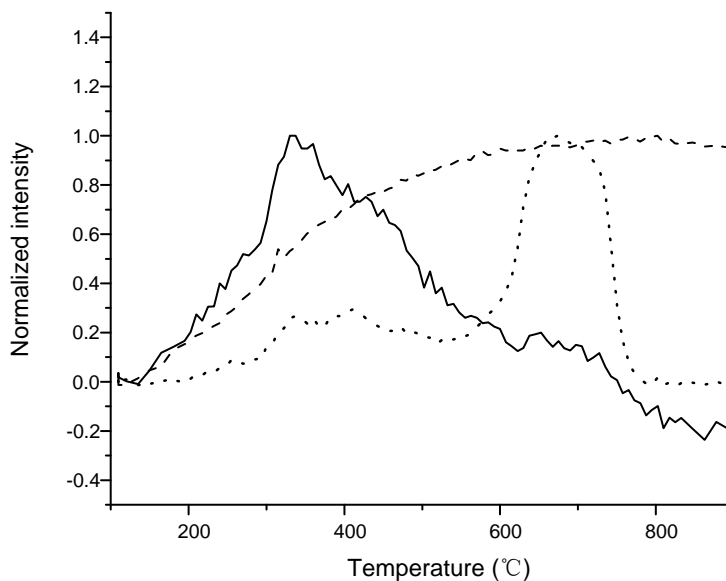


Figure 23: Mass spectroscopy of mass to charge ratios in TGA. Solid-18, dash-28, dot-44.

### 2.4.3 Pyroprobe GC-MS Analysis

Detailed product distributions for pyrolysis of the lignin model compound were collected by pyroprobe-GC-MS system. Table 11 shows the mass balance of pyrolyzing lignin model compounds at a temperature ramp of 150 °C/min. A fast temperature ramp of Table 11. Mass balance of pyrolysis of lignin model compound in pyroprobe at temperature ramp of 150 °C/min. 1000 °C/s was also applied as comparison. We report our products in four different categories: gas, liquid, solid and unidentified. Gas mainly consists of carbon monoxide and carbon dioxide. Liquid products contain all the species detected by GC-MS except gas products. These liquid compounds are mainly mono aromatics. Solid products were the char collected after the reaction and burned to analyze carbon content by TOC. We also report the unidentified products, which are most likely heavier molecular weight compounds that cannot be detected by GC-MS. Only 0.1 wt% to 4.3 wt% gas was observed with carbon dioxide being the major gas product. As the

temperature increases, the ratio of carbon monoxide to carbon dioxide decreases. The yield of liquid product reaches a maximum (about 60 wt%) at 550 °C. The oligomeric lignin model compound produces more liquid products than lignin<sup>19</sup> due to its simpler structure, lower heat resistance and higher reactivity. The amount of char formation decreases at the higher temperature. At the highest temperature, it has 30wt% char formation. In the previous TGA results, we observe around 30 wt% and 20 wt% char formation at 450 °C and 550 °C, respectively (Figure 19 (e)). However, in the pyroprobe the char yield is 50 wt% and 30 wt% at the corresponding temperatures. The probe has poorer mass transfer properties than the TGA which most likely increases the rate of secondary reactions that form coke compared to the TGA.

Table 11. Weight balance of pyrolysis of lignin model compound in pyroprobe

Temperature (°C)	Gas	Liquid	Solid	Unidentified
250	0.10% (1:4.8)	11.80%	74.10%	14.00%
350	2.20% (1:5.1)	20.40%	66.30%	11.10%
450	3.40% (1:5.4)	40.40%	50.30%	5.90%
550	4.30% (1:8.9)	59.70%	28.30%	7.70%
() designate weight ratio of carbon monoxide to carbon dioxide				

Table 12 shows the carbon balance of pyrolysis in the pyroprobe. The solid product contains 30% to 75% of the carbon from the lignin model compound. This indicates the solid product is highly carbon concentrated. The gas products have less than 2% of total carbon content. The carbon in liquid products increases from 9% at lower temperature to 46% at higher temperature. When applying the fast pyrolysis at 550 °C, the carbon content in the liquid decreases while the carbon content in the unidentified products increases. The lignin model compound has a similar weight and carbon distribution as lignin produced from maple wood by hydrolysis<sup>45</sup>. However, lignin residue has more char formation.

Table 12. Carbon balance of pyrolysis of lignin model compound in pyroprobe

Temperature (°C)	Gas	Liquid	Solid	Unidentified
250	0.42% (25%:75%)	8.91%	86.19%	4.48%
350	1.00% (23%:77%)	16.06%	71.13%	11.81%
450	1.49% (22%:78%)	31.97%	64.75%	1.79%
550	1.85% (15%:85%)	46.34%	48.93%	2.88%

( ) designate ratio of carbon selectivity of carbon monoxide to carbon dioxide

Table 13 shows the carbon selectivity of the liquid products detected by Pyroprobe-GC-MS under different temperatures at a temperature ramp of 150 °C/min. We were able to detect more than 25 distinct peaks in the GC-MS. As shown in Table 4, most detectable liquid products are mono aromatics with different functional groups and side chains. These compounds are listed by their abundance. Acetic acid is the most abundant product being produced from the acetyl group. The most abundant monomeric aromatic is vanillin, which is the monomer used to produce the model compound. Some of the compounds in Table 13 had a low similarity with the GC-MS library indicating that there are some uncertainties in whether or not we correctly identified these compounds.

Table 13. Carbon selectivity of liquid products detected by Py-GC/MS

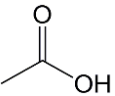
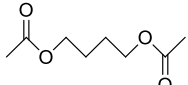
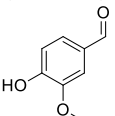
Compound	250°C	350°C	450°C	550°C	550°C <sup>[a]</sup>	S <sup>[b]</sup>	F <sup>[c]</sup>
acetic acid 	42.6%	32.2%	34.5%	22.1%	16.3%	91	1,3
1,4-butanediol diacetate 	8.3%	21.7%	12.2%	7.8%	9.1%	90	(a)
4-hydroxy-3-methoxybenzaldehyde (vanillin) 	21.8%	8.3%	9.1%	7.6%	8.2%	97	1,4

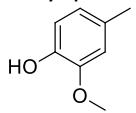
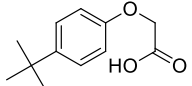
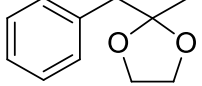
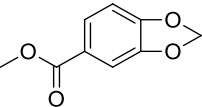
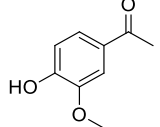
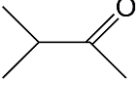
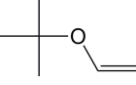
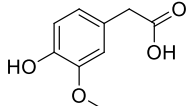
Table 13 – Continued							
2-methoxy-4-methyl phenol 	5.7%	0.9%	3.0%	7.1%	6.7%	96	1,3
(4-Tert-butylphenoxy)acetic acid <sup>[d]</sup> 	6.1%	2.5%	7.5%	7.2%	8.6%	72	
1,3-dioxolane,2-methyl-2-[phenylmethyl] <sup>[d]</sup> 	0.8%	3.3%	2.6%	6.7%	8.1%	40	
1,3-benzodioxole-5-carboxylic acid, methyl ester <sup>[d]</sup> 	0.7%	3.8%	3.1%	6.3%	4.7%	59	
1-[4-hydroxy-3-methoxyphenyl]-ethanone <sup>[d]</sup> 	2.1%	8.2%	4.9%	4.9%	6.0%	58	
3-methyl-2-butanone <sup>[d]</sup> 	4.3%	2.5%	3.4%	1.9%	0	35	
2-(ethenyloxy)-2-methylbutane <sup>[d]</sup> 	4.7%	7.5%	5.8%	2.1%	3.3%	14	
4-hydroxy-3-methoxy- benzene acetic <sup>[d]</sup> 	1.6%	1.2%	2.4%	2.4%	2.7%	50	



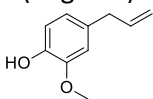
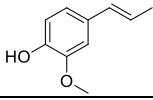
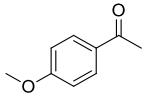
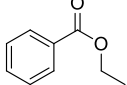
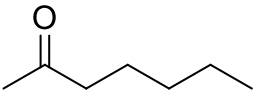
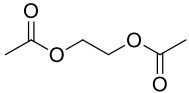
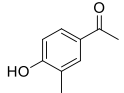
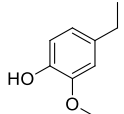
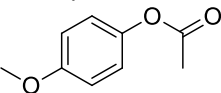
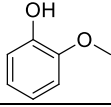
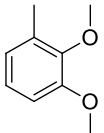
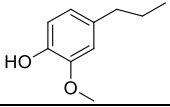
Table 13 – Continued							
4-Allyl-2-methoxyphenol (eugenol) 	1.0%	1.8%	1.0%	1.4%	3.2%	97	(d)
2-methoxy-4-[1-propenyl]-phenol 	0	1.7%	4.5%	3.8%	4.4%	95	(c)
1-[3-methoxyphenyl]-ethanone 	0	0.8%	2.4%	0.4%	0.6%	86	
benzoic acid, ethyl ester 	0	1.5%	0.4%	0.2%	0.06%	94	
2-heptanone <sup>[d]</sup> 	0	0.7%	0.7%	0.8%	0.8%	50	
1,2-Ethanediol diacetate 	0	0.2%	0.6%	0.7%	0.5%	83	(b)
4-hydroxy-3-methylacetophenone 	0	0.9%	0	5.9%	5.0%	83	
2-methoxy-4-ethyl-phenol 	0	0.1%	0	4.6%	4.2%	91	
4-methoxy-acetate phenol 	0	0	1.7%	0.07%	0.23%	81	

Table 13 – Continued							
2-methoxyphenol (guaiacol) 	0	0	0	4.9%	5.7%	95	1,2
2,3-dimethoxy toluene 	0	0	0	0.7%	0.6%	91	
2-methoxy-4-propyl-phenol <sup>[d]</sup> 	0	0	0	0.4%	1.1%	59	1,6,7
[a] Designating temperature ramp is 1000°C/s. [b] S designates similarity search from MS library. [c] F designates the bond cleavage or reaction number this compound comes from in Figure 9. [d] Designating mass spectrometry has low identity on this compound and we may not observe.							

Compare with the dimeric model compound, the reaction network of pyrolyzing oligomeric model compound is much more complicated, which adds many uncertainties when we try to propose the reaction pathway. Free radical with concerted reactions have been proposed in PPE. However, in the presence of oligomeric structure and acetyl groups, there can be various possibilities for the reaction pathways. We propose one possible free radical reaction dominant pathway (Figure 24) based on the major products observed in Table 13. A free radical chain mechanism can be drawn to explain the thermal decomposition of the lignin model compound. Previous studies have indicated that the  $\beta$ -O-4 bond cleavage happens at relatively low temperature because of its low dissociation energy<sup>79,80</sup>. This is in agreement with our FTIR and NMR results discussed above. Radicals are generated after  $C_{\beta}$ -O homolysis cleavage. This is

believed to be the initiation step for free radical chain reaction<sup>81</sup>. In Figure 10,  $\beta$ -O-4 linkage breaks (cleavage 1 in Figure 24) between the temperature 250 °C and 350 °C in our experiment. The radicals can abstract the proton from other species which have weak C-H or O-H bonding (such as C<sub>6</sub>H<sub>5</sub>-OH) and form products. Vanillin and 2-methoxy-4-methyl phenol being the two most abundant monomeric aromatic products are produced by  $\beta$ -O-4 bond cleavages and H-abstraction. This indicates the bond cleavage tend to happen at 1, 3 and 4 positions in Figure 24. The radicals are passed to other species for further reaction leading to chain propagation. We observe large amount of acetic acid and 1,4-butanediol diacetate formation. This implies the C-O bond at 4 and 7 positions can easily break. When two radicals collide with each other, they form products and terminate the chain reaction such as Reaction (a) and (b) in Figure 24. Some products in Table 13 were not identified with a high similarity by GC-MS. These compounds are not shown in Figure 24. Secondary reactions can also happen. Usually, the radical species are highly active as well as their side chains. H-abstraction, double bond formation, rearrangement and isomerization diversify the products distribution<sup>63</sup> such as reaction (c) and (d) in Figure 24. From the mass and carbon balance in Table 11 and 12, we observe that the solid products contain about 50% of carbon content in original lignin model compound. This is a similar result to what we have observed in our previous study on pyrolysis of a lignin residue<sup>43</sup>. Even though we used relatively simple structure model compound in this work compared with lignin residue, char formation is still a dominant process. Char most likely forms from polymerization of smaller radical species such as aromatics, alkanes and alkenes (reaction (e) in Figure 24). The reaction propagates with more radicals causing further polymerization (reaction (f) in Figure 24). Polyaromatic char finally forms after the elimination of functional groups such as hydroxyl and methoxyl groups

It would be desirable to inhibit radicals chain propagation reactions and prevent repolymerization during lignin pyrolysis to decrease the char formation and increase the bio-oil

production. This could be done by one of two methods: 1) by converting the lignin products before they undergo free radical reactions or 2) by the addition of free radical inhibitors. From the proposed reaction chemistry, a hydrogen donor would be effective to stop the chain reaction after the initial bond break. Both intermolecular and intramolecular H-abstraction can achieve this. The weak C-H or O-H bond such as aldehyde and phenol could be taken into consideration to provide the proton. Other free radical inhibitors including nitrobenzene, butylated hydroxyl toluene or diphenyl picryl hydrazyl have shown the ability to stabilize the resonance of the radicals. A persistent radical would be another alternative. When the monomer lacks protons, it can easily abstract them from persistent radical to terminate the reaction. However, these compounds could introduce unwanted elements into the pyrolysis process. Moreover, the free radical inhibitors need to be in intimate contact with the lignin and not degrade at the temperatures of the lignin pyrolysis. More work is needed before lignin can effectively be decomposed into fungible fuels and chemicals.

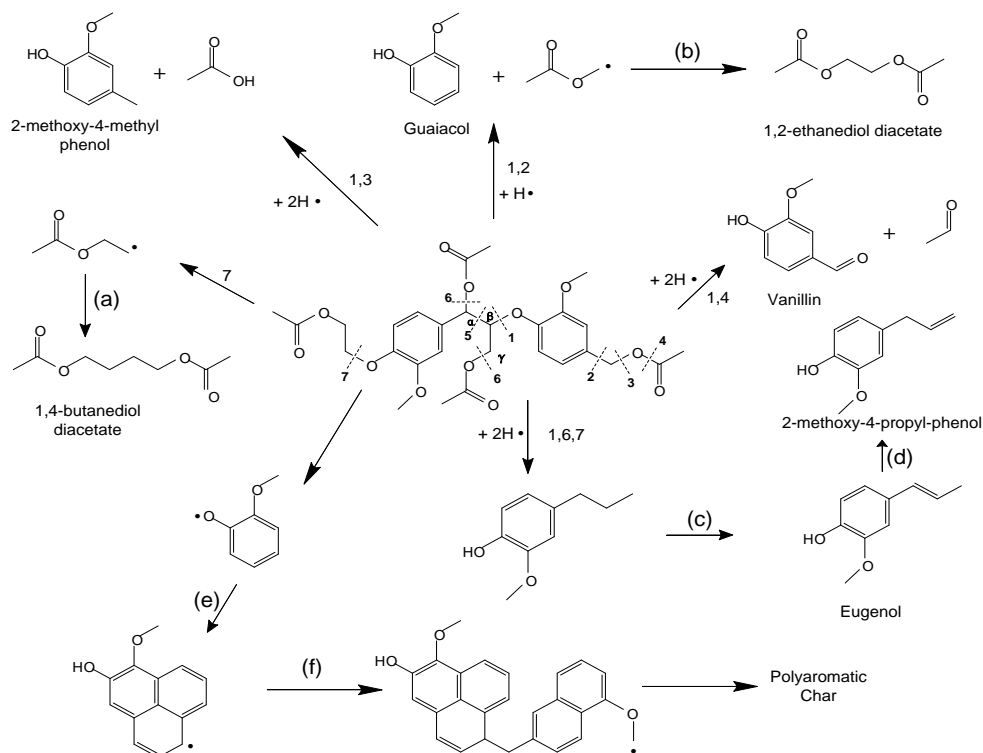


Figure 24: Proposed reaction mechanism of pyrolysis of lignin model compound

## 2.4.4 Conclusion

An oligomeric lignin model compound, which only contains  $\beta$ -O-4 linkages, was synthesized using t-butoxycarbonylmethyl vanillin as the polymerization monomer. The average molecular weight is around 1250Da. The oligomeric lignin model compound shows similar thermal decomposing temperatures as the lignin residue derived from maple wood. The lignin model compound decomposes around 300 °C and 380 °C under temperature ramps of 15 °C/min and 150 °C/min, respectively.  $^1\text{H-NMR}$  is applied to trace the structure changes of soluble part of pyrolyzed products.  $\beta$ -O-4 linkage is thermally cleaved at the temperature between 250 °C and 350 °C. A solid product is observed at the temperature of 350 °C. At higher temperatures, polyaromatic char forms. The major product from pyrolysis of this lignin model compound is solid char which accounts for 50-70 % of the carbon. Volatile monomeric aromatic compounds are

quantified by GC-MS and vanillin is the most abundant product. The chemistry of pyrolyzing lignin model compound can be explained by a free radical reaction mechanism. Various products are formed by bond cleavages and secondary reactions. Randomly repolymerized radicals are believed to cause char formation.

## CHAPTER 3

### REENGINEERED FEEDSTOCK™ FOR COAL COMBUSTION EMISSION CONTROL

Non-recyclable paper and plastic waste are utilized to produce refused derived fuel (RDF). The combination of RDF and flue gas desulfurization sorbent forms an innovative product called Re-Engineered Feedstock™ (ReEF). ReEF is designed to co-feed with coal in power plants to produce energy while remove the SO<sub>x</sub> from coal combustion. The performance of ReEF on capturing SO<sub>x</sub> from coal combustion were studied in a lab scale fluidized bed combustor and drop tube reactor. The system construction and experimental results are presented in this chapter.

#### 3.1 Introduction

##### 3.1.1 Refused Derived Fuel (RDF)

Municipal solid waste (MSW) mainly consists of paper, plastics, food wastes, glass, metals, rubbers, yard trimmings, and woods. The collected wastes are processed in material recovery facilities. Refused derived fuel (RDF) refers to the combustible fraction recovered from mixed MSW<sup>82</sup>. The main compositions of RDF are paper, plastic and biodegradable waste. The processes that recover RDF from MSW involve series of screening, separation and size reduction. The key function of the processes is the separation between combustible components and non-combustible components. In industry, the major application of RDF is utilized as a fuel supplement for coal fired power plants. To achieve a higher energy density, drying and pelletization is required in RDF production. When using as a fuel supplement, the heating value of RDF usually between 12 MJ/kg and 16 MJ/kg which contributes up to about 30% of the energy input<sup>82</sup>. The contaminants in the wastes could be transferred to RDF, which would lead to emission problems when RDF is subjected to burning. Typically, RDF contains materials having high concentration of chlorine like PVC. In the combustion, chlorine is converted to HCl, which could cause corrosion.

Moreover, the presence of chlorine in the combustion atmosphere can lead to the formation of polychlorinated dibenzo-p-dioxins (PCDDs) and polychlorinated dibenzofurans (PCDFs), which are reported as probable carcinogens. Another disadvantage of RDF production is the fact that more cost is associated with pre-treatments to recover the fuels.

### **3.1.2 Co-firing coal and RDF**

Coal combustion remains and is predicted to be an important process for electricity production in the United States and many countries around the world for the foreseeable future<sup>83</sup>. The United States produces approximately seven quadrillion BTUs of electrical power per year from coal, constituting 42% of all electrical energy being produced in the country in 2011<sup>84</sup>. However, coal power plants produce gases such as SO<sub>x</sub>, NO<sub>x</sub> and HCl, which can lead to environmental problems including formation of acid rain. Power stations that use coal boilers exhibit typical stack flue gas concentrations before scrubbing of 200-2000 ppm SO<sub>2</sub>, 50-100 ppm CO, 800 ppm NO<sub>x</sub><sup>85</sup>, which are many orders of magnitude higher than permitted by regulation<sup>86,87</sup>. Increasingly restrictive regulations, such as the Clean Air Act, mandate the reduction of emissions from coal combustion facilities.

The process of converting the waste to energy is considered to be one of the promising method to achieve maximum energy recovery and environmental sustainability. RDF produced from MSW is commonly used as a second fuel to be co-fired with coal in a power plant. The combustion performance and emission of co-firing RDF and coal have been studied extensively in the last decades<sup>88-99</sup>. The technology has been gained wide attentions for the benefits in replacing fossil fuels, mitigating greenhouse gas and enhancing the waste management.

Co-firing coal and RDF can reduce the CO<sub>2</sub> emission from the fossil fuel for the reason that RDF is considered to be a CO<sub>2</sub> neutral fuel. Moreover, the low sulfur content in the RDF leads to the lower SO<sub>2</sub> emission. However, other pollutants such as hydrogen chloride (HCl) need to be



concerned when combusting RDF due to the existence of polyvinyl chloride (PVC)<sup>100-102</sup>. Cl<sub>2</sub> and Cl emitted from the fuel is also an important factor for forming the polychlorinated dibenzo-p-dioxins and dibenzofurans (PCDD/Fs)<sup>103,104</sup>. To achieve the regulated emission level, the addition of a third component is required to decrease the pollutants emissions by sequestration within the ash. Commonly, calcium based sorbents such as calcium oxide, calcium hydroxide and calcium carbonate are proved to be effective on removing the SO<sub>2</sub> emission<sup>105-109</sup>. Recently, the studies shows by injecting the calcium sorbents the HCl emission from the RDF can also be reduced<sup>102,110,111</sup>. However, the process of removing the emissions requires to build the scrubbing facilities in the downstream of a power plant, which increases the capital and operation cost for the plant.

### **3.1.5 ReEngineered Feedstock™**

Although a number of processes exist for cleaning the sulfur dioxide emissions to lower level (e.g. wet scrubbing), the addition of new chemical processing equipment to existing systems will introduce new costs, more water consumption, and decreased energy efficiency. A transformational idea is to develop an energy-rich coal co-reactant from post-recycled materials which can be utilized in existing coal combustion facilities as both a fuel substitute and a sorbent for harmful process emissions. A new coal-reaction technology is proposed and named ReEngineered Feedstock™ (ReEF) which can be directly co-fired in existing coal combustion systems. Co-combustion of ReEF can replace up to 30% of coal with post-recycled materials in existing pulverized coal combustion facilities. Additionally, the ReEF combines sorbents (e.g. Ca(OH)<sub>2</sub>) as part of an engineered fuel which can serve to neutralize emissions such as SO<sub>2</sub>. Utilization of ReEF eliminates the need for additional downstream capital investment in emissions control unit operations as well as eliminating the need for millions of gallons of fresh water.

ReEngineered Feedstock™ was prepared and processed by the ReCommunity Inc. The process consists of two broad phases: the Multi-Material Processing Platform (MMPP) and Advanced Product Manufacturing (APM). The municipal, institutional, and commercial waste stream are collected and pre-sorted at Material Recovery Facility (MRF). After the presorting, the material enters MMPP. It is shredded and sent through a fiber separator to extracted fibers. The optical sorting station removes remaining rigid plastics, container and old newspapers for recycling. The remaining non-recycling fibers are sent to a fluidized bed separator to remove all the heavy inert and non-combustibles. The pure fibers are then sent to the fiber silo. The non-fiber stream is exposed to a drum separator, a magnetic separator and an eddy current separation to recover all recyclable metals. The remaining waste is then sent to an optical sorter to separate out high density polyethylene (HDPE), polyethylene terephthalate (PET) and about 80% of polyvinyl chloride (PVC) for recycling. The remaining post-sorted plastics will be subjected to a two steps thermal treatment to remove all the chlorine in the plastics. This two-step process will bring the concentration of chlorine down to a level which is comparable to other fuels. The remaining non-recyclable plastics are sent to a fluidized bed separator to separate the hard and soft plastics. After the completion of the MMPP, three streams of non-recyclable fiber, hard plastics and soft plastics are obtained. They are free from any non-combustible materials, inert residues and ready to be process in the Advanced Product Manufacturing (APM). In the APM process, a certain type of sorbent is synthesized into the profile of hard plastics to ensure the sorbents are effectively distributed across the ReEF profile. Then the desired amounts of fibers and plastics are mixed with the hard plastics and sorbent. After thoroughly mixed, the material is then pelletized<sup>112–115</sup>.

In this thesis, the ReEngineered Feedstock™ was comprehensively characterized. A bottom feeding co-combustor was constructed to investigate the effects of co-feeding ReEF

materials with coal on the sequestration of pollutants in flue gas, such as SO<sub>2</sub> and NO<sub>x</sub>. The desulfurization behavior of ReEF particles without coal combustion was tested under a series of reaction conditions in a drop tube reactor. The study aims at revealing the advantages of ReEF in capturing sulfur dioxide and potential utilization as a fuel substitute and sorbent of emission control in an industrial scale.

### **3.1.3 Flue Gas Desulfurization**

Sulfur dioxide is generated from coal power plant by combusting sulfur-containing coal. The emission of sulfur dioxide is one of the major pollutant and has significant impacts to the human health and environment. Inhaling sulfur dioxide can cause respiratory symptoms and disease or even premature death. The formation of acid rain is mainly due to the primarily emission of sulfur dioxide. Currently, the regulation on SO<sub>2</sub> emission from EPA is 75 ppb in averaging 1 hour for primary standard and 0.5 ppm in averaging 3 hours for secondary standard<sup>86</sup>. Commercialized technologies of flue gas desulfurization includes wet, spray dry and dry scrubber. With more and more strict regulation on sulfur dioxide control, significant investment is required downstream of the emissions stack to remove it to below regulated levels.

Three major technologies (Wet, Spray dry, and Dry Scrubber) are applied in the industry to remove sulfur dioxide in the flue gas. In a wet scrubber system, flue gas is ducted to a spray tower where an aqueous slurry of sorbent is injected into the flue gas. Sulfur dioxide dissolves into the slurry droplets where it reacts with the sorbents. Typical sorbent material in the wet scrubber is limestone or lime. It is been proved that applying the wet scrubber technology can achieve a sulfur dioxide removal efficiency greater than 95%.<sup>116,117</sup> However, it requires high initial investment and water disposal. Spray dry scrubber, or semi-dry systems, inject an aqueous sorbent slurry similar to a wet system but with higher concentration of sorbent. As the slurry contacts with flue gas, the water in the slurry is evaporated. The sulfur dioxide reacts with water

vapor to form sulfite and then contacts with dry sorbent to form sulfate. In a lot of cases, the water remains on the solid sorbent can enhance the reaction. The products from after the reaction are usually in solids. And it can be removed or collected by a baghouse or ESP. The efficiency of sulfur dioxide removal for spray dry scrubber is usually between 80% and 90% which is a little bit lower than wet scrubber. Application of a single spray dry scrubber is limited to a power plant less than 200 MW. For large power plant, it may requires multi spray dry scrubbers. In the dry system, the sorbent is directly injected into the furnace, the economizer or downstream ductwork. The temperature of furnace injection is over 900 °C. The sorbent decomposes fast into porous materials with high surface area. The capture of sulfur dioxide will lead to a product layer of sulfate formation which causes the pore closure, which prevents the gas transports into the particle for continuous reaction. Due to this, the utilization of the sorbent in dry injection is relative low. This requires an excess amount of sorbent injected into the system to meet the removal regulation. Sulfur dioxide removal efficiencies are significantly lower than other two system, between 50% and 80%.<sup>116</sup> However, dry injection is easy to install and use less space. It is economically favorable for the small scale combustion power plant or combusting low sulfur-containing coal.

### **3.1.4 Sorbents for Flue Gas Desulfurization**

Traditional sorbent materials used for desulfurization are typically alkali and alkaline-earth compounds, including lime ( $\text{CaO}$ )<sup>108,118-121</sup> or hydrated lime ( $\text{Ca(OH)}_2$ )<sup>122-125</sup>, calcium carbonate ( $\text{CaCO}_3$ )<sup>126-129</sup>, sodium bicarbonate ( $\text{NaHCO}_3$ )<sup>130-133</sup>, and others. The natural limestone is very inexpensive and control efficiencies could achieve about 90% sulfur dioxide removal. Lime is the mixture of calcium oxide and calcium hydroxide. It gives higher sulfur dioxide removal efficiency comparing to limestone. However, it significantly cost more<sup>116</sup>. Some modified lime or limestone are developed through the special material preparation<sup>134-136</sup>. The modified sorbents

have high surface area and total pore volume (eg. Sorbacal SP). This will maximize the efficiency of sulfur dioxide capture.

Other than calcium based sorbents, sodium based compounds (sodium bicarbonate, sodium hydroxide, trona) are also commonly used in the flue gas cleaning process. Sodium bicarbonate decomposes to sodium carbonate and subsequently reacts with sulfur dioxide to form sodium sulfate. Generally, the reaction temperature for sulfur dioxide removal (About 300 °F)<sup>137</sup> is much lower than that of calcium sorbents. Trona is a naturally occurring mineral and has a formula of  $\text{NaHCO}_3 \cdot \text{Na}_2\text{CO}_3 \cdot 2(\text{H}_2\text{O})$ . It is composed of approximately 46% sodium carbonate ( $\text{Na}_2\text{CO}_3$ ) and 36% sodium bicarbonate ( $\text{NaHCO}_3$ ). Similar as sodium bicarbonate, trona will decompose into sodium carbonate upon heat treatment<sup>138</sup>. Compared with sodium bicarbonate, trona costs less due to its abundant in the nature. It is reported that sodium bicarbonate can achieve a higher degree of desulphurization (>90%), while the hydrated lime desulphurization efficiency in dry conditions is in the range of 30–80%<sup>132</sup>.

### **3.2 Fluidized Bed Combustion**

This part of work focuses on demonstration and optimization of the efficiency of ReEngineered Feedstock for emission control of coal combustion. A lab scale fluidized bed combustor was constructed capable of evaluating the performance of ReEF for the key emissions in the order of importance. Four types of ReEF containing various sorbents (two sorbents are calcium based and the other two sorbents are sodium based) were pre-mixed with coal and sent into the combustor from the bottom. The results indicate that combining ReEF with coal provides significant improved emissions control with significant  $\text{SO}_2$  reduction in flue gas emission up to 85%. Meanwhile, a slight decrease in NO emission is observed. The results are very promising for the industrial scale application of co-firing coal and ReEF.

### 3.2.1 Materials

The elemental analysis of four pulverized Re-Engineered Feedstock (ReEF) materials were tested by Galbraith Inc. and listed in Table 14. Compared with coal, ReEF, like other biomass, has higher volatile matter and less fixed carbon. The content of nitrogen and sulfur in ReEF is order of magnitude lower than those in coal, which will lead to a lower emission of SO<sub>x</sub> and NO<sub>x</sub>. The higher ash content in ReEF is mainly due to the added inorganic sorbent. The heat of combustion for ReEF is about half of that of coal. Thus, to ensure a certain energy output, only a portion of coal can be replaced by ReEF. Other than proximate and ultimate analysis on the ReEF. We also perform the analysis on the metal elements. The major metal element is calcium and sodium, which is from the sorbents added into the ReEF. Other than those, silicon, chlorine, aluminum, magnesium, iron, and potassium are detected in the ReEF. These metals are probably from the waste stream<sup>99</sup>.

Table 14: Elemental analysis of Coal and ReEF

Sample	Proximate Analysis (wt%)				Ultimate Analysis (wt%)					Heat of Combustion
	Moisture	Volatile Matter	Fixed Carbon	Ash	H	C	N	O	S	Btu/lb
coal	2	33.13	57.2	7.7	5.4	75.3	1.8	8	1.7	13607
ReEF SL <sup>a</sup>	1.24	59.67	5.33	33.7	5.0	33.8	0.06	26.1	0.04	5787
ReEF ML <sup>b</sup>	2.39	49.9	15.13	32.5	5.2	29.0	0.05	33.0	0.04	5546
ReEF SB <sup>c</sup>	7.79	55	9.51	27.7	4.9	36.5	0.09	30.8	0.04	6018
ReEF Trona <sup>d</sup>	9.52	52.32	9.51	33.6	5.0	34.9	0.07	26.3	0.05	5538

a. Sorbocal lime—high surface area hydrated lime  
b. Mississippi lime—standard hydrate lime  
c. Sodium bicarbonate  
d. Pre-milled Trona

ReEF was thoroughly mixed with pulverized coal in different mass ratios prior to use, as shown in Table 15 along with the properties of ReEF including weight percent of components in ReEF and weight percent of ReEF combined with pulverized coal. ReEF content in coal/ReEF mixture are recommended by the ReCommunity Inc. from 26 wt% to 37 wt%. The energy content of coal/ReEF mixture is approximate 30 kJ/g, which is similar to that of the bituminous coal. ReEF is compared with each independent sorbent, including Sorbocal lime, Mississippi lime, sodium bicarbonate and pre-milled Trona, a naturally occurring mixture of sodium bicarbonate and sodium carbonate. Table 15 shows the sorbent cation-(Ca, Na)-to-sulfur ratio for mixtures and the weight percent of sorbent in the mixtures of pure sorbent with coal.

Table 15: Properties of ReEF and sorbent feedstock

Sample	ReEF SL	ReEF ML	ReEF SB	ReEF Trona	Coal
Fibers (wt%)	52	52	53.6	49.6	0
Hard plastic (wt%)	13	6.5	6.7	6.2	0
Soft plastic (wt%)	0	6.5	6.7	6.2	0
Sorbent (wt%)	35	35	33	38	0
ReEF ratio <sup>a</sup> (wt%)	26	26	35	37	0
Mixture energy (kJ/g)	30.4	30.4	29.5	29.1	31.6
Sorbent type	Sorbocal lime	Mississippi lime	Sodium bicarbonate	Pre-milled Trona	None
Sorbent formula	Ca(OH) <sub>2</sub>	Ca(OH) <sub>2</sub>	NaHCO <sub>3</sub>	Na <sub>3</sub> (CO <sub>3</sub> )(HCO <sub>3</sub> )•2H <sub>2</sub> O	None
Molecular weight (g/mol)	74	74	84	226	0
Cation/S ratio <sup>b</sup>	Ca/S=3.1	Ca/S=3.1	(Na/2)/S=2	(Na/2)/S=2.8	0
Sorbent ratio <sup>c</sup>	11	11	15	18	0
a. ReEF ratio in coal/ReEF mixture (wt%), recommended by ReCommunity b. Sorbent cation (Ca, Na)-to-sulfur ratio for coal/ReEF mixture and coal/sorbent mixture c. Calculated sorbent ratio in coal/sorbent mixture, wt%					

### 3.2.2 Experimental Apparatuses and Procedure

To demonstrate the effectiveness of ReEF co-feeding with coal, a fluidized bed combustion (FBC) reactor was constructed as shown in the Figure 25 schematic of the reactor and

analytical system. A 5.0 cm inner-diameter alumina tube (99.8%, CoorsTek Inc.) was the main reactor inside a high temperature furnace, which can withstand high temperatures up to 1650 °C. The alumina tube was 100 cm in length with 80 cm placed inside the heated zone during operation. Three thermocouples (type B, Pt/30%Rh-Pt/6%Rh) were placed into the combustor tube from top to bottom to measure the temperatures at each of three thermal zones. A distributor plate (316 stainless steel mesh) was welded to a stainless steel tube, 3.8 cm in diameter and 15 cm in length. The distributor plate/tube assembly was inserted into the bottom of the reactor tube and tightly sealed using a wrap of alumina insulation fabric. The top of the distributor plate was approximately 2.5 cm below the reactor inlet port of the feeder auger. The alumina reactor tube was sealed at both ends outside the furnace by water-cooled o-ringed flanges. A three-temperature zone furnace was purchased from Applied Test Systems Inc. (Series 3320 split furnace with Watlow EZ-Zone temperature controllers).

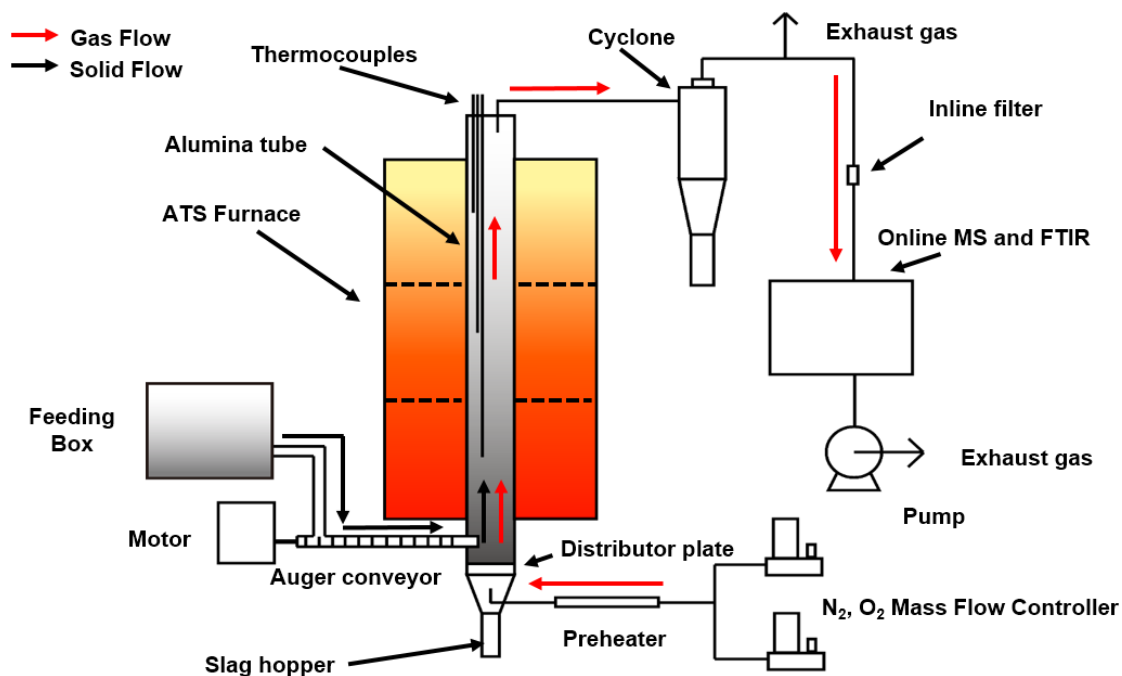


Figure 25: Schematic of Fluidized Bed Combustion Reactor set up. (a) a flow diagram of the combustion system; (b) a 3D rendering of the reactor.



The solid feed train consisted of a Schenck AccuRate® feeder (where the feedstock was stored) equipped with a 0.32, 0.95 or 1.27 cm helix auger (depending on the feed type), a drop tube, and a main auger driven by a DC motor at ~50 RPM. Two augers were necessary to avoid reaction within the feed train and plugging; the feeder controllably metered out solid feed, which fell through the drop tube, while a second fast auger rapidly pushed feedstock into the reactor just below the hot zone of the furnace. A cooling copper coil was wrapped around the main auger tube to prevent early pyrolysis and combustion due to the high temperature at the bottom of the reactor. Fluidizing gas consisting of synthetic air was supplied by parallel mass flow controllers (Brooks Inc.) and preheated to 400 °C using resistive heating tape with temperature control (Watlow PID temperature controller). Heated gas entered the bottom of the reactor below the distributor plate. The gas flowed up, reacted with the solid feedstock and exited from the top to a cyclone system to separate fly ash. During reaction, ash dropped through the distributor plate to the slag hopper. One stream of the flue gas coming out of the cyclone was sent to the online analytical equipment by a vacuum pump. The sampling line had two stainless steel filters (Swagelok, 0.2 and 1 µm pore size) to remove any remaining particles in the sampled gas and prevent the analytical equipment from solid contamination.

The combustion conditions are listed in Table 16 and Table 17. In experimental trials, the bottom zone was set to 1200, 1400 or 1600 °C, and the middle zone set to 1100, 1320, or 1550 °C, respectively. The top zone was kept unheated, except by thermal conduction from the lower two furnace zones and convection of the up-flowing gases. To heat up the reactor from room temperature to experimental conditions, a slow heating/cooling ramp (10 °C/min) was employed to avoid cracking of the reactor tube due to rapid thermal expansion/contraction. During combustion, a temperature gradient of approximately 200 °C existed from the bottom to the top

of the tube. The applied temperature gradient was similar to that exhibited in industrial coal combustion boilers. In each run, the feeding rate was varied from 0.50 g/min to 0.61 g/min according to the feed type and maintained 5.0 L/min synthetic air, resulting in about 21% to 46% excess air through the reactor. Control, monitoring and data capture of the gas flows and reactor temperatures was achieved using LabVIEW virtual instrument. All set points were continuously logged. Each test occurred for about 40 to 60 minutes, and the collected data were analyzed at steady state conditions. Solid slag and fly ash were collected after the reactor was cooled down.

Table 16: Temperature profile of the combustion reactor.

Temperature	Setting Value (°C)			Process Value <sup>a</sup> (°C)			Measured Value <sup>b</sup> (°C)		
	Case 1	Case 2	Case 3	Case 1	Case 2	Case 3	Case 1	Case 2	Case 3
Top Zone	0	0	0	1050	1275	1507	1033	1215	1421
Middle Zone	1100	1320	1550	1100	1320	1550	1118	1314	1530
Bottom Zone	1200	1400	1600	1200	1400	1600	1201	1397	1595
a. The temperature was from furnace outside the reactor									
b. The temperature was from thermocouples inside the reactor									

Table 17: Gas flow rate and feeding conditions for combustion.

Feed type	Air flow rate (mL/min)	Argon flow rate (mL/min)	Feed rate (g/min)	Excess air (%)
coal	5000	20	0.50	21.1
coal/ReEF SL	5000	20	0.50	38.0
coal/ReEF ML	5000	20	0.50	40.0
coal/ReEF SB	5000	20	0.50	43.6
coal/ReEF Trona	5000	20	0.50	46.0
coal/SL	5000	20	0.56	21.1
coal/ML	5000	20	0.56	21.1
coal/SB	5000	20	0.59	21.1
coal/Trona	5000	20	0.61	21.1

### 3.2.3 Analytical Methods

Sampled flue gas circulated through an infrared spectrometer (MKS MultiGas 2000), followed by flow through a heated sampling line from the outlet port of the spectrometer cell to

a residual gas analyzer. The IR gas cell had a path length of 5.11 meters and 200 mL volume, with antireflection coated ZnSe windows. The gas cell was maintained at a constant 191 °C for comparison to gas concentration standards. The residual gas analyzer was a MKS Cirrus 2 model of quadrupole mass spectrometer with 200 amu mass range.

The crystalline structure of slag samples was determined using X-ray diffraction (XRD, a Philips powder diffractometer, model X'Pert system), with CuK $\alpha$  radiation ( $\lambda = 1.54 \text{ \AA}$ ) and an X'Celerator detector. An accelerating voltage of 45 KeV was used at a current of 40 mA. Patterns were obtained at a scan speed of  $(2\theta) 7.73^\circ/\text{min}$ . Slag samples were finely ground to ensure random orientation of the crystals so that there were detectable signals at all angles. Also, slag powder was compacted between two glass slides, so that the plane of the powder was aligned with the holder surface.

### **3.2.4 Results and Discussions**

#### **3.2.4.1 Mechanism of Co-combustion of Coal and ReEF**

The proposed mechanism of integrated sorbents/RDF in ReEF for co-combustion with coal is illustrated in Figure 26. As solid feed and reactant gas enter the bottom of the reactor, the fibers and plastics in ReEF and coal are combusted. Then ReEF fragments travel upward, sorbents are released to capture SO<sub>2</sub> flue gas, and any remaining residues continue to combust. Within the convection zone, sorbents undergo desulfurization of the flue gas where complete burnout and conversion are achieved. Optimal ReEF design minimizes sintering of the sorbent early in the

reactor while maximizing gas absorption later at lower temperatures before exiting as gas/solid products.

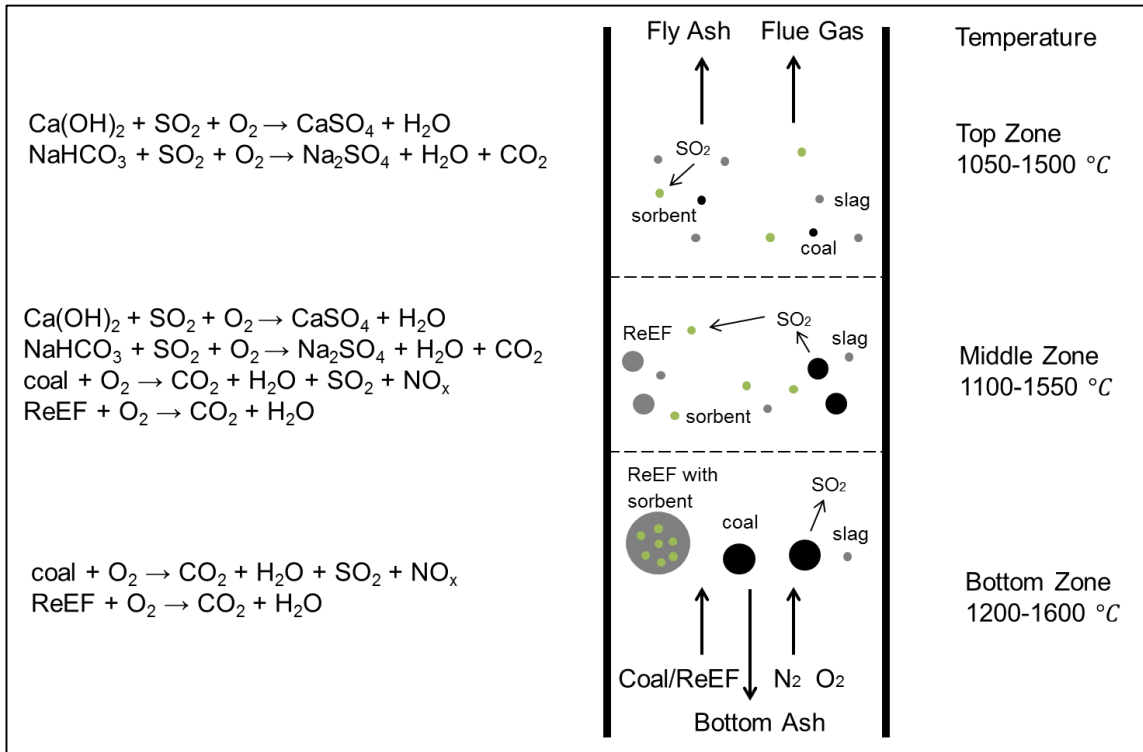


Figure 26. The mechanism of co-combustion of coal and ReEF materials.

### 3.2.4.2 Combustion Efficiency

First, we check the combustion efficiency to see how effectively the heat content of coal/ReEF mixture is transferred into usable heat. As flue gas oxygen or carbon dioxide concentrations are primary indicators of combustion efficiency, we calculate carbon conversion from effluent CO<sub>2</sub> and CO concentrations of the combustion of coal and coal/ReEF mixtures, as shown in Equation 2.

$$\text{Carbon Conversion} = \frac{\text{Carbon in CO}_2 \text{ and CO from measurement}}{\text{Total carbon content in feedstock}} \quad (2)$$

Carbon monoxide emissions ranged between 4 and 6000 ppm for all five blends and comprised less than 2% of carbon content in the feedstock, making CO a minor product compared

with CO<sub>2</sub>. The results of carbon conversion are compared in Figure 27. At 1400 °C and 1600 °C, carbon conversion during combustion is higher than that at 1200 °C. By the combination of coal with ReEF, the efficiency of each coal/ReEF mixture combustion generally increases in contrast to pure coal combustion due to the fact that fibers and plastics are easy to combust than coal<sup>92</sup>. Carbon conversion of mixtures with Na-based sorbent raised by 20-30%, implying that it burned more efficiently than mixtures with Ca-based sorbent. This may be attributed to the degree of excess air, which was 43-46% for coal/ReEF SB and coal/ReEF Trona compared with only 21% for coal. At 1200°C and 1400°C combustion efficiency of coal/ReEF ML was higher than that of coal/ReEF SL by as much as 15%.

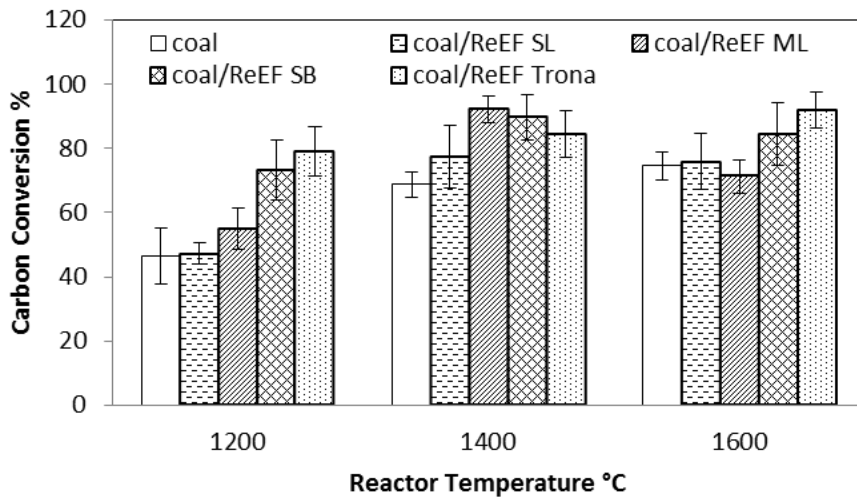


Figure 27. Carbon conversion of coal and coal/ReEF mixtures combustion

One challenge for efficient combustion of coal/sorbent mixtures may result from sorbent melting. For example, mixtures of coal with Na-based sorbent agglomerate at all three temperatures, since the melting point of sorbents are quite low (50 °C for NaHCO<sub>3</sub> and 70 °C for Trona). As reported in literature for sodium bicarbonate, sintering occurs at temperatures above

316 °C<sup>130</sup>. In experiments, coal/sorbent mixtures with Na-based sorbent fed through the hopper and feed screw more smoothly than mixtures with Ca-based sorbent. Despite these issues, high combustion efficiency of ReEF/coal mixtures indicates that ReEF can be mixed with coal in pulverized coal combustors and achieve the objective of steady-state combustion for energy production.

### **3.2.4.3 Sulfur Dioxide Reduction**

Generation of SO<sub>2</sub> flue gas strongly depended on the addition of sorbent, sorbent type, and reaction temperature. To evaluate SO<sub>2</sub> removal efficiency for each ReEF, we defined SO<sub>2</sub> reduction by Equation 3.

$$\text{SO}_2 \text{ reduction} = \frac{\text{Theoretical SO}_2 \text{ emission from combusted feedstock} - \text{Measured SO}_2 \text{ concentration}}{\text{Theoretical SO}_2 \text{ emission from combusted feedstock}} \quad (3)$$

Desulfurization performance of coal/ReEF and coal/sorbent mixtures are shown in Figure 28, with SO<sub>2</sub> flue gas concentration for pure coal combustion ranging 600~800 ppm from 1200 °C to 1600 °C. By co-firing with ReEF, SO<sub>2</sub> emissions are reduced to less than 200 ppm. Calculated SO<sub>2</sub> reduction results in Figure 28 (d-f) demonstrate significant removal of SO<sub>2</sub> emission in combustion flue gas by ReEF, with 70~85% of SO<sub>2</sub> reduction achieved for each temperature. However, only minor differences of SO<sub>2</sub> reduction was observed between four coal/ReEF mixtures. For example, the maximum difference is 15% between coal/ReEF SL and coal/ReEF SB at 1200 °C (Figure 28 (d)). For ReEF sorbents, adsorption capacity did not significantly vary with temperature. Whereas, at 1200 °C and 1600 °C, Na-based sorbents (Figure 28 (f)) demonstrate a measureable advantage on SO<sub>2</sub> reduction relative to Ca-based sorbents (Figure 28.(e)).

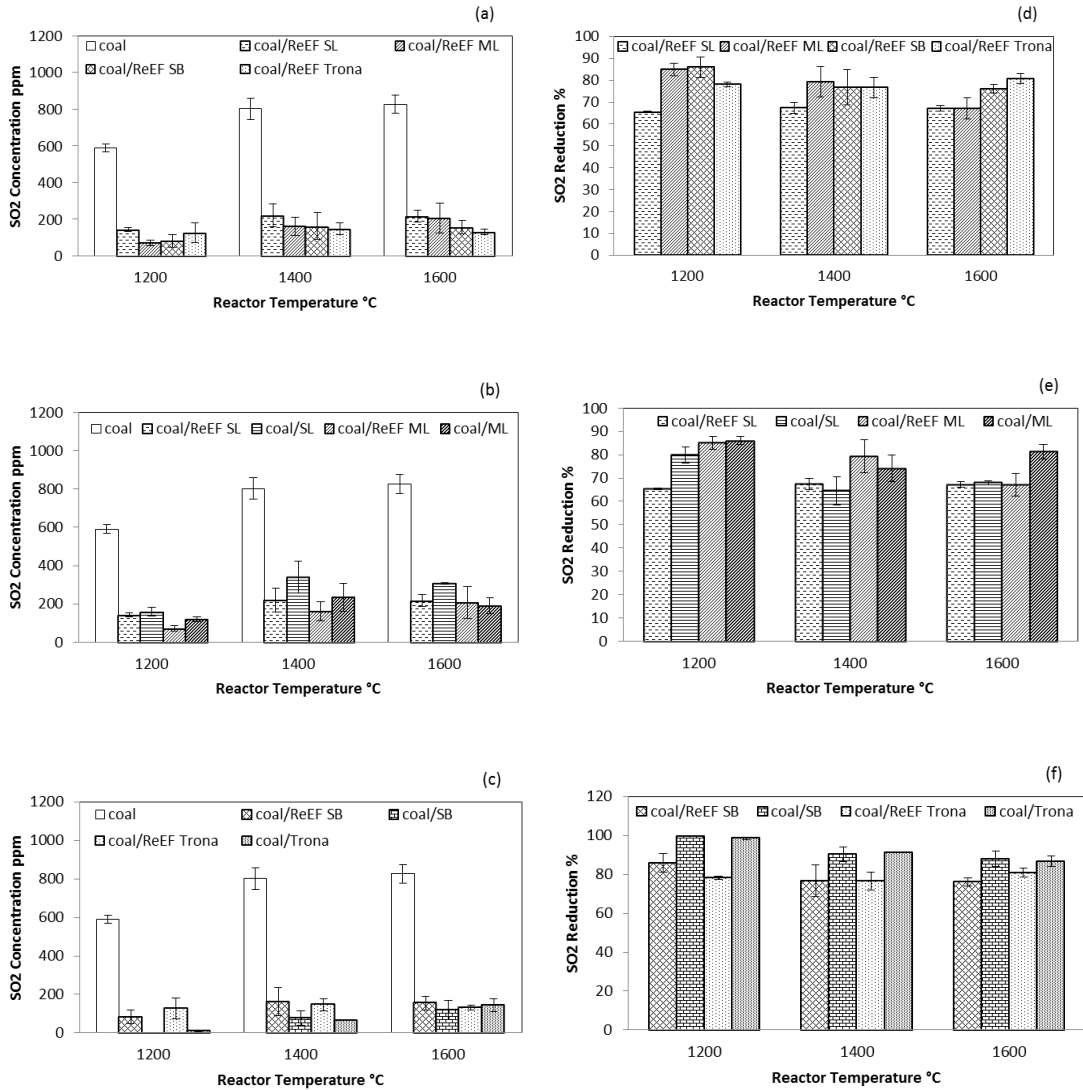


Figure 28. Sulfur dioxide reduction of co-firing ReEF and coal. The left column is SO<sub>2</sub> flue gas concentrations for different feedstock at temperatures, 1200, 1400, 1600°C: (a) coal and coal/ReEF mixtures; (b) coal and mixtures with Ca-based sorbent; (c) coal and mixtures with Na-based sorbent. The right column is the corresponding SO<sub>2</sub> reduction for different feedstock at temperatures, 1200, 1400, 1600°C: (d) coal/ReEF mixtures; (e) mixtures with Ca-based sorbent; (f) mixtures with Na-based sorbent.

Of particular interest to ReEF performance is variation in sorbent surface area. For example, Sorbocal lime is a type of calcium hydroxide which has higher surface area than Mississippi lime. From previous research, higher surface area has led to higher sulfur retention in

coal combustion<sup>139,140</sup>. However, we observe the opposite trend, such that ReEF with Mississippi lime has better SO<sub>2</sub> removal than sorbical lime under the same Ca/S conditions, especially at 1200 °C and 1400 °C (Figure 28 (b) and (e)). Similar to the combustion efficiency of these two fuels, this further confirmed that ReEF ML exhibited better combustion and emission-capture performance than ReEF SL. Shown in Figure 28 (b) at each temperature, both coal/ReEF SL and coal/ReEF ML result in less SO<sub>2</sub> flue gas than corresponding coal/SL and coal/ML. These results indicate that Ca-based sorbent embedded within ReEF capture SO<sub>2</sub> emission with better efficiency than direct utilization of Ca sorbents.

Overall superior sulfur capture of Na-based sorbents is consistent with previous studies have shown Na-based sorbents to have higher reactivity toward SO<sub>2</sub> compared to Ca-based sorbents in dry injection systems<sup>141</sup>. As shown in Figure 28 (c), coal combustion utilizing ReEF with Na-based sorbent emits very low SO<sub>2</sub> concentrations in the flue gas with only 100~150 ppm. Though the SO<sub>2</sub> concentration and reduction of both ReEF SB and ReEF Trona are nearly the same in Figure 28 (c and f), the (Na/2)/S ratio of ReEF SB is 2, which is significantly smaller than that of ReEF Trona which is 2.8. Therefore, on a per-sodium-basis, ReEF SB has higher SO<sub>2</sub> adsorption capacity. While the Na-sorbent/coal mixture performs better than ReEF at 1200 °C (Figure 28 ©), ReEF with Na-based sorbent provides comparable sulfur capture performance at 1400-1600 °C.

#### **3.2.4.4 NO Reduction**

Nitrogen element in the fuels in the process of combustion would generate NO<sub>x</sub> such as NO, NO<sub>2</sub>, N<sub>2</sub>O and NH<sub>3</sub>. Nevertheless, NO<sub>2</sub>, N<sub>2</sub>O and NH<sub>3</sub> emission were in a low concentration in our study, only 0.1~1 ppm which could be neglected. The NO during this process was the major NO<sub>x</sub> emission which reached about 50~300 ppm. Generally, the NO<sub>x</sub> emission can be generated from oxidation of nitrogen in the fuel (fuel-bound NO), oxidation of molecular nitrogen from air (thermal NO), and reaction between fuel radicals and atmosphere nitrogen (prompt NO). Prompt



NO can be produced directly in the combustion flame zone where the molecular nitrogen reacts with hydrocarbon fragments from fuel. Although we couldn't quantify how much NO emission produce from prompt NO pathway, it is reported that prompt NO is usually neglected compared to thermal NO<sup>142</sup>. Figure 29 (a) shows the concentration of NO emission from coal/ReEF mixtures. We observed a decrease in the NO concentration in all the coal/ReEF mixtures compared with coal at all temperatures. This is due to ReEF containing lower nitrogen than coal, which leads to a lower NO emission from the fuel. Thermal NO is generated by the reaction between atmosphere oxygen and nitrogen above 1540 °C, and more is produced at even higher temperature. The amount of NO emission depends on the access of oxygen concentration. As reported in other studies, combustion of coal in air produced 20% more NO<sub>x</sub> than in a nitrogen free atmosphere<sup>45</sup>. Although the highest temperature we used in our experiments was 1600 °C, combustion is an extreme exothermic reaction which causes the boost in temperature over 1600 °C in flame zone and post flame zone.

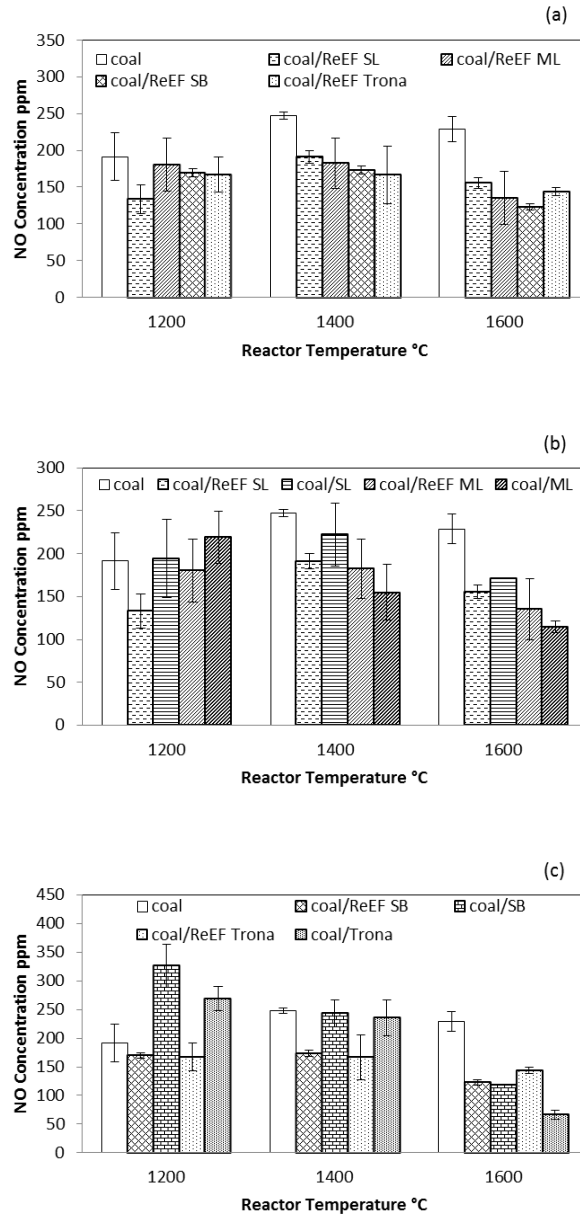


Figure 29. NO reduction in co-firing ReEF and coal. (a) coal and coal/ReEF mixtures; (b) coal and mixtures with Ca-based sorbent; (c) coal and mixtures with Na-based sorbent.

In this study, however, Figure 29 (a) shows a slight decrease of NO concentration for coal and coal/ReEF blends from 1400 °C to 1600°C, which is contradicted to thermal NO emission

tendency. One possible cause could be attributed to the mechanism that NO can react with char to form molecular nitrogen<sup>93</sup>.



Another cause for lower NO emission is due to the Ca-based and Na-based sorbents. In general, coal/ReEF mixtures emitted 50~100 ppm less NO than pure coal (Figure 29 (a)). This indicates the sorbents in ReEF might have the potential to capture NO flue gas. Calcium oxide has been studied as a catalyst on the reaction (4) and (5). By addition of CaO, the emission of NO and CO will be reduced<sup>47</sup>. Sodium bicarbonate can be a sorbent for both SO<sub>2</sub> and NO removal<sup>143</sup>.

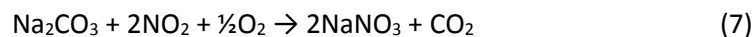


Figure 29 (b) shows principally coal/ReEF SL and coal/ReEF ML have less NO emission than pure sorbent mixtures by up to 60 ppm. At 1400 °C and 1600 °C coal/ReEF ML emitted less NO than coal/ReEF SL. This manifests ReEF ML is better than ReEF SL on both economy and efficiency aspects. Figure 29(c) shows at 1200 °C and 1400 °C coal/ReEF SB and coal/ReEF Trona have much less NO emission than coal/sorbent mixtures. At 1600 °C coal/ReEF SB emitted a slightly less NO than coal/ReEF Trona. Although the difference is rather small, 20 ppm, regarding ReEF SB has smaller (Na/2)/S ratio, NO reduction capacity of ReEF SB is better than ReEF Trona. However, the coal/sorbent mixtures emission are even higher than that of coal. This might be due to the feeding rate for coal/sorbent mixture was 0.6 g/min compared to 0.5 g/min of coal.

### 3.2.5 Conclusion

An experimental study of ReEngineered feedstock for coal combustion emission control is presented. The results show co-feed of ReEF in coal combustion greatly increases the sulfur retention and decreases NO emission.

(1) The carbon conversion is enhanced when co-firing ReEF and coal proves that ReEF is a promising feedstock for coal combustion. For all four ReEF materials, carbon conversion at 1400°C is the highest to be the optimal temperature for combustion. On account of Mississippi lime as a nature product, it's recommended to use ReEF ML instead of ReEF SL at a much cheaper price for similar performance.

(2) Calculation results show significant reduction of SO<sub>2</sub> emission in combustion flue gas to at least 70% by mixed with ReEF. The advantage of ReEF with Na-based sorbent on SO<sub>2</sub> reduction is a bit more evident than ReEF with Ca-based sorbent. For the same Ca/S ratio, SO<sub>2</sub> reduction by ReEF ML is higher than ReEF SL. This confirms ReEF ML behaves better than ReEF SL as a coal combustion adsorbent. Since (Na/2)/S ratio of ReEF SB is smaller than that of ReEF Trona to have higher SO<sub>2</sub> adsorption capacity, it's suggested to select ReEF SB for better desulfurization effect.

(3) In general, coal/ReEF mixtures emit less NO than pure coal consistent with less nitrogen content in ReEF. The overall tendency of NO emission for all fuel blends are decreasing as the temperature increases. This possibly due to the mechanism of NO reacting with char or the sorbents in ReEF.

### 3.3 Drop tube Reactor

The ReEngineered Feedstock containing Sorbocal lime (high surface area calcium hydroxide) was selected to be comprehensive characterized to reveal the morphology and composition. The sulfation reactions of ReEF were tested in a drop tube reactor with various

reaction conditions. The results shows combusting the ReEF in the low oxygen environment would lead a high conversion of calcium hydroxide to calcium sulfate in a long time reaction. Moreover, the sulfation of the calcium hydroxide in ReEF is delayed by the RDF combustion compared with that of pure calcium hydroxide.

### 3.3.1 Materials

Table 18 shows the detailed elemental analysis on the ReEF containing Sorbacal lime. The particle size distribution of ReEF was determined by sieving the pulverized ReEF through a series of U.S. Standard sieves. The ReEF was separated upon the particle size smaller than 25  $\mu\text{m}$ , 25-53  $\mu\text{m}$ , 53-212  $\mu\text{m}$ , 212-500  $\mu\text{m}$ , 500-1000  $\mu\text{m}$  and larger than 1000  $\mu\text{m}$ . A carbon content analysis as a function of particle size was determined by the Galbraith Laboratories Inc. Since the calcium hydroxide content varies from different particle sizes, an EDTA titration was used to determine the calcium content. The particle size distribution of pulverized ReEF is shown in Figure 30. Only a small portion of particles has larger size ( $>1000 \mu\text{m}$ ) or smaller sizes ( $< 53 \mu\text{m}$ ). About 58 wt% of the particles have a size range of 53-500  $\mu\text{m}$ . The arithmetic mean diameter of pulverized ReEF particles is about 428  $\mu\text{m}$ , which is larger than the mean diameter of pulverized coal particles (310  $\mu\text{m}$ ). Figure 31 illustrates the content of calcium hydroxide and carbon of the different particle sizes. We can observe a decrease in content of calcium hydroxide from small particles to large particles. However, the carbon content is in a contrary trend that the large particles contains highest carbon, which indicates more fibers and plastics existing in the large particles. Although the sorbent was well mixed with refuse-derived fuel in the material preparation process, when the pellets were pulverized, the sorbent may be detached from the surface of the RDF due to the strong mechanical force from pulverizing.

Table 18: Elemental analysis of ReEngineered Feedstock containing Sorbacal lime

<b>Proximate Analysis (wt %)</b>		<b>Other Elements (wt %)</b>	
Moisture	1.24	Calcium	22.9
Volatile Matter	59.61	Silicon	1.05
Fixed Carbon	5.33	Chlorine	0.69
Ash	33.76	Aluminum	0.66
<b>Ultimate Analysis (wt%)</b>		Sodium	0.41
Carbon	33.76	Magnesium	0.25
Hydrogen	5.08	Iron	0.18
Oxygen	26.11	Potassium	0.04
Nitrogen	0.06	<b>Heat of Combustion (BTU/lb )</b>	5787
Sulfur	0.04		

The surface area of pure calcium hydroxide (Sorbacal® SP) and the pulverized ReEF particles were measured by nitrogen adsorption using Autosorb-1 from Quantachrome Instruments. The degassing of the sample was in a temperature of 99 °C and complete degas was achieved when the pressure difference was lower than 25 mtol. The nitrogen was used as absorbed gas in a temperature of 77 K. The surface area was calculated using BET equation and total pore volume was measured at the relative pressure of 0.95. Table 19 shows the results from nitrogen adsorption for calcium hydroxide and ReEF particles. The calcium hydroxide is a porous material with high surface area and large pore volume due to the special manufacturing. However, the ReEF particles has lower surface area and pore volume, which indicates the ReEF is a non-porous material. This is due to large portion of non-porous fibers and plastics added in the ReEF.

Table 19: Surface area of ReEF and calcium hydroxide

Sample	Surface area (m <sup>2</sup> /g)	Pore volume (*10 <sup>-3</sup> cm <sup>3</sup> /g)
Calcium hydroxide	34.8	190
ReEF (<25 μm)	2.5	7.5
ReEF (25-53 μm)	4.1	10.7
ReEF (53-212 μm)	2.4	7.2

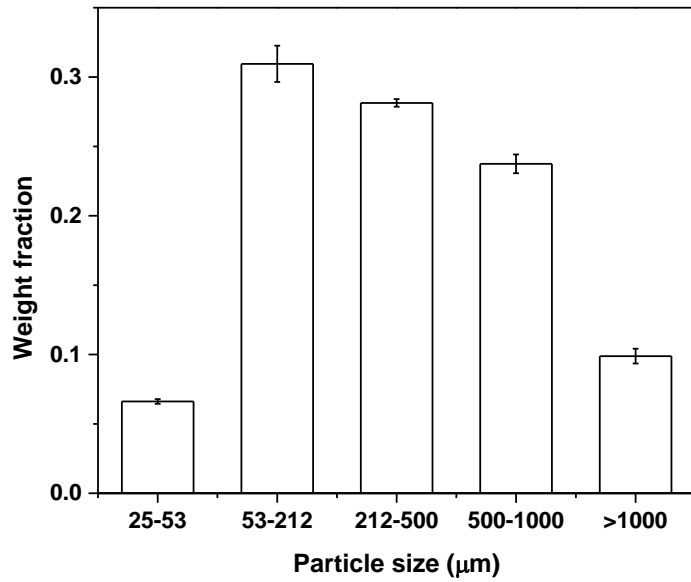


Figure 30. Particle size distribution of ReEF

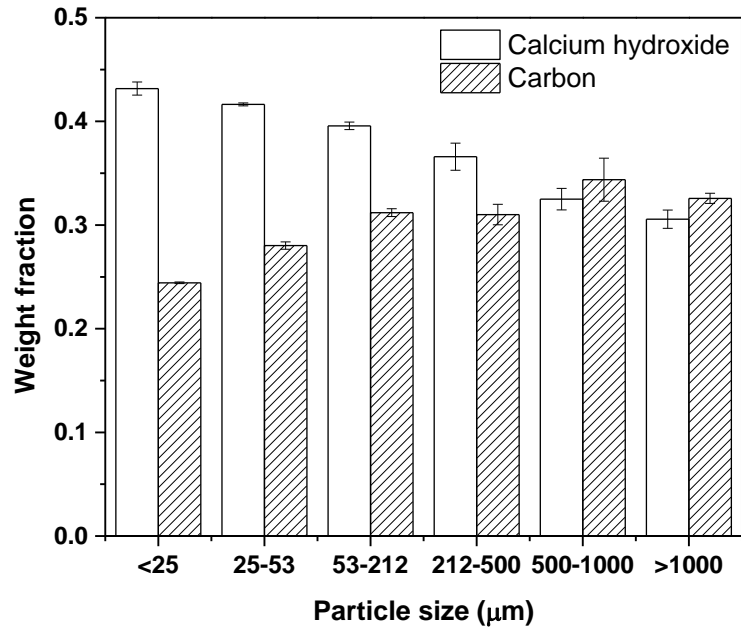


Figure 31. Calcium hydroxide and carbon content in ReEF at different particle sizes

Figure 32 shows the images of ReEF. After the manufacturing process, the ReEF is pelletized. The pulverized ReEF is sieved into different particle sizes as shown in Figure 8 b, c, and d. The microscopic images of ReEF at different particle sizes are shown in the Figure 33. We defined the circularity as the equation 8. If the circularity is close to 1, the shape of the particle is close to a perfect circle. The circularities of particles in (a), (b) and (c) in

$$\text{Circularity} = \frac{4 \pi * \text{Area}}{\text{Perimeter}^2} \quad (8)$$

Figure 33 are 0.63, 0.58 and 0.41, respectively, which indicates the shape of smaller particles is more toward to a circle. The long strings of fibers and plastics started to be observed in 53-212  $\mu\text{m}$  particles. For even larger particles, they may be formed by the twining of fibers and plastics as shown in (d) in Figure 33. We also notice that the ReEF particles have a property of flaky shape, which is different from the spherical coal particles. This may cause the difficulties when fluidizing the ReEF materials.

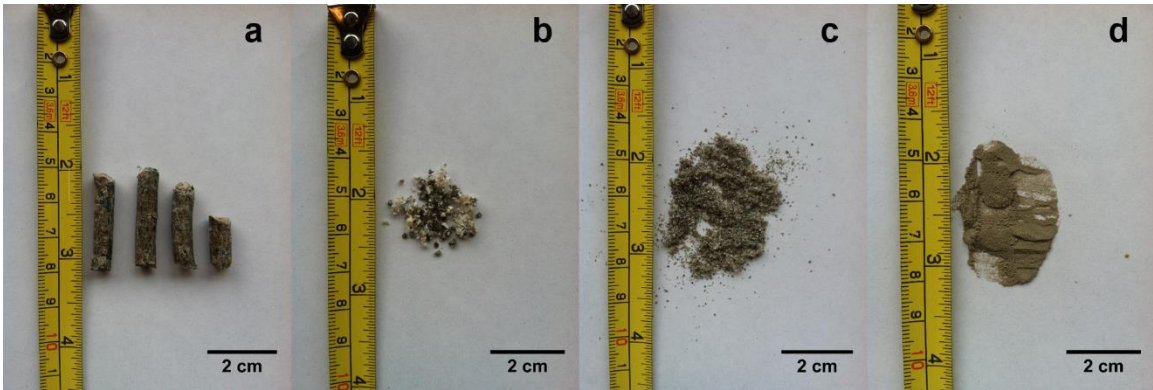


Figure 32. Images of ReEF. (a) ReEF pellet, (b) Particle size larger than 1 mm, (c) Particle size between 212  $\mu\text{m}$  and 500  $\mu\text{m}$ , (d) Particle size between 25  $\mu\text{m}$  and 53  $\mu\text{m}$



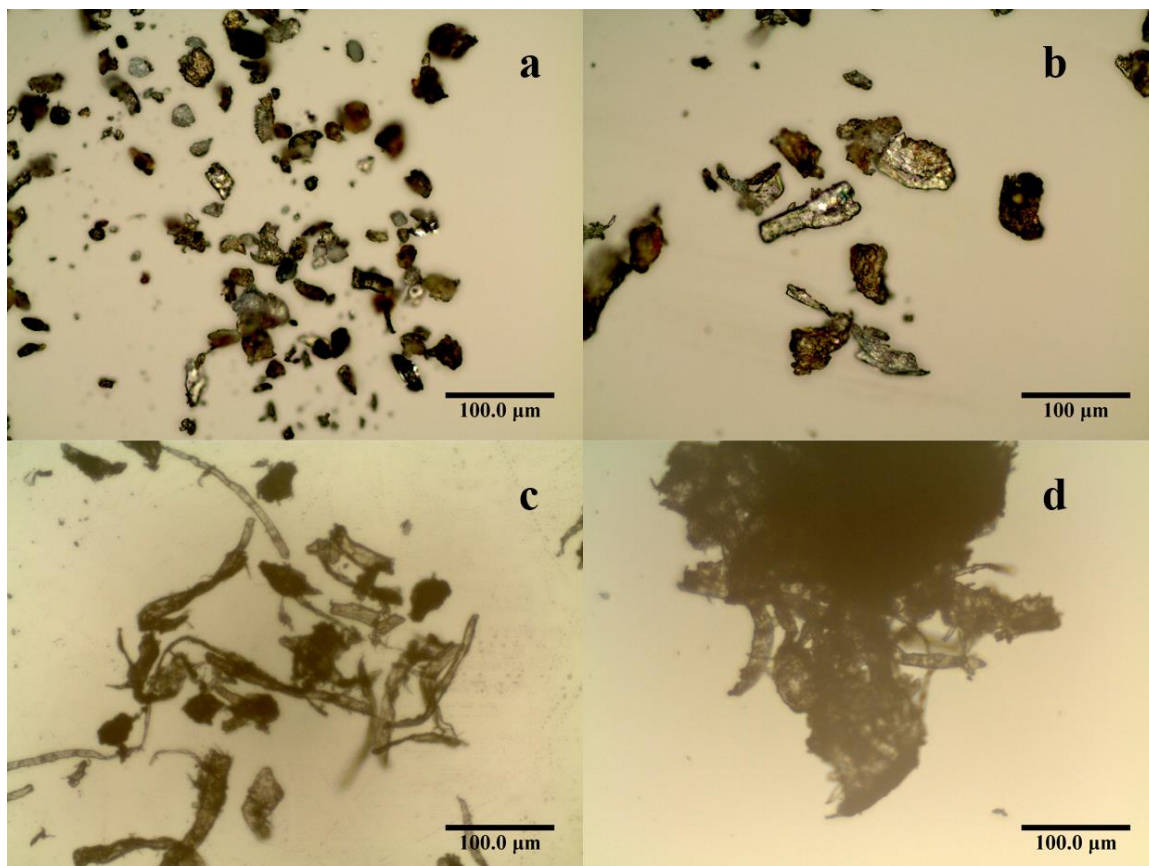


Figure 33. Microscopic images of ReEF. (a) less than 25  $\mu\text{m}$ , (b) 25-53  $\mu\text{m}$ , (c) 53-212  $\mu\text{m}$ , (d) 212-500  $\mu\text{m}$

To further study the sorbent distribution in the ReEF particles, SEM images and elemental mapping of ReEF particles were taken on FEI SEM Magellan 400. An accelerating voltage of 3 kv, 7 kv and a current of 50 pA, 0.2 nA were applied to the SEM images and EDX mapping, respectively. The ashes collected from the ReEF combustion and desulfurization were analyzed by X-ray diffraction (a Philips powder diffractometer, model X'Pert system). The XRD pattern was obtained under an accelerating voltage of 45 kv and a current of 40 mA.

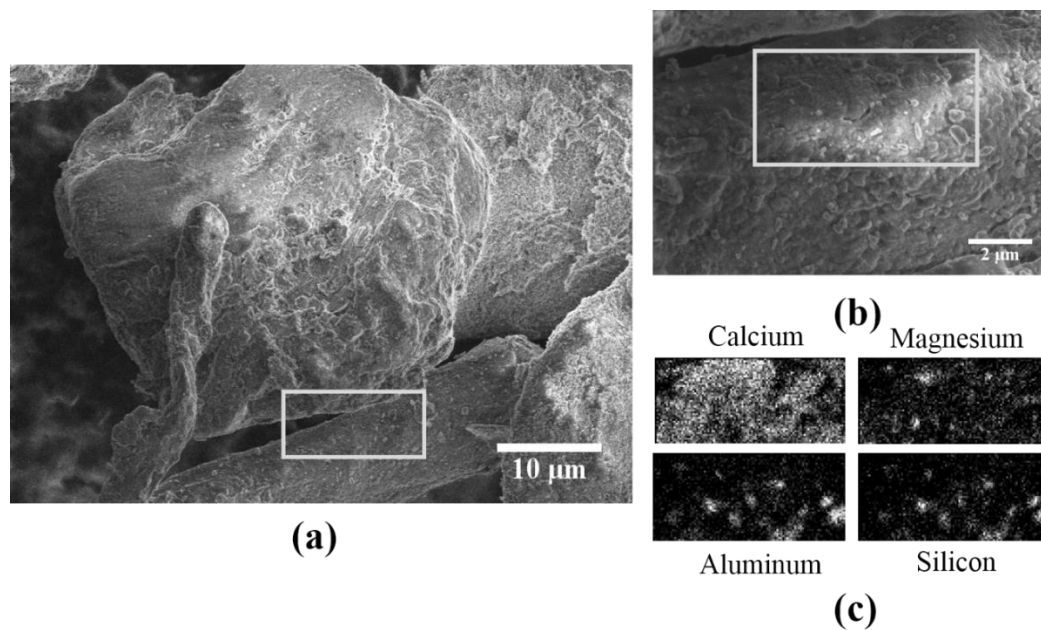


Figure 34. SEM-EDX of Reengineered feedstock. a) SEM image of ReEF, b) Enlarged SEM image of area in white box in (a), c) EDX mapping of white box in (b), d) Spectrum of EDX of white box in (b)

Figure 34 (a) shows the SEM image of ReEF particles having a size between 25 μm and 53 μm. We noticed that there are small white particles randomly dispersed on the rough surface as shown in Figure 34 (b). An energy-dispersive X-ray spectroscopy was used to analyze the white

rectangular area in Figure 34 (b). The results of elemental mapping on the surface are shown in Figure 34 (c) and (d). The major elements on the surface are carbon, oxygen and calcium, which are from the main components of ReEF. The signal of calcium element was detected almost everywhere on the surface. This indicates the distribution of calcium hydroxide on the surface is random. Other than calcium, we also detected the sodium, magnesium, aluminum, silicon and chlorine on the surface, which are from the waste stream. The elemental maps of aluminum and silicon are overlapped with each other, which indicates the existence of aluminum silicates. In terms of particle size of dispersed calcium hydroxide, it could vary from several microns to submicron.

### **3.3.2 Experimental Apparatus and Procedure**

#### **3.3.2.1 Drop tube reactor**

Figure 35 shows the reactor system for studying the ReEF particles combustion and desulfurization reactions. The composition and flow rate of gas stream can be varied and controlled by the thermal mass flow controller from Brooks Instruments. In each run, 10mg of ReEF was loaded into the feeding rotary valve. A 1 L/min gas flow with a concentration of 1400ppm SO<sub>2</sub> flowed through the reactor system before the ReEF was injected into the reactor. At the time zero, by turning the valve knob, the ReEF particles dropped into the hot zone and stayed on a quartz frit. The fibers and plastics from the ReEF were combusted, leaving the sorbent to react with SO<sub>2</sub>. The reactor consisted of a 1 inch OD quartz tube on the top and was reduced to ¼ inch quartz tube after the reaction to minimize the axial mixing. The gas stream was analyzed by an online Bruker Vertex 70 FTIR with a Harrick temperature controlled gas cell (10cm pathlength and 17ml cell volume).

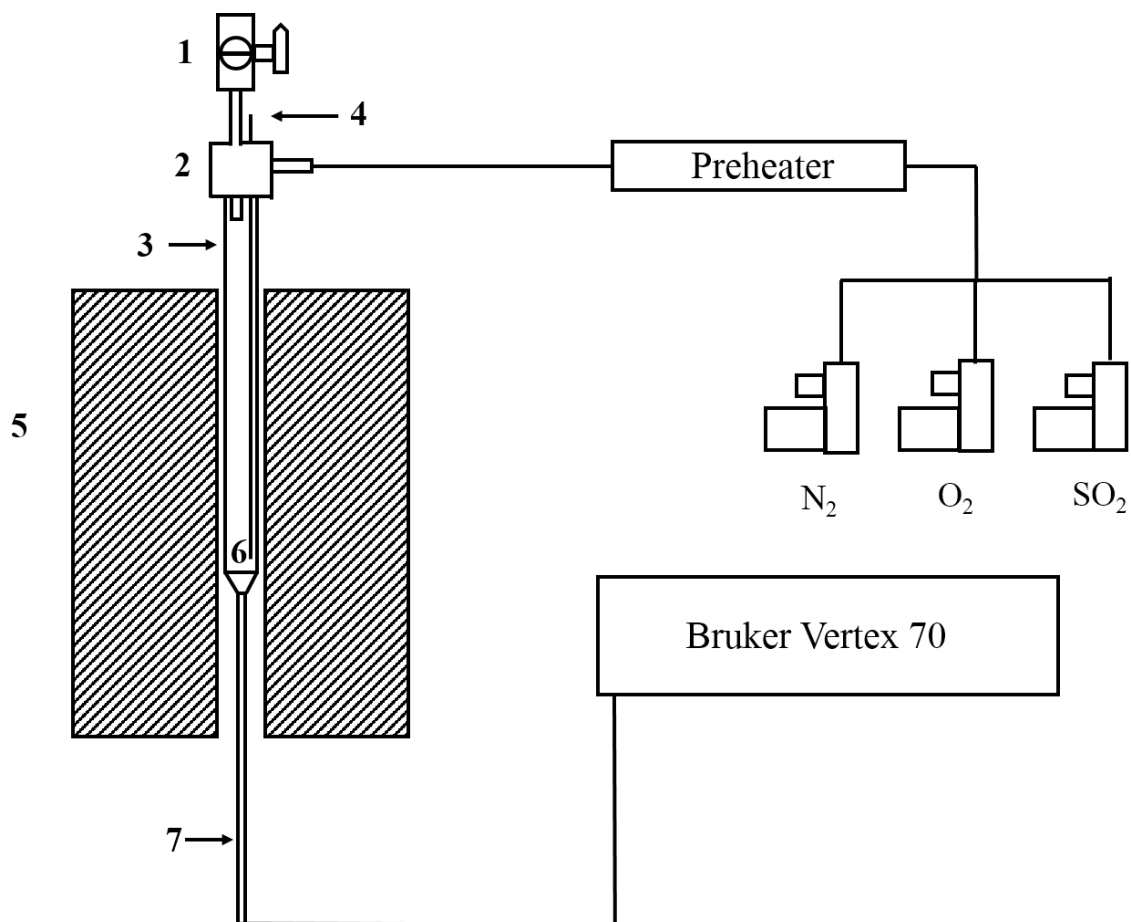


Figure 35. Drop tube sulfation reactor setup. 1) Feeding rotary valve 2) Swagelok tee 3) 1 inch quartz tube 4) Thermocouple 5) ATS furnace 6) Quartz frit 7) ¼ inch quartz tube

### **3.3.2.2 Calcination Reactor**

A horizontal reactor system was set for studying the calcination and combustion of ReEF. The schematic diagram is shown in the Figure 36. The reactor consists of a ½ inch diameter quartz tube with Swagelok ultr-torr fitting on the both ends. A quartz boat containing the sample was attached to a ¼ inch quartz tube. Before the calcination, the temperature was set at 800 °C and maintained at a constant. A certain concentration of gas (containing the different ratio of oxygen to nitrogen) flew through the reactor. The sample was directly inserted into the center of the

furnace for calcination and then collected after a certain time in the vial attached to the reactor tube. The advantage of this setup is to allow us to control the calcination time. Sorbent can be transferred into the collecting vial immediately after it is taken out from the hot furnace. Fast cooling minimizes potential sorbent sintering compared to the slowing cooling in the sulfation reactor. The collected sample was purged by nitrogen and sealed for further analysis.

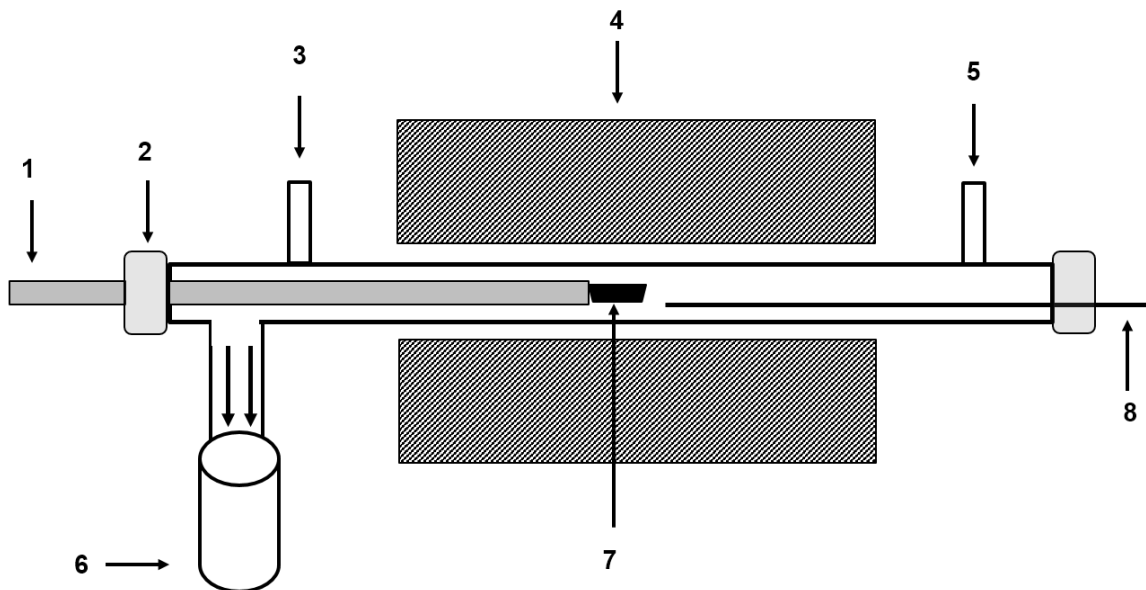


Figure 36. Calcination reactor setup. 1) quartz rod, 2) Swagelok ultr-torr fitting, 3) gas inlet, 4) furnace, 5) gas outlet, 6) sample collection vial, 7) quartz boat, 8) Thermocouple

### 3.3.3 Results and Discussions

#### 3.3.3.1 Sulfation of ReEF

The gas flow of the reaction consisted of 1400 ppm sulfur dioxide, (5 %-30 %) of oxygen and nitrogen as balance. When the ReEF particles dropped into the hot reaction zone. A series of reactions would happen as shown in Figure 37. The fibers and plastics in the ReEF is dried at first. As the heat transfers into particles, the solid fibers and plastics begin to decompose, releasing volatiles. The volatiles flow out of the surface and react with the oxygen to form carbon dioxide and water. As the devolatilization proceeds, the particle shrinks and finally leaves the char and

ash remain. The char then would further be combusted under the oxygen environment and having the ash left. On the other side, the calcination of calcium hydroxide takes place first. As calcium hydroxide decomposes, a fresh CaO layer are formed surrounding the unreacted calcium hydroxide. It is reported that the fresh CaO layer is highly porous and active to react with sulfur dioxide<sup>144-146</sup>. The outer CaO layer undergoes sintering and sulfation simultaneously as the inner calcium hydroxide continues decomposing. A CaSO<sub>4</sub> layer forms when CaO react with O<sub>2</sub> and SO<sub>2</sub>. Since the molar density of CaSO<sub>4</sub> is larger than that of CaO, the CaSO<sub>4</sub> layer is considered to be non-porous, which generates strong transport resistance for the SO<sub>2</sub> and O<sub>2</sub> flowing in to contact with CaO or H<sub>2</sub>O from calcination of calcium hydroxide flowing out. At one point, the sulfation reaction would become extremely slow due to the gas and Ca<sup>2+</sup> and O<sup>2-</sup> ion transport limitation<sup>147,148</sup>. The non-porous CaSO<sub>4</sub> layer can also stop the water transporting to outside, which causes an increase in water concentration inside of the particles. The calcination would stop when the water reaches the equilibrium concentration. The structure of the sorbent particle after a certain time of sulfation reaction may contains the CaSO<sub>4</sub> layer, unreacted CaO layer and incomplete calcined calcium hydroxide.

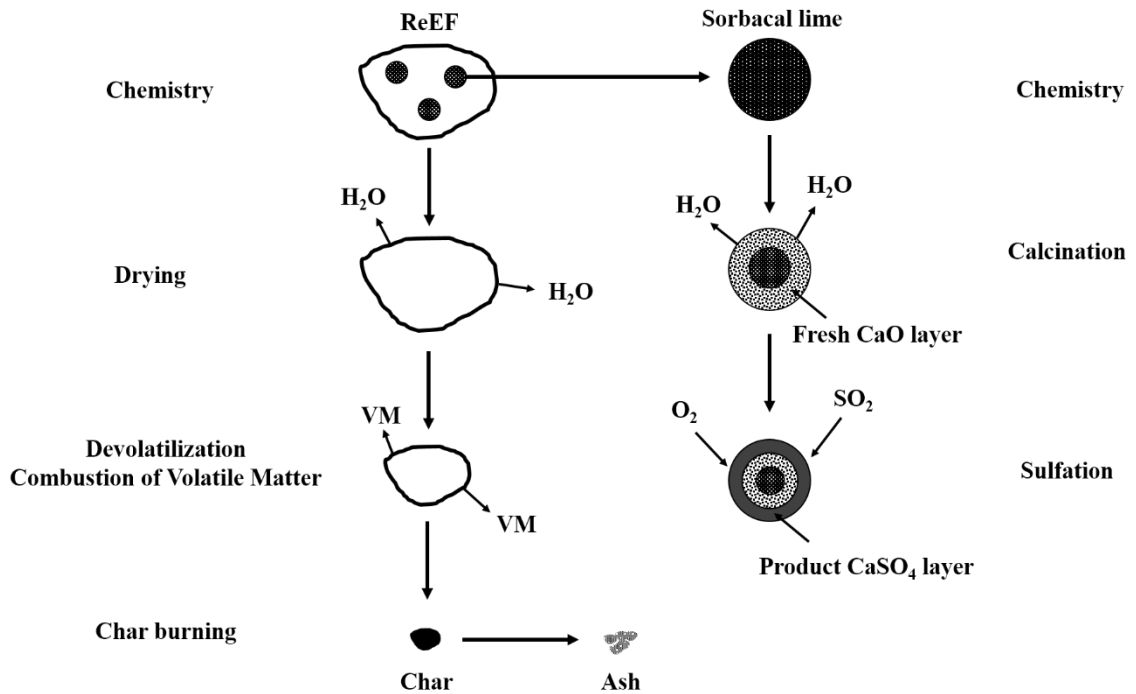


Figure 37. Reactions of ReEF dropping into the furnace.

Figure 38 shows the typical sulfur dioxide concentration measured from FTIR. The concentration of SO<sub>2</sub> keeps at a level when there is no ReEF dropping into the reactor. At the time zero, the ReEF dropped into the reactor and sorbent started to adsorb SO<sub>2</sub>. The concentration of SO<sub>2</sub> decreased to a minimum value and went back to an asymptotic value. The reaction rate was expressed as the conversion of calcium hydroxide to calcium sulfate and calculated by the equation 9. By integrating the equation 9, we can obtain the conversion of the sorbent as a function of time.

$$\frac{dX}{dt} = \frac{PV(Y_{SO_2,in} - Y_{SO_2,out})/RT}{W \cdot a/M(Ca(OH)_2)} \quad (9)$$

X: Conversion of calcium hydroxide to calcium sulfate

P: Pressure of the reactor

V: Gas flow rate

Y: Concentration of sulfur dioxide

R: Gas constant

T: Reaction temperature

W: Weight of the ReEF sample

a: Fraction of sorbent in the ReEF

M: Molecular weight of calcium hydroxide

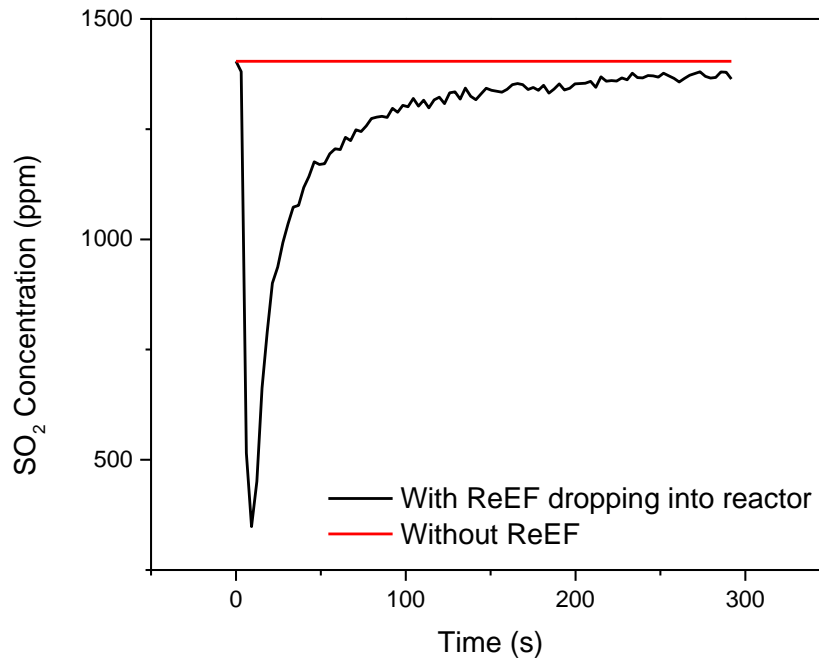


Figure 38. The sulfur dioxide concentration profile for a typical run

The sulfation reactions of ReEF were tested under three temperatures (800 °C, 900 °C and 1000 °C) with varies oxygen concentration (5%, 10%, 20% and 30%). 10 mg of ReEF sample at different particle sizes were injected into the reactor. The same amount of pure calcium hydroxide was also tested under the same reaction conditions as the comparison. Figure 39 shows the conversion of calcium hydroxide to calcium sulfate as the function of time for 25-53  $\mu\text{m}$  ReEF particles at 900 °C under various oxygen concentration. The pure sorbent are run at the same



reaction conditions as control experiments. Within the first 50 seconds, the conversion of both reactants are similar. However, the divergence on the conversion happens after a long time reaction. A lower oxygen concentration (Figure 39 (a)), the difference on the long time sorbent conversion is relative small. As the oxygen concentration increases, the different on the conversion is more obvious (Figure 39 (d)). Since the same amount of calcium hydroxide were put into the system for all the tests, for the ReEF, the combustion of fibers and plastics became the factor which affects the sorbent on sulfur take. With more oxygen in the system, the fibers and plastics achieved more complete combustion, which led to more carbon dioxide and water generation. Both of the gases accelerate the sintering rate of the nascent calcium oxide, which results in a lower conversion of sorbent at higher oxygen environment. Meanwhile, the combustion is an extreme exothermal reaction. It may cause a temperature increase which also accelerates the sorbent sintering. We notice the difference on the sorbent conversion happens after a long time run. It is believed that a product layer has already formed and the reaction is controlled under product layer diffusion. Evidences showed the diffusion in the product layer is a solid state diffusion by the  $\text{Ca}^{2+}$  and  $\text{O}^{2-}$  diffusing toward the particle surface<sup>147,148</sup>. In the ReEF, it contains the other metal oxides from the waste. They could hinder the  $\text{Ca}^{2+}$  and  $\text{O}^{2-}$  diffusing out to react with  $\text{SO}_2$ , which leads to a lower sorbent conversion.

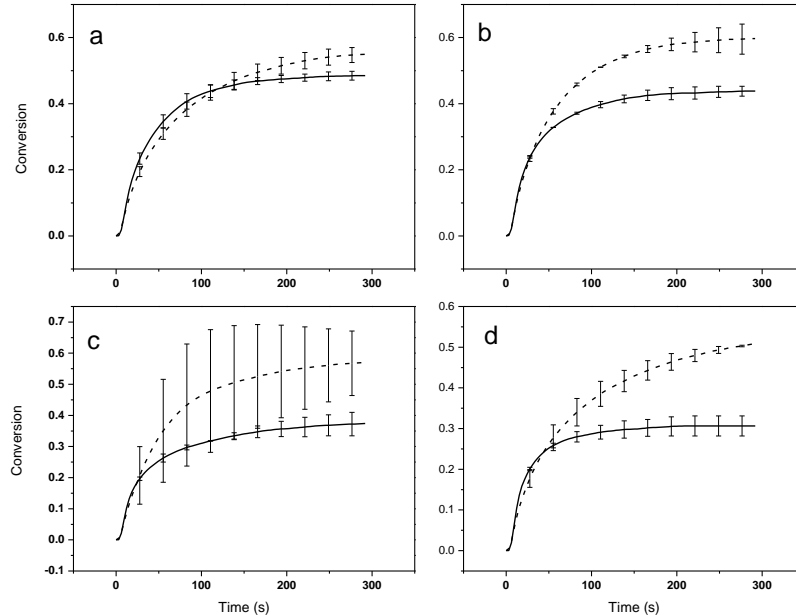


Figure 39. Conversion of sorbent with reaction time at 900 °C. Pure sorbent (dash line) and sorbent in ReEF (solid line) under 5% O<sub>2</sub> (a), 10% O<sub>2</sub> (b), 20% O<sub>2</sub> (c) and 30% O<sub>2</sub> (d).

Figure 40 shows the conversion of calcium hydroxide to calcium sulfate after five minutes run. The effect of oxygen concentration on the sulfation of pure calcium hydroxide isn't obvious as shown in Figure 40 (d). The conversion of pure calcium hydroxide to calcium sulfate are similar at each temperature even in various oxygen concentration. However, we observed a decrease on the sorbent conversion as the oxygen concentration increases in the ReEF particles, especially on the particles having a size range from 25  $\mu\text{m}$  to 212  $\mu\text{m}$  (Figure 40 (a) and (b)). The temperature effect on the sorbent conversion in the ReEF is different from that in the pure calcium hydroxide. In the ReEF particles, the conversion is always the lowest at 900 °C while this trend is not observed in the pure calcium hydroxide (Figure 40 (a), (b) and (c)). This is probably due to the interacting between calcium oxide and impurities from the ReEF. For the small particles (25-212  $\mu\text{m}$ ), the conversion of sorbent are similar under same reaction conditions (Figure 40 (a) and (b)). However,

large particles (212-500  $\mu\text{m}$ ) have more sorbent conversion at higher oxygen concentration than that of small particles (Figure 40 (c)).

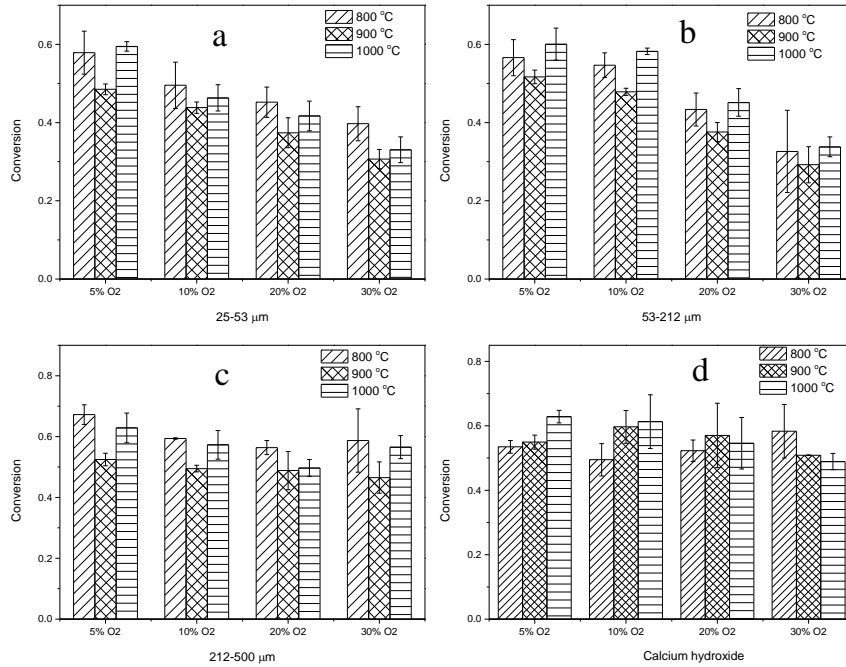


Figure 40. Conversion of Calcium hydroxide in ReEF after 5min run

Figure 41 presents the normalized reaction rate of conversion of pure calcium hydroxide and calcium hydroxide in ReEF. We observed a time delay ( $\Delta t$ ) on the maximum reaction rate of sulfation. For the pure calcium hydroxide, the time of maximum sulfation rate always happened earlier than that of calcium hydroxide in ReEF, which indicates that the combustion of fibers and plastics in ReEF can delay or slow the sorbent sulfation reaction. The time delay ( $\Delta t$ ) of the maximum reaction rate in various reaction conditions are plotted in the Figure 41. Since the sampling rate from the FTIR analysis was 3 second per spectrum, in most cases, there were at most three seconds time delay on the maximum sulfation rate. For the large ReEF particles (212-

500  $\mu\text{m}$ ), this time delay can reach about six seconds (Figure 42 (a)). One of the possible reason to explain this phenomena is that a film or cloud of gas and volatiles from combustion of fibers/plastics is generated around the sorbent particles. The film/cloud of gas will prevent the sulfur dioxide from contacting with the sorbent. The sulfation will resume after the gas film/cloud moving with the external flow. The delay on the sulfation reaction can be vital in the co-firing coal with ReEF on the sulfur dioxide emission control. If injecting the pure sorbents into coal boiler, due to the extreme high temperature, it is thermodynamically unfavorable for the sulfation reaction and products. However, by applying the time delay in ReEF combustion, it will prevent the sorbents form early sulfation. Instead, the sulfation reaction would happen when sorbents travel into a lower temperature zone where thermodynamically more favorable for reaction and products. In this case, it will potentially increase the efficiency of capturing the  $\text{SO}_2$ . Also, this provides a promising future for co-firing coal and ReEF without additional  $\text{SO}_2$  removing technologies.

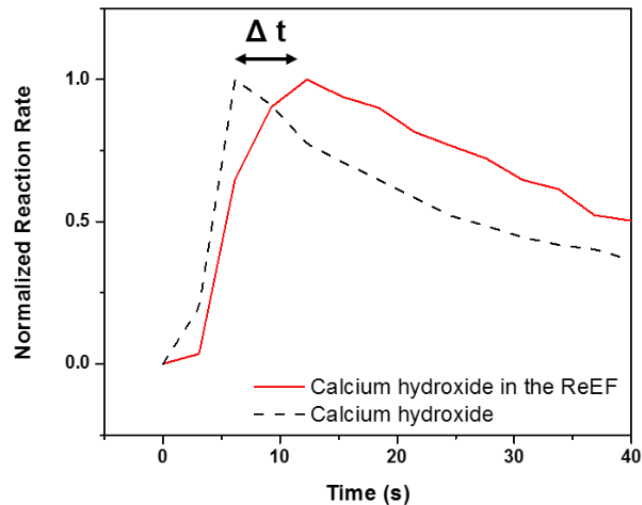


Figure 41. Maximum reaction rate of sorbent sulfation in ReEF is delayed by biomass combustion

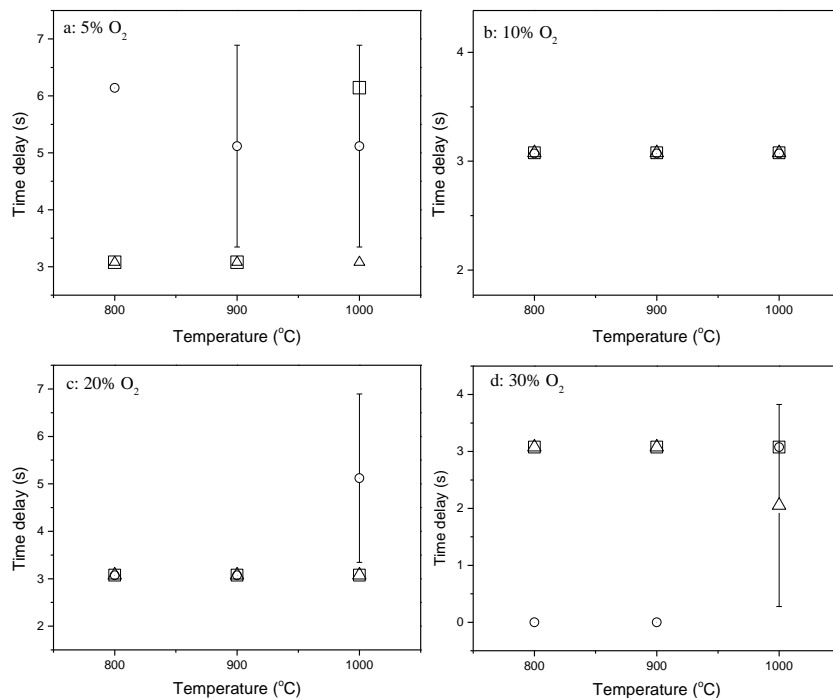


Figure 42. Time delay on the maximum reaction rate. (□ 25-53 μm, ○ 53-212 μm, Δ 212-500 μm)

### 3.3.3.2 Calcination/Combustion of ReEF

In the previous research, we conclude that the sorbent conversion in the sulfation of ReEF is lower than that of pure sorbent at a long time run. This indicates the combustion of fibers and plastics in the ReEF would affect the sorbent sulfation performance. To further study the effects of fiber/plastic combustion on the sorbent calcination and sulfation, the ReEF combustion/calcination and sulfation are studied separately. The calcination reactor in Figure 36 was applied for simultaneously combustion and calcination of ReEF. The sample was inserted into the hot furnace in the present of oxygen flow. The fiber and plastics are combusted meanwhile the sorbent thermally decomposed under high temperature. The calcined ReEF, mainly calcined sorbent, are subjected to the sulfation reactor to test the performance on desulfurization.

10 mg of ReEF and pure calcium hydroxide were inserted into the calcination furnace at 800 °C. The gas flow was set at 2 L/min with an oxygen concentration of 21%. Calcination with various times were tested. The collected samples were analyzed by XRD and SEM to characterize their physical structures. Figure 43 presents the XRD patterns of combustion/calcination of ReEF (Figure 43 (c) and (d)). As the comparison, the XRD pattern of calcined pure calcium hydroxide are also shown (Figure 43 (a) and (b)). The pure calcium hydroxide was calcined for 30s and we still can observe the peaks from calcium hydroxide, which is labeled as (2) in Figure 43-(a). If the time of calcination extends to 60s, no peaks from calcium hydroxide is detected as shown in Figure 43-(b). This indicates that after 60s calcination, the pure calcium hydroxide sample is completely decomposed to calcium oxide. However, when 10mg ReEF were subjected to the same condition (60s calcination), the peaks from calcium hydroxide are still observed in the calcined sample as shown in Figure 43-(c). This indicates that the calcination of sorbent in the ReEF takes longer than that of pure sorbent. In other words, the combustion of fibers/plastics can affect the rate of the sorbent calcination in the ReEF compared to the pure sorbent. The reaction rate of calcination depends on the difference between equilibrium dissociation pressure and partial pressure of water above the surface. During ReEF combustion and calcination, water partial pressure increases due to fiber/plastic combustion, which slows the rate of sorbent calcination. The XRD pattern of ReEF subjected to 2min calcination are shown in Figure 43-(d). Fully calcination is achieved and only calcium oxide is detected. Thus, to obtain the complete calcined sorbent, the calcination time of 2min was selected for the following sulfation study.

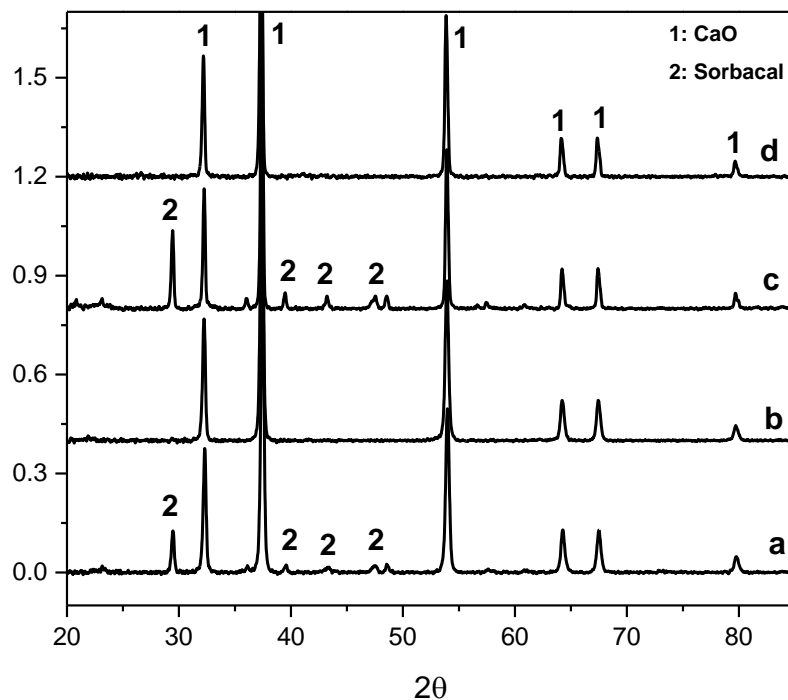


Figure 43. XRD patterns of calcined sorbents from calcination reactor (21%O<sub>2</sub>). a) calcination of sorbacal in 30s, b) calcination of sorbacal in 60s, c) calcination of ReEF in 60s, d) calcination of ReEF in 120s.

The concentration of oxygen was varied in calcination tests to study its effects on the ReEF sorbent calcination. SEM was used to characterize the surface morphology of calcined sorbents. Figure 44 shows the surface of sorbent after 2 min calcination in 21% and 100% of oxygen, respectively. In the lower oxygen concentration ((a) in Figure 44), we can observe the neck formation between the small grains, which indicates the sintering happening during the calcination. However, the extent of sintering is not as severe as that in 100% oxygen calcination, in which the surface almost consists of fused sorbent grains. In the Figure 44 (a), we can still observe pores on the surface. While in the Figure 44 (b), the pores are diminished and a solid

surface is observed. From the nitrogen adsorption isothermal analysis, the porosity of sorbent in 21% O<sub>2</sub> condition is 8.4% while a porosity of 3.6% is obtained for sorbent calcined in 100% O<sub>2</sub>. With these results, we prove that the sintering of the sorbent is enhanced by the intense combustion of fibers/plastics. The more oxygen in the calcination/combustion, the more sintered calcined sorbent we would obtain.

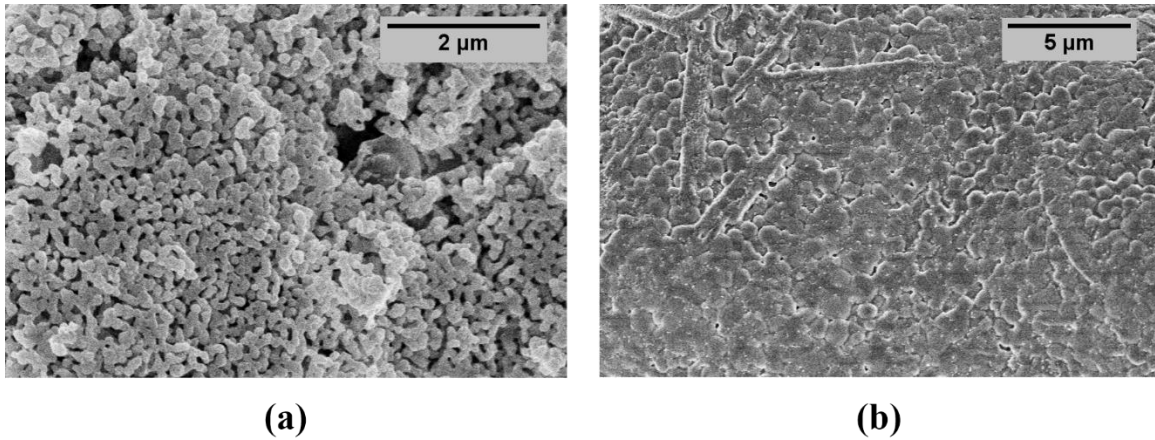


Figure 44. SEM Images of calcined ReEF: a) Calcined ReEF at 800C, 120s, 21% O<sub>2</sub>, b) Calcined ReEF at 800C, 120s, 100% O<sub>2</sub>.

The calcined ReEF obtained from different oxygen concentrations were then tested in the sulfation reactor under the same conditions as we mentioned above. The results are presented in the Figure 45. With the ReEF sorbent produced in lower oxygen calcination, the conversion of the sorbent keeps increasing continuously in the 5min testing time. In this case, the SO<sub>2</sub> can still diffuse through the existing pores into inner surface to continuously react with CaO. It will take longer time before the pore complete closure due to the CaSO<sub>4</sub> layer formation. Thus, a gradual increase in sorbent conversion is observed. However, for the ReEF calcined in high oxygen concentration, the conversion of the sorbent reach an asymptotic value after 2min, especially for the tests in 800 °C. Due to severe sintered surface, SO<sub>2</sub> reacts only on the sorbent surface. The product CaSO<sub>4</sub> layer easily covers the surface which generates strong transport resistance for SO<sub>2</sub> penetrating in to react with CaO. This will well explain what we observe in the Figure 39 and prove



our proposed mechanism. With more oxygen, combustion leads to a more sintered calcined sorbent. The sorbent is non-porous and sulfation reaction is hindered easily by the product layer formation on the surface.

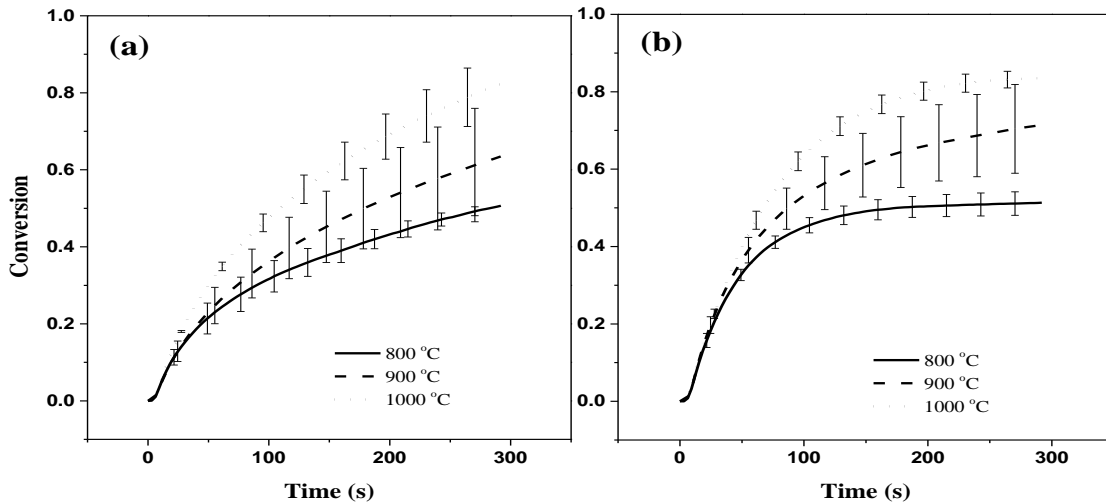


Figure 45. The sulfation behavior of calcined ReEF. a) ReEF calcined at 800C, 120s, 21%O<sub>2</sub>. b) ReEF calcined at 800C, 120s, 100%O<sub>2</sub>.

### **3.3.3.3 Kinetic Modelling of Sulfation of Calcined ReEF**

The kinetic modelling of sorbent sulfation has been extensively studied in the literatures. Two major models (unreacted shrinking core model and grain model) were often applied to describe and predict the sulfation behavior of the sorbents such as CaO, CaCO<sub>3</sub> and Ca(OH)<sub>2</sub>. Both of the model describe the non-catalytic gas-solid reactions. Unreacted shrinking core model was first proposed by Yagi and Kunii<sup>149</sup>. Initially, the gas reacts with the solid on the surface. After a certain time of reaction, the product forms and accumulates as a product layer. The gas diffuses inside the product layer and reacts on the surface of unreacted part. As the time continues, the size of unreacted core shrinks due to the reaction. Thus the sharp boundary between unreacted core and product layer moves towards the center of the spherical particle. Due to the molar

volume change from solid reactant to product. The change of particle size always associates with the reaction. Szekely et al. proposed an unreacted shrinking core model with changing particle size<sup>150</sup>. Because the reaction happens on the sharp interface between unreacted part and product layer, the unreacted shrinking core model is suitable for representing the non-porous material.

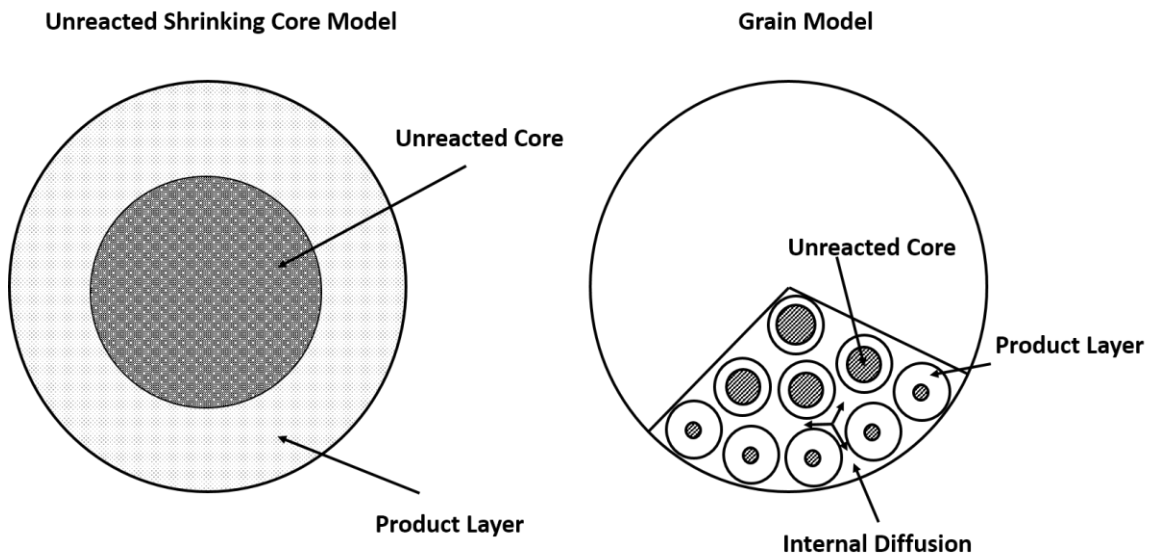


Figure 46. The Unreacted shrinking core model and grain model

Researchers found that some sorbents or nascent calcined sorbents were porous materials. The gas diffuses in the pores and reacts with solid in a wide reaction band instead of a sharp interface. In this case, the unreacted shrinking core model won't predict reaction and diffusion very well. Thus, grain model was proposed by Szekely et al<sup>151</sup> to solve this problem as shown in Figure 46 (b). In grain model, the particle consists of uniform smaller spherical grains. The space between the grains represents the pores in the particle. Reactant gas can react on the grain surface while diffusing in the space between the grains. Each grain follows the unreacted shrinking core model. From the grain model, the grains closed to the surface of the particle have higher conversion than that of the grains inside the particle. Historically, the grain model has been modified by researchers. Hartman and Coughlin incorporated the changing effective diffusivity in

the grain model<sup>152,153</sup>. Ramachandran and Smith considered the reduction in porosity due to the sintering of the sorbent<sup>154</sup>. The grain model is suitable for modeling the porous materials due to the prediction of pore diffusion in the particle.

In our work, the materials used in sulfation reaction was obtained from calcination/combustion of ReEF. Due to the combustion of fibers/plastics in the ReEF, the sorbent is sintered and non-porous. From this point of view, the unreacted shrinking core model is more suitable for the sulfation modeling. Several assumptions are made in this model. First, the particles are assumed as perfect sphere. Second, the temperature keeps uniform during the reaction. The mass transfer biot number was calculated. The result shows  $Bi_m \gg 1$ , which indicates that external mass transfer limitation can be neglected. The detailed mathematical deductions are presented in the Appendix A. Figure 47 shows the results from unreacted shrinking core modelling of two calcined sorbent from ReEF. For the sorbent calcined at 21% O<sub>2</sub>, the model provides a good fitting and prediction (Figure 47 (a)). Two parameters, reaction kinetics and diffusivity, are estimated in the model by fitting the experimental data. The activation energy for the sulfation reaction and gas diffusion are  $43 \pm 11$  KJ/mol and  $125 \pm 28$  KJ/mol, respectively. The estimated parameters are presented in Table 20. However, the model doesn't provide a quite good fitting to the calcined sorbent that was obtained from 100% O<sub>2</sub>. This is probably due to that pore closure happens earlier in more sintered sorbent. The product layer is easy to form, which prevents gas reacts with unreacted core. Thus the reaction rate is controlled by solid state diffusion.

Table 20 kinetics parameters of sulfation for calcined sorbent in 21% O<sub>2</sub>

Temperature (°C)	$k_s$ ( $10^{-2}$ cm/s)	$D_e$ ( $10^{-6}$ cm <sup>2</sup> /s)
800	$1.3 \pm 0.3$	$2.6 \pm 0.6$
900	$2.2 \pm 0.4$	$7.3 \pm 0.6$
1000	$2.7 \pm 0.2$	$20.7 \pm 1.7$

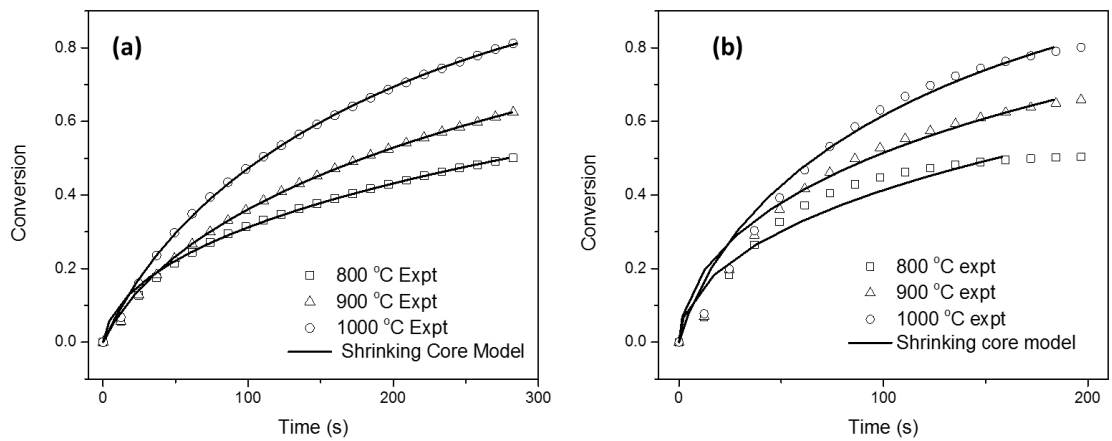


Figure 47. The modelling of sulfation behavior of calcined ReEF. a) ReEF calcined at 800C, 120s, 21%O2. b) ReEF calcined at 800C, 120s, 100%O2.

### 3.3.4 Conclusions

The ReEF fuel contains about 35 wt% of high surface area calcium hydroxide and 65 wt% of non-recyclable fibers and plastics. The compositions of calcium sorbent and RDF vary slightly on different sizes of particle. SEM-EDX presents the calcium sorbent is randomly dispersed on the surface of RDF as well as other impurities from wastes. The desulfurization performance of ReEF was tested in a drop tube sulfation reactor. Combusting the ReEF in a low oxygen environment leads to a high sorbent sulfur take in a long time run. Comparing with the sulfation of pure sorbent, the sulfation of ReEF is delayed by the fibers and plastics combustion. This will prevent the sorbent from early sulfation under high temperature and increase the efficiency of sulfur dioxide capture when co-firing coal with ReEF. The combustion and calcination of ReEF were studied in a horizontal calcination reactor. The results shows the combustion of fibers/plastics of ReEF can enhance the sintering of the sorbent, which leads to a non-porous material. The sulfation is more hindered due to the product layer formation. Unreacted shrinking core was used to estimate the kinetic parameters during the sulfation reaction. For the sorbent produced in the 21% O2

calcination/combustion, the model provides a good prediction. However, the model fails to predict the sulfation of sorbent obtained in 100% O<sub>2</sub> calcination/combustion.

### **3.4 Economic Analysis**

The ReEF process can be applied to the current coal combustion power plant with minimum retrofit. In this thesis, the economics of ReEF process has been estimated and compared to a conventional coal power plant. The estimation of ReEF process is established on the retrofit of a 400 MW conventional coal power plant. The schematic process flow for both process is shown in Figure 48. A material recovery facility is included in the analysis for ReEF production. In conventional coal power plant, since it doesn't use ReEF as feedstock, the MRF is independent, which means there will be no connection between power plant and MRF. However, in ReEF process, the production of ReEF from MRF needs to be transported to power plant for burning. A common way to compare different technologies is to compare the levelized electricity cost (LEC), which is the cost per unit of energy. The definition of LEC is shown in equation 10 and 11

$$\text{LEC} = \frac{\text{Total annualized cost of the plant}}{\text{annual energy produced}} \quad (10)$$

$$\text{LEC} = \text{LEC (Fuel)} + \text{LEC (Capital Cost)} + \text{LEC (O\&M)} + \text{LEC (Other benefits)} \quad (11)$$

Usually, the total annualized cost included capital cost, fuel cost, operation and Maintenance cost (O&M), and other cost. We discussed each of them in the analysis in detail.

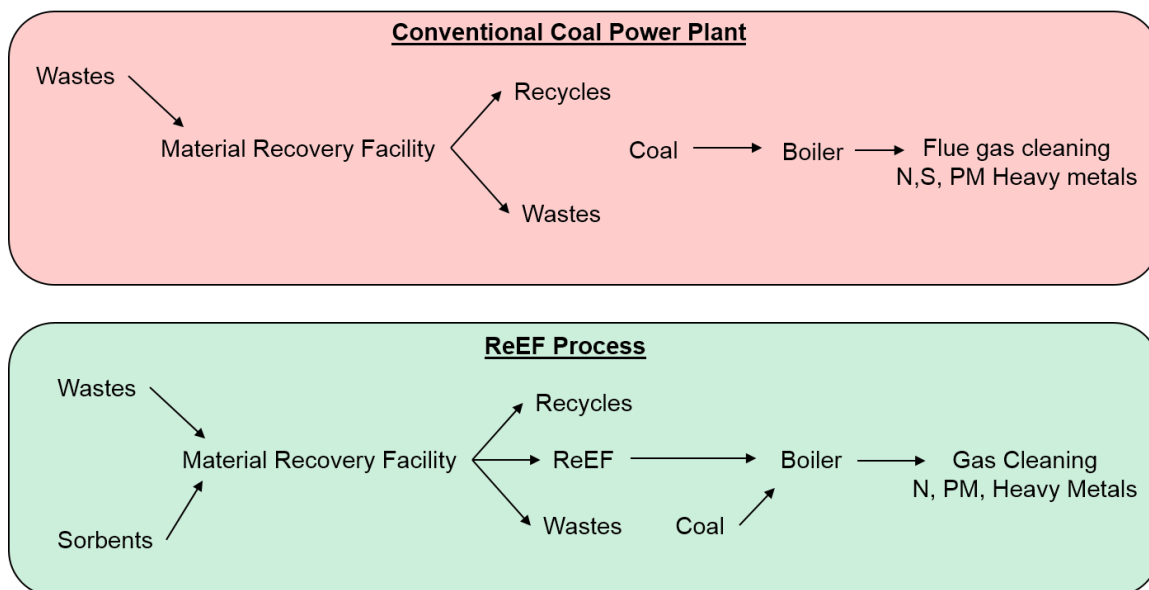


Figure 48. The schematic process flow of conventional coal power plant and ReEF process

### 3.4.1 Fuel Cost

In the conventional coal power plant, the feedstock is 100% coal. Thus, the fuel cost would include the cost of coal and transportation. The coal price is dependent on the type of coal and the location of coal mining factory<sup>155</sup>. In our study, the price of coal is taken as a bituminous coal and the average price across the United States. The cost of transportation of coal is determined by the distance between power plant and coal market and the amount of coal. In our study, since we didn't set a location of the power plant, the cost of fuel for a conventional coal power plant is mainly determined by the price of coal. In the ReEF process, since the fuel consist of two components (ReEF and coal), we need to estimate the cost of each of them. The ratio of ReEF in the fuel mixture is 26 wt% to guarantee the energy output of the plant. The composition of ReEF in our estimation is 65 wt% of RDF and 35 wt% calcium hydroxide. The material cost of ReEF mainly comes from consumption of calcium hydroxide (sorbent).

Table 21: Economic Analysis on the ReEF and Conventional Coal Power Plant

	ReEF Process	Conventional Coal Power Plant
Capacity Factor <sup>156</sup>	0.69	
Efficiency <sup>156</sup>	0.325	
Operating year	35	
Interest rate	3.55 %	
<b>Fuel Cost (\$/y)</b>		
Coal <sup>155</sup>	53591037	61,599,051
ReEF Production <sup>157</sup>	11474564	0
Total fuel cost	65,065,601	61,599,051
<b>Capital Cost<sup>158</sup> (\$)</b>		
Additional feed lime	500,000	0
Spray dry absorber	0	36,000,000
MRF for ReEF Production <sup>159</sup> (150 TPH)	10,597,000	8,597,000
Other direct and indirect cost	1,483,360,000	
Total Capital cost	1,494,457,000	1,527,957,000
<b>O&amp;M Cost<sup>158</sup> (\$/y)</b>		
Fixed O&M cost	12,467,292	
Lime Reagent	0	4,783,006
Solid waste disposal	4,799,898	2,452,682
FGD product disposal	0	1,248,616
Other variable O&M Cost	4,847,000	
MRF O&M Cost	4,975,000	4,975,000
Total O&M Cost	27,089,190	32,372,128
<b>Others Benefits (\$/y)</b>		
Tipping fee <sup>160</sup>	17,461,914	25,831,235
Sale on Recycled Materials <sup>161</sup>	(28,206,294)	(28,206,294)
Total Other benefits	(10,744,378)	(2,375)
<b>LEC Analysis (cent/kwh)</b>		
LEC (Fuel)	2.69	2.54
LEC (Capital)	3.11	3.18
LEC (O&M)	1.12	1.34
LEC (Others)	(0.44)	0.09
<b>Total LEC (cent/kwh)</b>	6.48	6.97
( ): Revenue		

### 3.4.2 Capital Cost

The common units for a conventional power plants include boiler, steam turbine, heat exchangers, baghouse, dry flue gas desulfurization (FGD) control unit, NO<sub>x</sub> control unit, and mercury control unit. The capital cost includes all the materials and construction of units. Other

than that, indirect costs such as land and contingency are also included. ReEF process only requires the minimum retrofit on the current power plant. Compared to coal power plant, at least two modifications needs to be consider. ReEF process is one-step technology that combines combustion and emissions control. The sorbents in the ReEF can remove the SO<sub>2</sub> emission from coal combustion. Thus, the cost of the traditional flue gas desulfurization equipment can be eliminated. However, the pre-mixing of ReEF and coal needs an additional feed line and mixer when applying the ReEF process. With regard to ReEF production, a 150 TPH Material Recover Facility (MRF) is selected for wastes processing. The capital cost of MRF is also considered in both processes. In ReEF process, the production of ReEF requires additional steps (sorbent mixing and ReEF pelletization), which needs more equipment than regular MRF. Thus, an extra capital cost is generated in ReEF process. The detailed capital cost of two process are listed in Table 20. The calculation of LEC on the capital cost is different, since most of capital costs are one-time payment. The annualized cost on the capital is calculation based on the equation 12.

$$\text{LEC (Capital Cost)} = \frac{\text{SC}*(\text{A/P},i,n)}{\text{CF}*8760} \quad (12)$$

SC: Construction Cost / Rated Power

$$(\text{A/P},i,n) \text{ Capital Recovery factor} : \frac{i*(i+1)^n}{(i+1)^n-1}$$

i: interest rate

n: life of the plant

CF: Capacity factor

8760: number of hours in a year



### **3.4.3 Operation and Maintenance Cost**

Fixed O&M cost and variable O&M cost are the two major parts of O&M cost. Fixed O&M cost includes all the fixed labor and non-labor cost. We assume that in the two process, the fixed O&M cost is the same. The variable cost mainly includes daily expense related to the plant operation. In coal power plant, additional flue gas desulfurization sorbent such as lime, limestone need to be purchased. The amount of limestone needed in the conventional coal power plant was calculated by a Calcium to sulfur ratio equals two. Since sorbents are already mixed in RDF in ReEF production, there is no need for cost on reagent. The cost of solid waste disposal includes the disposing bottom ash, cyclone ash and ash from baghouse. In coal process, additional cost is added due to the disposal of flue gas desulfurization ash. In most cases, the coal ash or desulfurization ash can be sold to produce zeolite and gypsum. In our analysis, we assume the ash from both process are disposed. Other variable cost includes active carbon for mercury removal, catalysts for NO<sub>x</sub> removal, water consumption, bags for baghouse and others expenses. As for the O&M in MRF, we assume they have the same cost. The detailed information can be found in Table 21.

### **3.4.4 Other Benefits**

MRF receives wastes and sorts them into various streams. According to the report, 34.5 % of total MSW was recycled in 2012<sup>9</sup>. These recycled materials can be sold as reuse or made for other products. Thus, a revenue is generated through selling recycled products in MRF. The revenue mainly contains sales of recycled fibers, plastics, and metals. 53.8 % of total MSW was non-recyclable and discarded. A tipping fee is imposed when discarding the wastes in landfill. However, the production of ReEF utilizes non-recyclable fiber and plastic, which reduces the amount of wastes that go to landfill. This results in a decrease in tipping fee. In our analysis, the LEC of benefit is calculated by the addition of sales from recycling products and tipping fee for the discarded

wastes. We assume both processes have same revenue on the recycles sale. Compared to conventional coal power plant, the ReEF process has lower tipping fee due to the utilization of non-recyclable fibers and plastics.

The greenhouse gas emission from combustion of fossil fuel is becoming a big concern in society due to the global warming. Carbon dioxide is considered to be a heat-trapping gas and CO<sub>2</sub> emission is dependent on carbon content in the fuels. The carbon tax is levied on the carbon content in the fuels. It provides a potentially cost-effective way to reduce carbon dioxide emission. The carbon tax is charged in a number of countries in European Union such as Denmark, Germany, the UK, Sweden, etc. In United States, carbon tax is only imposed in a few states. The tax is calculated based on per metric ton of carbon dioxide emission and there isn't a uniform tax on carbon dioxide emission. Based on the carbon tax rate provided by Center for Climate and Energy Solutions<sup>162</sup>, the carbon tax is calculated for both conventional power plant and ReEF process (Table 22).

Table 22: Carbon tax on ReEF process and conventional coal plant

Price Source	Unit Price (\$/ton CO <sub>2</sub> emission)	ReEF process (\$/year)	Conventional Coal Plant (\$/year)
Maryland	5.00	10,605,917	11,681,452
California	0.044	95,453	105,133
Finland	30	63,635,507	70,088,713
Netherland	20	42,423,671	46,725,808
Australia	23	48,787,222	53,734,680

Since ReEF contains about 50% of fibers, the carbon emitted from fibers is considered to be neutral. It won't generate additions on carbon dioxide net value. The carbon emission from

fossil fuel is counted by combustion of plastics and coal in ReEF process and coal in conventional process. From Table 22, the tax on carbon emission of ReEF process is lower than that of conventional process due to the combustion of renewable material in ReEF process. From this perspective, ReEF process is more preferred in reducing the GHG emission. Since the carbon tax is not imposed widely in United States, in our analysis, the carbon tax is not included in the economic analysis.

### **3.4.5 Conclusion**

The total LEC of both processes is compared in Table 21. The LEC of ReEF is 6.48 cent/kwh, which is lower than that of conventional process. This indicates that ReEF process is more economic preferred. To analyze the economic feasibility of ReEF process, more complex model including net present value and internal rate of return need to be considered. In this thesis, we provide a simple economic analysis to prove that applying ReEF process can reduce the cost of electricity. Considering environmental benefits associating with ReEF process such as supplementing fossils fuels, reducing greenhouse gas emission, and saving landfill space, we conclude that ReEF process can be beneficial in both economic and environment. The application of ReEF will facilitate the sustainable development in energy production.

## CHAPTER 4

### CONCLUSION AND FUTURE RESEARCH

#### 4.1 Conclusions

##### **4.1.1 Pyrolysis of lignin and lignin model compound**

In this thesis, converting waste lignin to valuable chemicals by pyrolysis technology is presented. Two lignin extracted from Maplewood (solid lignin residue after enzymatic hydrolysis and organosolv lignin) and  $\beta$ -O-4 oligomeric lignin model compound were tested in pyroprobe reactor and TGA system. The intermediate products were comprehensively analyzed by various techniques including GC/MS, FTIR, NMR, TOC, and GPC.

A two-step decomposition is proposed when Maplewood lignin is pyrolyzed. In the first step, lignin decomposed into volatiles and solid products. The solid products were primarily polyaromatics. The polyaromatics further decomposed at a temperature above 325 °C. The volatile species are comprised of light gases and condensable liquid mixture. CO, CO<sub>2</sub>, and H<sub>2</sub>O were major gaseous species. Small amounts of H<sub>2</sub> and CH<sub>4</sub> release were also observed. Condensable liquid products were captured by a nitrogen trap in a pyroprobe reactor and their concentrations were quantitatively measured as a function of pyrolysis temperature. The condensable liquid species were mainly composed of identifiable monomeric phenolics (14–36 carbon %) and unidentifiable heavy tars. The major detectable products were guaiacol, syringol and vanillic acid which result from the cleavage of ether linkages. Elemental analysis and TOC results showed that a larger amount of carbon transferred to the solid char and a larger amount of oxygen transferred to the volatile species. FT-IR and DP- MAS <sup>13</sup>C NMR analysis of the solid intermediate products indicated disappearance of methoxy groups and accumulation of nonprotonated aromatic C–C bonds with the increase in pyrolysis temperature. These results indicate that lignin pyrolysis occurs primarily from cleavage of ether bonds leaving solid

polyaromatic compounds. The fraction of polyaromatics produced from lignin pyrolysis was about 0.69 which is in a good agreement with the values from pyroprobe quantification.

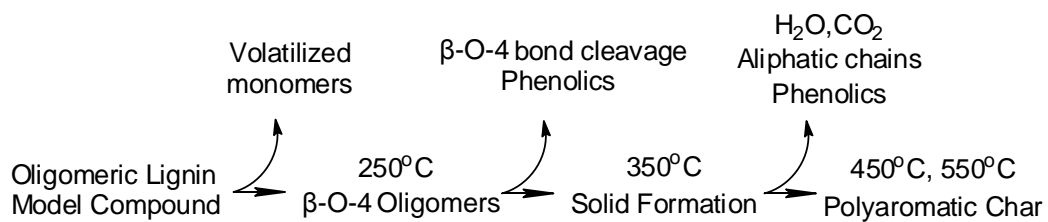


Figure 49: The reaction steps of pyrolysis of lignin model compound

An oligomeric lignin model compound only containing  $\beta$ -O-4 linkage was synthesized and its pyrolysis behavior was studied. The reaction steps with the pyrolysis temperature was proposed as Figure 49. The monomers tend to volatilize below 250 °C leaving the  $\beta$ -O-4 oligomers.  $\beta$ -O-4 linkage is thermally cleaved at the temperature between 250 °C and 350 °C. The phenolic compounds were detected by GC-MS. However, no solid product was observed at 250 °C. The appearance of solid char started at 350 °C. The evolution of solid char involves losing gases such as CO, CO<sub>2</sub>, H<sub>2</sub>, CH<sub>4</sub> and H<sub>2</sub>O. At higher temperatures, highly concentrated polyaromatic char forms. The major product from pyrolysis of this lignin model compound is solid char which accounts for 50–70% of the carbon. Volatile monomeric aromatic compounds are quantified by GC-MS and vanillin is the most abundant product. A free radical dominant reaction pathway is proposed to explain the products formation. Various products are formed by bond cleavages and secondary reactions. Randomly repolymerized radicals are believed to cause char formation.

#### 4.1.2 ReEngineered Feedstock™ for Coal Combustion Emission Control

A new coal combustion technology utilizing Re-Engineered Feedstock™ (ReEF), was evaluated for pulverized coal combustion emission control in this thesis. The ReEF consists of non-

recyclable waste fiber/plastic and commercialized flue gas desulfurization (FGD) sorbent. This novel feedstock is combusted to produce energy while capturing the sulfur dioxide generated during coal combustion

A lab scale fluidized bed combustor was constructed to study the co-firing pulverized coal and various types of ReEF. The enhanced combustion efficiency when co-firing coal and ReEF indicates that ReEF was observed, which indicates ReEF is a promising feedstock for co-firing with coal. Further, coal/ReEF mixtures with Na-based sorbent burned more efficiently than mixtures with Ca based sorbent by 20-30%. Significant reduction of SO<sub>2</sub> emission in combustion flue gas was achieved by premixing coal with ReEF. For the same Ca/S condition, SO<sub>2</sub> reduction by ReEF Mississippi Lime (ML) was higher than that by ReEF Sorbacal Lime (SL). In general, coal/ReEF mixtures emit less NO than pure coal consistent with less nitrogen content in ReEF.

One specific ReEF containing 35 wt% of high surface area calcium hydroxide and 65 wt% of non-recyclable fibers and plastics was studied. A comprehensive characterization was done on the ReEF to reveal its feature. The compositions of calcium sorbent and RDF vary slightly on different sizes of particle. SEM-EDX presents the calcium sorbent is randomly dispersed on the surface of RDF as well as other impurities from wastes. The desulfurization performance of ReEF was tested in a drop tube sulfation reactor. Combusting the ReEF in a low oxygen environment leads to a high sorbent sulfur take in a long time run. Comparing with the sulfation of pure sorbent, the sulfation of ReEF is delayed by the fibers and plastics combustion. This will prevent the sorbent from early sulfation under high temperature and increase the efficiency of sulfur dioxide capture when co-firing coal with ReEF. The combustion and calcination of ReEF are studied in a horizontal calcination reactor. The results shows the combustion of fibers/plastics of ReEF enhances the sintering of sorbents, which leads to a non-porous material. The sulfation is more hindered due to the product layer formation. The application of ReEF will have positive impacts

on the environment and society by supplementing coal combustion, reducing greenhouse gas emissions, and minimizing wastes that will go to landfill.

## **4.2 Future research on pyrolysis of lignin**

### **4.2.2 Pyrolysis of Oligomeric lignin model compound**

In this thesis, the oligomeric lignin model compound is used in pyrolysis study. From the GPC analysis, the average molecular weight of synthesized model compound is 1260 Da, which indicates it contains average 4-5 monomeric units. The effect of degree of polymerization on product distribution from pyrolysis of cellulose model compound has been studied<sup>163</sup>. The results show that simplified empirical model cannot predict the product yields from cellodextrin pyrolysis. However, certain products were observed to be increased continuously with degree of polymerization. In the future research, the effect of chain length of oligomeric lignin model compound on pyrolysis can be studied. By controlling the reaction time and temperature, the degree of polymerization can be varied in synthesizing oligomeric lignin model compound<sup>65</sup>. A series of oligomeric lignin model compounds with various chain length can be studied in pyroprobe-GC/MS system to obtain the product distribution.

In this thesis, TGA were used in the pyrolysis study. One of the major drawbacks of TGA is relative slow heating rate (Maximum 150 °C/min). In present, the heating rate of fast pyrolysis can be 1,000,000 °C/min<sup>164</sup>. To maximize the bio-oil production from biomass, a fast heating rate should be achieved. Thus, compared to TGA, pyroprobe is more suitable for this study. In the future research, experiments with fast heating rate should be conducted in pyroprobe system and products distribution should be analyzed. Other than the limitation of instruments, the dimension of samples can influence sample heating rate. The pyrolysis of bulk and powder sample may be subjected to heat transfer limitation which causes low sample heating rate, pre-reactions, and

secondary reactions. To better understand the chemistry of biomass pyrolysis, a thin-film pyrolysis technique was developed for studying the cellulose pyrolysis<sup>164-167</sup>. A thin film sample is prepared to control the pyrolysis only subjected to isothermal kinetic limitation. In the future research of pyrolyzing oligomeric lignin model compound, the thin film technique can be considered.

#### **4.2.1 Slow pyrolysis of lignin for bio-char production**

Lignin is recalcitrant and solid char residue is the major product from lignin pyrolysis. This gives the opportunity of bio-char production from slow pyrolysis of lignin. Due to its aromatic structure, the bio-char produced from lignin is porous and can be used as cooking, soil improvers, and gas separations. Meanwhile, the product gas from slow pyrolysis mainly consists of CO, H<sub>2</sub>, CH<sub>4</sub> and small hydrocarbons, which can be combusted for energy supply. In the future research, the slow pyrolysis can be applied on lignin and lignin model compound for production of bio-char. The physical properties of bio-char can be characterized by N<sub>2</sub> adsorption, XRD, SEM, etc. The ability of bio-char as an absorber for gases, water, and nutrients needs to be tested.

### **4.3 Future research on Re-Engineered Feedstock™**

#### **4.3.1 Enhance carbon conversion**

In this thesis, a lab scale fluidized bed was constructed for co-firing pulverized coal and ReEF. The feedstock was premixed and loaded in a feeder box. The mixture was sent to the bottom of the reactor through an aguer. The air stream was also fed from the bottom. From the co-firing results as described in Figure 27, the carbon conversion varies from 50% to 90%, which means only 50% to 90% of carbon in the mixture was converted to carbon dioxide. To achieve a better energy conversion, the carbon should be completely converted into carbon dioxide. In our experiments, the carbon was noticed to present in the slag collected from the bottom and soot in



the top part of reactor and flue gas tube. Slags are formed under high temperature due to the melting or volatilizing of metal compounds. In our experiments, the temperature of bottom reactor was as high as 1600 °C. When injecting the feed into reactor, the low melting/boiling point metals melt or volatilize. Coal or carbon can be wrapped inside the glassy melts. Oxygen cannot transport into the melting layer, leaving the unconverted carbon in the slag. Black soot is heavy polyaromatic hydrocarbons which evolves from tars. Tars directly form from pyrolysis of volatile matters in the feedstock. They mainly consists of condensable organic compounds which include oxygenated products, deoxygenated hydrocarbons and polycyclic aromatic hydrocarbons (PAHs). The formation of tar involves the progression from primary tar to secondary tar or further tertiary tar and soot. The tar/soot formation is the indication of incomplete combustion.

To enhance the carbon conversion, a more complete combustion is required. A better mixing between feed and oxygen must achieve. Several methods are proposed here for future research to change gas and solid flow pattern in the reactor. 1). A secondary air inlet needs to be considered on top part of the reactor. Tars can be combusted with additional oxygen input. 2) ReEF and coal can be fed separately. The rate limiting step in combustion is usually char combustion because it involves a solid-gas reaction. Mass transport of oxygen in the porous solid char could be the rate controlling step. Since coal contains more fixed carbon than ReEF, the time required by a complete combustion for coal could be longer than that of ReEF. This requires longer residence time for coal particles in the reactor. Considering this, instead of pre-mixing them, they can be fed separately with coal being fed in the bottom. Additionally, both of potential methods can be utilized together to further facilitate complete burning.

#### **4.3.2 Metal issues in the combustion**

The transformation of metals in the coal combustion has been comprehensive studied<sup>168</sup>. Due to the extreme high temperature (1600 °C), metals in coal and ReEF melt or volatilize, which

would cause severe operation issues including slagging, fouling, and bed agglomeration. The major cause of these problems is low melting and highly volatile alkali and alkaline earth metals and their compounds. If not addressing these problems properly, serious damages would happen to the unit and pipes, which will lead to the shutdown of the plant and lose the profit. Slagging is the deposition of fused or sintered ash on heat transfer and refractory surface in the furnace which is subjected to radiant heat transfer<sup>168</sup>. The prediction of slagging in the reactor is closely related to the ash fusion temperature. The acid to base ratio is frequently used for correlating ash fusion property. The acid oxides such as  $\text{SiO}_2$ ,  $\text{Al}_2\text{O}_3$  and  $\text{TiO}_2$  have higher melting points. The existence of large portion of acid oxides in the ash will increase its fusion temperature. However, base oxides including  $\text{K}_2\text{O}$ ,  $\text{Na}_2\text{O}$ ,  $\text{CaO}$ ,  $\text{MgO}$  and iron oxides will decrease the ash fusion temperature. The slagging indices based on the chemical composition of ash are developed to predict the ash fusion temperature<sup>169</sup>. Moreover, the formation of eutectics between the multiple compounds also results in a low melting temperature ash. Another method to predict the ash fusion temperature is ternary phase diagram which is based on the thermodynamic phase equilibrium. Commercial software such as FactSage developed by the GTT & CRCT is widely used in the research and industry on slagging predictions<sup>170,171</sup>. Fouling is the deposition and condensation of fly ash on the non-radiant convective heat transfer surface when the flue gas temperature is below the ash melting point<sup>168</sup>. The depositions of alkali and alkaline earth compounds are the major cause on the fouling<sup>168,171</sup>. They transport out of the reactor as format of chlorides, hydroxides and sulfates under high temperature. They nucleate and condense on the convective heat transfer surface when the temperature cools down between 850 °C to 550 °C<sup>171</sup>. The vapor alkali compounds react and bound with fly ash forming alkali silicates and deposit on the heat transfer surface. The severe fouling problem can lead to the clogs in the tube, low heat transfer efficiency and corrosion on the surface. Because about 20- 40 wt% of sorbent is added in

the ReEF and most of sorbents are calcium and sodium compounds, the slagging, fouling and bed agglomeration must be considered under the extreme high temperature combustion. Thus, the second future research direction of ReEF can be focused on studying these potential issues caused by alkali and alkaline earth metals.

#### **4.3.3 Gasification of ReEF**

Gasification converts organic materials into combustible syngas under elevated temperatures in controlled amount of oxidants. Advantages of gasification over combustion have been mentioned above. First, gasification provides various options on chemical products including hydrogen, ammonia, methane, methanol, wax, olefins, and transportation fuels. Second, gasification is considered more environmental friendly than combustion. The sulfur, nitrogen ends up in their reducing form, which can be either removed easily or recovered. Additionally, the emission of PCDDs and PCDFs is lower in reducing atmosphere. Third, a coal integrated gasification combined cycle (IGCC) power plant achieved an average of 48% on efficiency while only 32.5% for traditional coal boiler power plant. Moreover, combustion usually requires 20-50% of excess air to achieve the complete burning. To process the same amount of feed, larger gas flow is required in combustion, which usually increases the reactor size.

Gasification is a proven technology on coal conversion and it has been used over 200 years. Technology of coal gasification was first commercialized by London Gas, Light and Coke Company in 1812. It produced town gas for lighting, cooking, heating and industrial use. During 1920s-1960s, the gasification technology was enhanced by other technologies such as Cryogenic separation and Fischer-Tropsch. Coal was the major feed used in the gasification. In the World War II, synthetic fuels were produced from Fischer-Tropsch process using syngas. In 1970s, after the first oil crisis and panic of potential short of natural gas, the coal gasification became more and more popular in energy and chemical productions. Today, more and more integrated gasification combined

cycle power plant based on coal are under construction or planned to be built. Compared to coal, ReEF has higher volatile matter and low fixed carbon. It is easier to gasify ReEF than coal. As a fossil fuel supplement, the application of ReEF as a co-gasification feed would be promising. Additionally, alkali metals (Na, K) are reported to be the catalysts on char gasification and tar reduction<sup>172-175</sup>. However, the amount of sorbent in ReEF should be reduced since no need to remove SO<sub>x</sub> and NO<sub>x</sub>.

## APPENDICES

### APPENDIX A. UNREACTED SHRINKING CORE MODEL

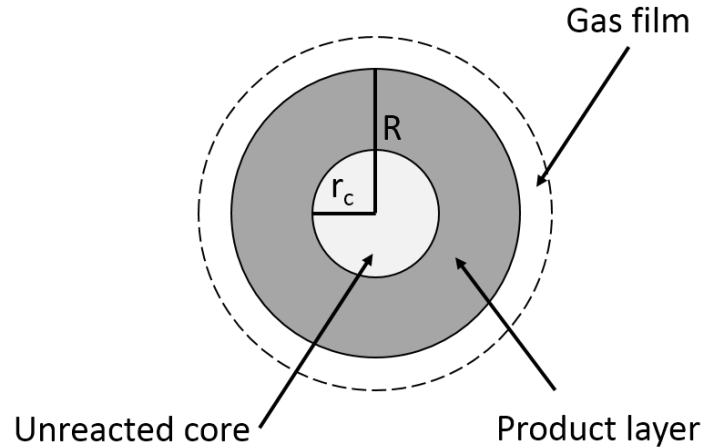


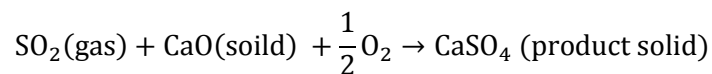
Figure 50. Unreacted shrinking core model

The deduction of unreacted shrinking core model with changing particle size is presented here. As we mentioned above, the external mass transfer is proved to be neglected. The process can be controlled by either by reaction kinetics, diffusion or the combination of both. Some other assumptions with regard to the model are:

1. The solid particle are spherical. The dimension is reduced to one dimension in radius direction.
2. During the process, the temperature is uniform and unchanged.
3. The reaction is first order with respect to  $\text{SO}_2$  and zero order with respect to  $\text{O}_2$ <sup>107,176-</sup>

180.

In this work, the reaction can be presented by



The rate of consumption of CaO equals to the rate of formation of  $\text{CaSO}_4$  and is expressed

as,

$$\frac{dN_B}{dt} = \frac{d(\rho_B V_B)}{dt} = \frac{\rho_B d\left(\frac{4}{3}r_c^3\right)}{dt}$$

The conversion of CaO to CaSO<sub>4</sub> is expressed by:

$$1 - X_B = \frac{\text{Volume of unreacted core}}{\text{Original volume of particle}} = \frac{\frac{4}{3}\pi r_c^3}{\frac{4}{3}\pi R^3} = \left(\frac{r_c}{R}\right)^3$$

If the process is under reaction control, the rate of consumption of gas SO<sub>2</sub> (Gas A) is given by:

$$\frac{-dN_A}{dt} = 4\pi r_c^2 k_s C_A = -\frac{dN_B}{dt} = \rho_B 4\pi r_c^2 \frac{dr_c}{dt}$$

C<sub>A</sub> is the gas concentration in the interface. Thus,

$$\frac{dr_c}{dt} = \frac{k_s C_A}{\rho_B}$$

Initial condition is t=0, r<sub>c</sub>= R. By integrate on both side, the time of required conversion is

$$t = \frac{\rho_B R}{k_s C_A} \left(1 - \frac{r_c}{R}\right)$$

$$t = \tau \left(1 - (1 - X_B)^{\frac{1}{3}}\right) \quad (13)$$

$$\tau = \frac{\rho_B R}{k_s C_A} \quad (14)$$

If the process is under diffusion control,

$$\frac{-dN_A}{dt} = 4D_e \frac{dC_A}{dr} \pi r^2$$

Thus,

$$4\pi D_e dC_A = \left(\frac{-dN_A}{dt}\right) \frac{dr}{r^2}$$

Integrating on both side from r<sub>c</sub> to R results in,

$$\frac{-dN_A}{dt} = \frac{4\pi D_e (C_A - C_{AS})}{\left(\frac{1}{r_c} - \frac{1}{R}\right)}$$

Since  $C_{AS}$  is nearly zero, the equation can be further deduced to

$$\frac{-dN_A}{dt} = \frac{4\pi D_e C_A}{\left(\frac{1}{r_c} - \frac{1}{R}\right)} = \frac{dN_B}{dt} = \rho_B 4\pi r_c^2 \frac{dr_c}{dt}$$

Therefore,

$$\left(r_c - \frac{r_c^2}{R}\right) dr_c = \frac{D_e C_A}{\rho_B} dt$$

Initial condition  $t=0, r_c=R$ ,

$$t = \sigma \left(1 - 3(1 - X_B)^{\frac{2}{3}} + 2(1 - X_B)\right) \quad (15)$$

$$\sigma = \frac{\rho_B R^2}{6D_e C_A} \quad (16)$$

The combination of both control can be expressed as,

$$t = \sigma P(X) + \tau g(X)$$

$$g(X) = \left(1 - (1 - X_B)^{\frac{1}{3}}\right)$$

$$P(X) = \left(1 - 3(1 - X_B)^{\frac{2}{3}} + 2(1 - X_B)\right)$$

During the sulfation, the volume of particle changes due to the molar volume difference between CaO and CaSO<sub>4</sub>. The ratio of molar volume of solid product is expressed as  $Z = 2.72$ , Thus the combination of both diffusion and reaction equation can be written as.

$$t = \sigma P(X) + \tau g(X)$$

$$g(X) = \left(1 - (1 - X_B)^{\frac{1}{3}}\right)$$

$$P(X) = 3 \left( \frac{Z - (Z + (1 - Z)(1 - X_B))^{2/3}}{Z - 1} - (1 - X)^{2/3} \right)$$

## APPENDIX B. NOMENCLATURE

APM: Advanced product manufacturing

$Bi_m$ : Mass transfer biot number

$C_A$ : Bulk Concentration of  $SO_2$  or concentration of  $SO_2$  in the interface in reaction control, mol/cm<sup>3</sup>

CHP: Combined heat and power

$D_e$ : Product layer diffusivity, cm<sup>2</sup>/s

DME: Dimethyl ether

DFT: Density functional theory

DP-MAS: Direct polarization-magic angle spinning

EDX: Energy-dispersive X-ray spectroscopy

ESP: Electrostatic precipitator

FBC: fluidized bed combustor

FGD: Flue gas desulfurization

FT-IR: Fourier transform infrared spectroscopy

GPC: Gel permeation chromatograph

HDPE: High density polyethylene

IGCC: Integrated gasification combined cycle

$k_s$ : Reaction rate constant of sulfation, cm/s

LEC: Levelized electricity cost

ML: Mississippi lime

MMPP: Multi-material processing platform

MS: Mass spectroscopy

MSW: Municipal solid waste

MW: Molecular weight



MTBE: Methyl tertiary butyl ether

$N_B$ : Mole of CaO, mol/cm<sup>3</sup>

$N_A$ : Mole of SO<sub>2</sub>, mol/cm<sup>3</sup>

NMR: Nuclear magnetic resonance

OD: Outer diameter

O&M: Operation and maintenance

PAH: Polyaromatic hydrocarbon

PCDDs: Polychlorinated dibenzo-p-dioxins

PCDFs: Polychlorinated dibenzofurans

PET: polyethylene terephthalate

PPE: Phenethyl phenyl ether

PVC: Polyvinyl chloride

RDF: Refused derived fuel

ReEF: ReEngineered Feedstock

R: Radius of particle, cm

R/P: Reserve to production

$r_c$ : Radius of unreacted core, cm

SB: Sodium bicarbonate

SEM: Scanning electron microscope

SL: Sorbacal lime

t: reaction time, s

TGA: Thermogravimetric analysis

THF: Tetrahydrofuran

TOC: Total organic carbon

$V_B$ : Volume of CaO,  $\text{cm}^3$

WTE: Waste to energy

$X_B$ : conversion of CaO

Z: ratio of the molar volume of solid product to solid reactant

*Greek Letters*

$\rho_B$  : Molar density of CaO,  $\text{mol}/\text{cm}^3$

$\tau$ : Defined by equation 14.

$\sigma$ : Defined by equation 16

## BIBLIOGRAPHY

- (1) BP. *BP Energy Outlook 2035*; 2014.
- (2) BP. *BP Statistics Review*; 2014.
- (3) BP. *BP Statistical Review of World Energy*; 2013.
- (4) REN21. *Renewables 2010 Global Status Report*; 2010.
- (5) EIA. U.S. Electricity Generation by Fuel, All Sectors <http://www.eia.gov/forecasts/steo/data.cfm> .
- (6) EIA Bioenergy. *Large Industrial Users of Energy Biomass*; 2013.
- (7) EPA. Municipal Solid Waste <http://www.epa.gov/epawaste/nonhaz/municipal/>.
- (8) EPA. Waste Management Options <http://www.epa.gov/osw/homeland/options.htm>.
- (9) EPA. *Municipal Solid Waste Generation, Recycling, and Disposal in the United States: Facts and Figures for 2012*; 2012.
- (10) IEA. *IEA Energy Technology Essentials*; 2007.
- (11) Spath, P. *Technical and Economic Assessment of Synthesis Gas to Fuels and Chemicals with Emphasis on the Potential for Biomass-Derived Syngas*; 2003.
- (12) Ioannidou, O.; Zabaniotou, a.; Antonakou, E. V.; Papazisi, K. M.; Lappas, a. a.; Athanassiou, C. Investigating the Potential for Energy, Fuel, Materials and Chemicals Production from Corn Residues (cobs and Stalks) by Non-Catalytic and Catalytic Pyrolysis in Two Reactor Configurations. *Renew. Sustain. Energy Rev.* **2009**, *13*, 750–762.
- (13) Zhou, C.-H.; Xia, X.; Lin, C.-X.; Tong, D.-S.; Beltramini, J. Catalytic Conversion of Lignocellulosic Biomass to Fine Chemicals and Fuels. *Chem. Soc. Rev.* **2011**, *40*, 5588–5617.
- (14) Dickerson, T.; Soria, J. Catalytic Fast Pyrolysis: A Review. *Energies* **2013**, *6*, 514–538.
- (15) Zakzeski, J.; Bruijninx, P. C. A.; Jongerius, A. L.; Weckhuysen, B. M. The Catalytic Valorization of Lignin for the Production of Renewable Chemicals. *Chem. Rev.* **2010**, *110*, 3552–3599.
- (16) Jae, J.; Tompsett, G. A.; Lin, Y.-C.; Carlson, T. R.; Shen, J.; Zhang, T.; Yang, B.; Wyman, C. E.; Conner, W. C.; Huber, G. W. Depolymerization of Lignocellulosic Biomass to Fuel Precursors: Maximizing Carbon Efficiency by Combining Hydrolysis with Pyrolysis. *Energy Environ. Sci.* **2010**, *3*, 358–365.

- (17) Ralph, J.; Lundquist, K.; Brunow, G.; Lu, F.; Kim, H.; Schatz, P.; Marita, J.; Hatfield, R.; Ralph, S.; Christensen, J.; et al. Lignins: Natural Polymers from Oxidative Coupling of 4-Hydroxyphenyl- Propanoids. *Phytochem. Rev.* **2004**, *3*, 29–60.
- (18) Federation, R. Oxidative Delignification in the Presence of Molybdovanadophosphate Heteropolyanions" Mechanism and Kinetic Studies. **1998**, *167*, 123–139.
- (19) Dorrestijn, E.; Laarhoven, L. J. J.; Arends, I. W. C. E.; Mulder, P. The Occurrence and Reactivity of Phenoxy Linkages in Lignin and Low Rank Coal. *J. Anal. Appl. Pyrolysis* **2000**, *54*, 153–192.
- (20) Jiang, G.; Nowakowski, D. J.; Bridgwater, A. V. A Systematic Study of the Kinetics of Lignin Pyrolysis. *Thermochim. Acta* **2010**, *498*, 61–66.
- (21) Gierer, J. Chemistry of Delignification. *Wood Sci. Technol.* **1985**, *19*, 289–312.
- (22) Pan, X.; Gilkes, N.; Kadla, J.; Pye, K.; Saka, S.; Gregg, D.; Ehara, K.; Xie, D.; Lam, D.; Saddler, J. Bioconversion of Hybrid Poplar to Ethanol and Co-Products Using an Organosolv Fractionation Process: Optimization of Process Yields. *Biotechnol. Bioeng.* **2006**, *94*, 851–861.
- (23) Pla, F.; Dolk, M.; Yan, J. F.; Mccarthy, J. L. Lignin 23 . Macromolecular Characteristics of Alkali Lignin and Organosolv Lignin from Black Cottonwoodla Delignification of Cottonwood. **1986**, *30*, 1471–1477.
- (24) Capanema, E. A.; Balakshin, M. Y.; Kadla, J. F. Quantitative Characterization of a Hardwood Milled Wood Lignin by Nuclear Magnetic Resonance Spectroscopy. *J. Agric. Food Chem.* **2005**, *53*, 9639–9649.
- (25) Sievers, C.; Valenzuela-Olarte, M. B.; Marzioletti, T.; Musin, I.; Agrawal, P. K.; Jones, C. W. Ionic-Liquid-Phase Hydrolysis of Pine Wood. *Ind. Eng. Chem. Res.* **2009**, *48*, 1277–1286.
- (26) Ferdous, D.; Dalai, A. K.; Bej, S. K.; Thring, R. W. Pyrolysis of Lignins: Experimental and Kinetics Studies. *Energy & Fuels* **2002**, *16*, 1405–1412.
- (27) Vtirhegyi, G.; Antal, M. J.; Jakab, E.; Szab, P. Kinetic Modeling of Biomass Pyrolysis '. **1997**, *2370*.
- (28) Gardner, D. J.; Schultz, T. P.; McGinnis, G. D. The Pyrolytic Behavior of Selected Lignin Preparations. *J. Wood Chem. Technol.* **1985**, *5*, 85–110.
- (29) Pandey, M. P.; Kim, C. S. Lignin Depolymerization and Conversion: A Review of Thermochemical Methods. *Chem. Eng. Technol.* **2011**, *34*, 29–41.
- (30) Sharma, R. K.; Wooten, J. B.; Baliga, V. L.; Lin, X.; Geoffrey Chan, W.; Hajaligol, M. R. Characterization of Chars from Pyrolysis of Lignin. *Fuel* **2004**, *83*, 1469–1482.

- (31) Iatridis, B.; Gavalas, G. R. Pyrolysis of Precipitated Kraft Lignin. *Ind. Eng. Chem. Prod. Res. Dev.* **1979**, *18*, 127–130.
- (32) Process, C.; Dev, D.; Nunn, T. R.; Howard, J. B.; Longwell, J. P.; Peters, W. A. Product Compositions and Kinetics in the Rapid Pyrolysis of MiHed Wood Lignin. **1985**, 844–852.
- (33) Suzukp, A.; Imaib, K. Analysis of Rice ( *Oryza Sativu L.* ) Lignin by Pyrolysis-Gas Chromatography. **1995**, 2370.
- (34) Acta, E. T. Thermochemica Acta Pyrolysis of Lignin and IR Analysis of Residues. **1997**, *293*, 39–46.
- (35) Bocchini, P.; Galletti, G. .; Camarero, S.; Martinez, a. . Absolute Quantitation of Lignin Pyrolysis Products Using an Internal Standard. *J. Chromatogr. A* **1997**, *773*, 227–232.
- (36) Caballero, J.; Font, R.; Marcilla, A. Study of the Primary Pyrolysis of Kraft Lignin at High Heating Rates: Yields and Kinetics. ... *Anal. Appl. pyrolysis* **1996**, 2370.
- (37) Jiang, G.; Nowakowski, D. J.; Bridgwater, A. V. Effect of the Temperature on the Composition of Lignin Pyrolysis Products. *Energy & Fuels* **2010**, *24*, 4470–4475.
- (38) Nowakowski, D. J.; Bridgwater, A. V; Elliott, D. C.; Meier, D.; de Wild, P. Lignin Fast Pyrolysis: Results from an International Collaboration. *J. Anal. Appl. Pyrolysis* **2010**, *88*, 53–72.
- (39) Avni, E.; Coughlin, R. W. Kinetic Analysis of Lignin Pyrolysis Using Non-Isothermal TGA Data. *Thermochem. Acta* **1985**, *90*, 157–167.
- (40) Ferdous, D.; Dalai, A.; Bej, S.; Thring, R. Pyrolysis of Lignins: Experimental and Kinetics Studies. *Energy & Fuels* **2002**, 1405–1412.
- (41) Gustafsson, C.; Richards, T. Pyrolysis Kinetics of Washed Precipitated Lignin. *BioResources* **2008**, *4*, 26–37.
- (42) Liu, Q.; Wang, S.; Zheng, Y.; Luo, Z.; Cen, K. Mechanism Study of Wood Lignin Pyrolysis by Using TG–FTIR Analysis. *J. Anal. Appl. Pyrolysis* **2008**, *82*, 170–177.
- (43) Cho, J.; Chu, S.; Dauenhauer, P. J.; Huber, G. W. Kinetics and Reaction Chemistry for Slow Pyrolysis of Enzymatic Hydrolysis Lignin and Organosolv Extracted Lignin Derived from Maplewood. *Green Chem.* **2012**, *14*, 428.
- (44) Patwardhan, P. R.; Brown, R. C.; Shanks, B. H. Understanding the Fast Pyrolysis of Lignin. *ChemSusChem* **2011**, *4*, 1629–1636.
- (45) Beis, S.; Mukkamala, S.; Hill, N.; Joseph, J. Fast Pyrolysis of Lignins. ... **2010**, *5*, 1408–1424.

- (46) Weingarten, R.; Tompsett, G. A.; Conner Jr., W. C.; Huber, G. W. Design of Solid Acid Catalysts for Aqueous-Phase Dehydration of Carbohydrates: The Role of Lewis and Brønsted Acid Sites. *J. Catal.* **2011**, *279*, 174–182.
- (47) Patwardhan, P. R.; Dalluge, D. L.; Shanks, B. H.; Brown, R. C. Distinguishing Primary and Secondary Reactions of Cellulose Pyrolysis. *Bioresour. Technol.* **2011**, *102*, 5265–5269.
- (48) Patwardhan, P. R.; Brown, R. C.; Shanks, B. H. Product Distribution from the Fast Pyrolysis of Hemicellulose. *ChemSusChem* **2011**, *4*, 636–643.
- (49) Mani, T.; Murugan, P.; Mahinpey, N. Determination of Distributed Activation Energy Model Kinetic Parameters Using Simulated Annealing Optimization Method for Nonisothermal Pyrolysis of Lignin. **2009**, 1464–1467.
- (50) Vuori, A. I.; Bredenbergh, J. B. Thermal Chemistry Pathways of Substituted Anisoles. *Ind. Eng. Chem. Res.* **1987**, *26*, 359–365.
- (51) Klein, M. T. Model Pathways in Lignin Thermolysis, Massachusetts Institute of Technology, 1981.
- (52) Liu, C.; Zhang, Y.; Huang, X. Study of Guaiacol Pyrolysis Mechanism Based on Density Function Theory. *Fuel Process. Technol.* **2014**, *123*, 159–165.
- (53) Arends, I. W. C. E.; Louw, R.; Mulder, P. Kinetic Study of the Thermolysis of Anisole in a Hydrogen Atmosphere. *J. Phys. Chem.* **1993**, 7914–7925.
- (54) Stein, S. E.; Rukkers, J. M.; Brown, R. L. *NIST Structure and Properties Database and Estimation*; 1994.
- (55) Britt, P. F.; Buchanan, A. C.; Cooney, M. J.; Martineau, D. R. Flash Vacuum Pyrolysis of Methoxy-Substituted Lignin Model Compounds. *J. Org. Chem.* **2000**, *65*, 1376–1389.
- (56) Beste, A.; Ili, A. C. B.; Harrison, R. J. Computational Prediction of R / Selectivities in the Pyrolysis of Oxygen-Substituted Phenethyl Phenyl Ethers. **2008**, 4982–4988.
- (57) Beste, A.; Ili, A. C. B.; Able, T. Computational Study of Bond Dissociation Enthalpies for Lignin Model Compounds. Substituent Effects in Phenethyl Phenyl Ethers. *J. Org. Chem.* **2009**, *74*, 2837–2841.
- (58) Younker, J. M.; Beste, A.; Buchanan, A. C. Computational Study of Bond Dissociation Enthalpies for Substituted B-O-4 Lignin Model Compounds. *Chemphyschem* **2011**, *12*, 3556–3565.
- (59) Beste, A.; Buchanan, A. C. Kinetic Simulation of the Thermal Degradation of Phenethyl Phenyl Ether, a Model Compound for the B-O-4 Linkage in Lignin. *Chem. Phys. Lett.* **2012**, *550*, 19–24.

- (60) Beste, A.; Buchanan, a. C. Substituent Effects on the Reaction Rates of Hydrogen Abstraction in the Pyrolysis of Phenethyl Phenyl Ethers. *Energy & Fuels* **2010**, *24*, 2857–2867.
- (61) Kawamoto, H.; Ryoritani, M.; Saka, S. Different Pyrolytic Cleavage Mechanisms of B-Ether Bond Depending on the Side-Chain Structure of Lignin Dimers. *J. Anal. Appl. Pyrolysis* **2008**, *81*, 88–94.
- (62) Hosoya, T.; Kawamoto, H.; Saka, S. Role of Methoxyl Group in Char Formation from Lignin-Related Compounds. *J. Anal. Appl. Pyrolysis* **2009**, *84*, 79–83.
- (63) Hosoya, T.; Kawamoto, H.; Saka, S. Secondary Reactions of Lignin-Derived Primary Tar Components. *J. Anal. Appl. Pyrolysis* **2008**, *83*, 78–87.
- (64) Liu, J.; Wu, S.; Lou, R. Chemical Structure and Pyrolysis Response of Beta-O-4 Lignin Model Polymer. *BioResources* **2011**, *6*, 1079–1093.
- (65) Katahira, R.; Kamitakahara, H.; Takano, T.; Nakatsubo, F. Synthesis of B-O-4 Type Oligomeric Lignin Model Compound by the Nucleophilic Addition of Carbanion to the Aldehyde Group. *J. Wood Sci.* **2006**, *52*, 255–260.
- (66) Yang, H.; Yan, R.; Chen, H.; Lee, D. H.; Zheng, C. Characteristics of Hemicellulose, Cellulose and Lignin Pyrolysis. *Fuel* **2007**, *86*, 1781–1788.
- (67) Cozzani, V.; Lucchesi, A.; Stoppato, G.; Maschio, G. A New Method to Determine the Composition of Biomass by Thermogravimetric Analysis. *Can. J. Chem. Eng.* **1997**, *75*, 127–133.
- (68) Lin, Y.; Cho, J.; Tompsett, G. A.; Westmoreland, P. R.; Huber, G. W. Kinetics and Mechanism of Cellulose Pyrolysis. **2009**, 20097–20107.
- (69) Cho, J.; Davis, J. M.; Huber, G. W. The Intrinsic Kinetics and Heats of Reactions for Cellulose Pyrolysis and Char Formation. *ChemSusChem* **2010**, *3*, 1162–1165.
- (70) Antal, M. J.; Grønli, M. The Art, Science, and Technology of Charcoal Production†. *Ind. Eng. Chem. Res.* **2003**, *42*, 1619–1640.
- (71) Vispute, T. P.; Zhang, H.; Sanna, A.; Xiao, R.; Huber, G. W. Renewable Chemical Commodity Feedstocks from Integrated Catalytic Processing of Pyrolysis Oils. *Science* **2010**, *330*, 1222–1227.
- (72) Zhang, H.; Cheng, Y.-T.; Vispute, T. P.; Xiao, R.; Huber, G. W. Catalytic Conversion of Biomass-Derived Feedstocks into Olefins and Aromatics with ZSM-5: The Hydrogen to Carbon Effective Ratio. *Energy Environ. Sci.* **2011**, *4*, 2297.
- (73) Pasquali, C. E. L.; Herrera, H. Pyrolysis of Lignin and IR Analysis of Residues. *Thermochim. Acta* **1997**, *293*, 39–46.

- (74) Sharma, R. K.; Wooten, J. B.; Baliga, V. L.; Lin, X.; Geoffrey Chan, W.; Hajaligol, M. R. Characterization of Chars from Pyrolysis of Lignin. *Fuel* **2004**, *83*, 1469–1482.
- (75) Wang, N.; Low, M. J. D. Spectroscopic Studies of Carbons. XV. The Pyrolysis of a Lignin. *Mater. Chem. Phys.* **1990**, *26*, 67–80.
- (76) Britt, P. F.; Buchanan, A. C.; Cooney, M. J.; Martineau, D. R. Flash Vacuum Pyrolysis of Methoxy-Substituted Lignin Model Compounds. *J. Org. Chem.* **2000**, *65*, 1376–1389.
- (77) Ben, H.; Ragauskas, A. J. NMR Characterization of Pyrolysis Oils from Kraft Lignin. **2011**, 2322–2332.
- (78) Bayerbach, R.; Nguyen, V. D.; Schurr, U.; Meier, D. Characterization of the Water-Insoluble Fraction from Fast Pyrolysis Liquids (pyrolytic Lignin): Part III. Molar Mass Characteristics by SEC, MALDI-TOF-MS, LDI-TOF-MS, and Py-FIMS. *J. Anal. Appl. Pyrolysis* **2006**, *77*, 95–101.
- (79) Beste, A.; III, A. B. Computational Study of Bond Dissociation Enthalpies for Lignin Model Compounds. Substituent Effects in Phenethyl Phenyl Ethers. *J. Org. Chem.* **2009**, *74*, 2837–2841.
- (80) Elder, T. A Computational Study of Pyrolysis Reactions of Lignin Model Compounds. *Holzforschung* **2010**, *64*, 435.
- (81) Klein, M. T.; Virk, P. S. Model Pathways in Lignin Thermolysis. 1. Phenethyl Phenyl Ether. *Ind. Eng. Chem. Fundam.* **1983**, *22*, 35–45.
- (82) International Environmental Technology Centre. *Solid Waste Management*; 2006.
- (83) *BP Statistical Review of World Energy, June 2013.*
- (84) *U.S. Energy Information Administration [Http://www.eia.gov](http://www.eia.gov) 2013.*
- (85) Gullett, B. .; Ghorishi, B.; Keeney, R.; Huggins, F. E. Mercuric Chloride Capture by Alkaline Sorbents. In *Proceedings of the Air & Waste Management Association's Annual Conference & Exhibition*; 2000.
- (86) *National Ambient Air Quality Standards (NAAQS) from EPA through the Clean Air Act.*
- (87) *Flue Gas Analysis in Industry, Testo, 2010.*
- (88) Alter, H. The History of Refuse-Derived Fuels. *Resour. Conserv.* **1987**, *15*, 251–275.
- (89) Manninen, H. CO-COMBUSTION OF REFUSE-DERIVED AND PACKAGING-DERIVED FUELS (RDF AND PDF) WITH CONVENTIONAL FUELS. *Waste Management & Research*, 1997, *15*, 137–147.



- (90) Manninen, H. Co-Combustion of Refuse-Derived and Packaging-Derived Fuels (Rdf and Pdf) With Conventional Fuels. *Waste Manag. Res.* **1997**, *15*, 137–147.
- (91) Desroches-Ducarne, E.; Marty, E.; Martin, G.; Delfosse', L. Co-Combustion of Coal and Municipal Solid Waste in a Circulating Fluidized Bed. *Fuel* **1998**, *77*, 1311–1315.
- (92) Chang, Y.-H.; Chen, W. C.; Chang, N.-B. Comparative Evaluation of RDF and MSW Incineration. *J. Hazard. Mater.* **1998**, *58*, 33–45.
- (93) Liu, D. C.; Zhang, C. L.; Mi, T.; Shen, B. X.; Feng, B. Reduction of N<sub>2</sub>O and NO Emissions by Co-Combustion of Coal and Biomass. *J. Inst. Energy* **2002**, *75*, 81–84.
- (94) Silvennoinen, J.; Roppo, J.; Nurminen, R. Co-Combustion of Coal With RDF and Biomass: Prevention of Chlorine Deposition by Using Coal Ash Alkali Absorption Ability. **2005**.
- (95) Wan, H.-P.; Chang, Y.-H.; Chien, W.-C.; Lee, H.-T.; Huang, C. C. Emissions during Co-Firing of RDF-5 with Bituminous Coal, Paper Sludge and Waste Tires in a Commercial Circulating Fluidized Bed Co-Generation Boiler. *Fuel* **2008**, *87*, 761–767.
- (96) Kupka, T.; Mancini, M.; Irmer, M.; Weber, R. Investigation of Ash Deposit Formation during Co-Firing of Coal with Sewage Sludge, Saw-Dust and Refuse Derived Fuel. *Fuel* **2008**, *87*, 2824–2837.
- (97) Saidur, R.; Abdelaziz, E. a.; Demirbas, a.; Hossain, M. S.; Mekhilef, S. A Review on Biomass as a Fuel for Boilers. *Renew. Sustain. Energy Rev.* **2011**, *15*, 2262–2289.
- (98) Wagland, S. T.; Kilgallon, P.; Coveney, R.; Garg, a; Smith, R.; Longhurst, P. J.; Pollard, S. J. T.; Simms, N. Comparison of Coal/solid Recovered Fuel (SRF) with Coal/refuse Derived Fuel (RDF) in a Fluidized Bed Reactor. *Waste Manag.* **2011**, *31*, 1176–1183.
- (99) Wu, H.; Glarborg, P.; Frandsen, F. J.; Dam-Johansen, K.; Jensen, P. A.; Sander, B. Trace Elements in Co-Combustion of Solid Recovered Fuel and Coal. *Fuel Process. Technol.* **2013**, *105*, 212–221.
- (100) Gullett, B. The Effect of Cofiring High-Sulfur Coal with Municipal Waste on Formation of Polychlorinated Dibenzodioxin and Polychlorinated Dibenzofuran. *Environ. Eng. Sci.* **1998**, *15*, 59–70.
- (101) Piao, G.; Aono, S.; Kondoh, M.; Yamazaki, R.; Mori, S. Combustion Test of Refuse Derived Fuel in a Fluidized Bed. *Waste Manag.* **2000**, *20*, 443–447.
- (102) Kobayashi, N.; Itaya, Y.; Piao, G.; Mori, S.; Kondo, M.; Hamai, M.; Yamaguchi, M. The Behavior of Flue Gas from RDF Combustion in a Fluidized Bed. *Powder Technol.* **2005**, *151*, 87–95.
- (103) Saito, H.; Kosugi, S.; Sato, K. The Revolving-Type Fluidized-Bed Incinerator: Its Basic Performance in MSW Combustion. *Waste Manag. Res.* **1988**, *6*, 261–270.

- (104) Tuppurainen, K.; Halonen, I.; Ruokojärvi, P.; Tarhanen, J.; Ruuskanen, J. Formation of PCDDs and PCDFs in Municipal Waste Incineration and Its Inhibition Mechanisms: A Review. *Chemosphere* **1998**, *36*, 1493–1511.
- (105) Orbey, N.; Dogu, G.; Dogu, T. Breakthrough Analysis of Noncatalytic Solid-Gas Reactions: Reaction of SO<sub>2</sub> with Calcined Limestone. *Can. J. Chem. Eng.* **1982**, *60*, 314–318.
- (106) Stouffer, M. R.; Yoon, H. An Investigation of CaO Sulfation Mechanisms in Boiler Sorbent Injection. *AIChE J.* **1989**, *35*, 1253–1262.
- (107) Hu, G.; Damjohansen, K.; Wedel, S.; Peterhansen, J. Review of the Direct Sulfation Reaction of Limestone. *Prog. Energy Combust. Sci.* **2006**, *32*, 386–407.
- (108) Hlincik, T.; Buryan, P. Desulfurization of Boiler Flue Gas by Means of Activated Calcium Oxide. *Fuel Process. Technol.* **2013**, *111*, 62–67.
- (109) Stewart, M. C.; Manovic, V.; Anthony, E. J.; Macchi, A. Enhancement of Indirect Sulphation of Limestone by Steam Addition. *Environ. Sci. Technol.* **2010**, *44*, 8781–8786.
- (110) Liu, G. Q.; Itaya, Y.; Yamazaki, R.; Mori, S.; Yamaguchi, M.; Kondoh, M. Fundamental Study of the Behavior of Chlorine during the Combustion of Single RDF. *Waste Manag.* **2001**, *21*, 427–433.
- (111) Chyang, C.-S.; Han, Y.-L.; Wu, L.-W.; Wan, H.-P.; Lee, H.-T.; Chang, Y.-H. An Investigation on Pollutant Emissions from Co-Firing of RDF and Coal. *Waste Manag.* **2010**, *30*, 1334–1340.
- (112) Bai, D. Systems and Methods for Producing Engineered Fuel Feedstocks with Reduced Chlorine Content. 20130298455, 2013.
- (113) Bai, D. Systems and Methods for Processing a Heterogeneous Waste Stream. 20120305686, 2012.
- (114) Bai, D. Systems and Methods for Producing Engineered Fuel Feed Stocks from Waste Material. 20120304536, 2012.
- (115) Bohlig, J. W.; Bai, D. Engineered Fuel Feed Stock. 20130055630, 2012.
- (116) EPA. *Air Pollution Control Technology Fact Sheet*; p. EPA-452/F-03-034.
- (117) Flue Gas Desulfurization (Acid Gas Removal) Systems  
[http://yosemite.epa.gov/oaqps/eogtrain.nsf/b81bacb527b016d785256e4a004c0393/d4ec501f07c0e03a85256b6c006caf64/\\$FILE/si412c\\_lesson9.pdf](http://yosemite.epa.gov/oaqps/eogtrain.nsf/b81bacb527b016d785256e4a004c0393/d4ec501f07c0e03a85256b6c006caf64/$FILE/si412c_lesson9.pdf).
- (118) Scala, F.; Chirone, R.; Meloni, P.; Carcangiu, G.; Manca, M.; Mulas, G.; Mulas, A. Fluidized Bed Desulfurization Using Lime Obtained after Slow Calcination of Limestone Particles. *Fuel* **2013**, *114*, 99–105.

- (119) Borgwardt, R. H. Calcium Oxide Sintering in Atmospheres Containing Water and Carbon Dioxide. *Ind. Eng. Chem. Res.* **1989**, *28*, 493–500.
- (120) Borgwardt, R. H. Effect of Specific Surface Area on the Reactivity of CaO with SO<sub>2</sub>. *AIChE J.* **1986**, *32*, 239–246.
- (121) Marier, P.; Dibbs, H. P. The Catalytic Conversion of SO<sub>2</sub> to SO<sub>3</sub> by Fly Ash and the Capture of SO<sub>2</sub> and SO<sub>3</sub> by CaO and MgO. *Thermochim. Acta* **1974**, *8*, 155–165.
- (122) Jozewicz, W.; Kirchgessner, D. A.; Division, E. S.; Corporation, A.; Engineering, E.; Environmental, U. S.; Agency, P. Calcination of Calcium Hydroxide Sorbent in the Presence of SO and Its Effect on Reactivity. **1991**.
- (123) Adanez, J.; Fierro, V.; García-Labiano, F.; Palacios, J. Study of Modified Calcium Hydroxides for Enhancing SO<sub>2</sub> Removal during Sorbent Injection in Pulverized Coal Boilers. *Fuel* **1997**, *76*, 257–265.
- (124) Mai, M. C.; Edgar, T. F. Surface Area Evolution of Calcium Hydroxide during Calcination and Sintering. *AIChE J.* **1989**, *35*, 30–36.
- (125) Silcox, G. D.; Kramlich, J. C.; Pershing, D. W. A Mathematical Model for the Flash Calcination of Dispersed Calcium Carbonate and Calcium Hydroxide Particles. *Ind. Eng. Chem. Res.* **1989**, *28*, 155–160.
- (126) Lee, K. S.; Jung, J. H.; Keel, S. I.; Yun, J. H.; Min, T. J.; Kim, S. S. Characterization of Calcium Carbonate Sorbent Particle in Furnace Environment. *Sci. Total Environ.* **2012**, *429*, 266–271.
- (127) Al Nasser, W. N.; Al Salhi, F. H. Scaling and Aggregation Kinetics Determination of Calcium Carbonate Using Inline Technique. *Chem. Eng. Sci.* **2013**, *86*, 70–77.
- (128) Mahuli, S.; Agnihotri, R. Pore-structure Optimization of Calcium Carbonate for Enhanced Sulfation. *AIChE ...* **1997**, *43*, 2323–2335.
- (129) Ghosh-Dastidar, A. Investigation of High-Reactivity Calcium Carbonate Sorbent for Enhanced SO<sub>2</sub> Capture. *Ind. ...* **1996**, 598–606.
- (130) Pilat, M. J.; Wilder, J. M. Pilot Scale SO<sub>2</sub> Control by Dry Sodium Bicarbonate Injection and an Electrostatic Precipitator. *Environ. Prog.* **2007**, *26*, 263–270.
- (131) Heda, P. K.; Dollimore, D.; Alexander, K. S.; Chen, D.; Law, E.; Bicknell, P. A Method of Assessing Solid State Reactivity Illustrated by Thermal Decomposition Experiments on Sodium Bicarbonate. *Thermochim. Acta* **1995**, *255*, 255–272.
- (132) Raclavska, H.; Matysek, D.; Raclavsky, K.; Juchelkova, D. Geochemistry of Fly Ash from Desulphurisation Process Performed by Sodium Bicarbonate. *Fuel Process. Technol.* **2010**, *91*, 150–157.

- (133) Kuu, W.-Y.; Chilamkurti, R.; Chen, C. Effect of Relative Humidity and Temperature on Moisture Sorption and Stability of Sodium Bicarbonate Powder. *Int. J. Pharm.* **1998**, *166*, 167–175.
- (134) Yang, J.; Shih, S.; Lin, P. Effect of Carbon Dioxide on the Sulfation of High Surface Area CaCO<sub>3</sub> at High Temperatures. *Ind. Eng. Chem. ...* **2012**.
- (135) Yang, J.-H.; Shih, S.-M.; Wu, C.-I.; Tai, C. Y.-D. Preparation of High Surface Area CaCO<sub>3</sub> for SO<sub>2</sub> Removal by Absorption of CO<sub>2</sub> in Aqueous Suspensions of Ca(OH)<sub>2</sub>. *Powder Technol.* **2010**, *202*, 101–110.
- (136) Manovic, V.; Anthony, E. J. Sequential SO<sub>2</sub>/CO<sub>2</sub> Capture Enhanced by Steam Reactivation of a CaO-Based Sorbent. *Fuel* **2008**, *87*, 1564–1573.
- (137) Desulfurization, F. G.; Removal, A. G. Lesson 9.
- (138) Cho, K. J.; Keener, T. C.; Khang, S.-J. A Study on the Conversion of Trona to Sodium Bicarbonate. *Powder Technol.* **2008**, *184*, 58–63.
- (139) Ho, C. S.; Shih, S. M. Calcium Hydroxide/fly Ash Sorbents for Sulfur Dioxide Removal. *Ind. Eng. Chem. Res.* **1992**, *31*, 1130–1135.
- (140) Milne, C. R.; Silcox, G. D.; Pershing, D. W.; Kirchgessner, D. A. High-Temperature, Short-Time Sulfation of Calcium-Based Sorbents. 1. Theoretical Sulfation Model. *Ind. Eng. Chem. Res.* **1990**, *29*, 2192–2201.
- (141) Güldür, Ç.; Doğu, G.; Doğu, T. Kinetics of Trona Sulfur Dioxide Reaction. *Chem. Eng. Process. ...* **2001**, *40*, 13–18.
- (142) Bryden, K. W.; Ragland, K. M. *Combustion Engineering*; Second Edi.; CRC Press: New York, 2011; pp. 108–115.
- (143) Hunt, T.; Hanley, J. T. *Integrated Dry NO<sub>x</sub>/SO<sub>2</sub> Emissions Control System Final Report, Volume 2: Project Performance and Economics*; Denver, 1999.
- (144) Borgwardt, R. H. Calcination Kinetics and Surface Area of Dispersed Limestone Particles. *AIChE J.* **1985**, *31*, 103–111.
- (145) Ar, İ.; Doğu, G. Calcination Kinetics of High Purity Limestones. *Chem. Eng. J.* **2001**, *83*, 131–137.
- (146) Yan, C.-F.; Grace, J. R.; Lim, C. J. Effects of Rapid Calcination on Properties of Calcium-Based Sorbents. *Fuel Process. Technol.* **2010**, *91*, 1678–1686.
- (147) Hsia, C.; St. Pierre, G. R.; Raghunathan, K.; Fan, L.-S. Diffusion through CaSO<sub>4</sub> Formed during the Reaction of CaO with SO<sub>2</sub> and O<sub>2</sub>. *AIChE J.* **1993**, *39*, 698–700.

- (148) Hsia, C.; Pierre, G.; Fan, L. Isotope Study on Diffusion in CaSO<sub>4</sub> Formed during Sorbent-flue-gas Reaction. *AIChE J.* **1995**, *41*, 2337–2340.
- (149) Yagi, S.; Kunii, D. Studies on Combustion of Carbon Particals in Flames and Fluidized Beds. In *Proceedings 5th Int. Symp. on Combustion*; 1955.
- (150) Szekely, J.; Evans, J. M.; Sohn, H. Y. *Gas-Solid Reactions*; Academic Press: New York, 1976.
- (151) Szekely, J.; Evans, J. W. A Structural Model for Gas—solid Reactions with a Moving Boundary. *Chem. Eng. Sci.* **1970**, *25*, 1091–1107.
- (152) Hartman, M.; Coughlin, R. Reaction of Sulfur Dioxide with Limestone and the Influence of Pore Structure. *Ind. Eng. Chem. ...* **1974**, *13*, 2–7.
- (153) Hartman, M.; Coughlin, R. Reaction of Sulfur Dioxide with Limestone and the Grain Model. *AIChE J.* **1976**.
- (154) Ramachandran, P. A.; Smith, J. M. A Single-Pore Model for Gas-Solid Noncatalytic Reactions. *AIChE J.* **1977**, *23*, 353.
- (155) EIA. *Annual Coal Report*; 2013.
- (156) DiPietro, P.; Krulla, K. *Improving the Efficiency of Coal-Fired Power Plants for Near Term Greenhouse Gas Emissions Reductions*; 2010.
- (157) Dubanowitz, A, J. Design of a Materials Recovery Facility (MRF) For Processing the Recyclable Materials of New York City’s Municipal Solid Waste, Columbia University, 2000.
- (158) *NEW COAL-FIRED POWER PLANT PERFORMANCE AND COST ESTIMATES*; 2009.
- (159) Dubanowitz, A, J. Design of a Materials Recovery Facility (MRF) For Processing the Recyclable Materials of New York City’s Municipal Solid Waste, Columbia University, 2000.
- (160) Landfill tipping fees in USA <http://www.cleanenergyprojects.com/Landfill-Tipping-Fees-in-USA-2013.html>.
- (161) Kessler Consulting Inc. *Materials Recovery Facility Feasibility Study*; 2009.
- (162) Center for climate and energy solutions. *Options and Considerations for a Federal Carbon Tax*; 2013.
- (163) Mettler, M. S.; Paulsen, A. D.; Vlachos, D. G.; Dauenhauer, P. J. The Chain Length Effect in Pyrolysis: Bridging the Gap between Glucose and Cellulose. *Green Chem.* **2012**, *14*, 1284.

- (164) Mettler, M. S.; Mushrif, S. H.; Paulsen, A. D.; Javadekar, A. D.; Vlachos, D. G.; Dauenhauer, P. J. Revealing Pyrolysis Chemistry for Biofuels Production: Conversion of Cellulose to Furans and Small Oxygenates. *Energy Environ. Sci.* **2012**, *5*, 5414.
- (165) Paulsen, A.; Mettler, M.; Dauenhauer, P. The Role of Sample Dimension and Temperature in Cellulose Pyrolysis. *Energy & Fuels* **2013**, *27*, 2126–2134.
- (166) Mettler, M. S.; Paulsen, A. D.; Vlachos, D. G.; Dauenhauer, P. J. Pyrolytic Conversion of Cellulose to Fuels: Levoglucosan Deoxygenation via Elimination and Cyclization within Molten Biomass. *Energy Environ. Sci.* **2012**, *5*, 7864.
- (167) Mettler, M. S.; Paulsen, A. D.; Vlachos, D. G.; Dauenhauer, P. J. Tuning Cellulose Pyrolysis Chemistry: Selective Decarbonylation via Catalyst-Impregnated Pyrolysis. *Catal. Sci. Technol.* **2014**.
- (168) Bryers, R. Fireside Slagging, Fouling, and High-Temperature Corrosion of Heat-Transfer Surface due to Impurities in Steam-Raising Fuels. *Prog. energy Combust. Sci.* **1996**, *72*.
- (169) Degereji, M. U.; Gubba, S. R.; Ingham, D. B.; Ma, L.; Pourkashanian, M.; Williams, a.; Williamson, J. Predicting the Slagging Potential of Co-Fired Coal with Sewage Sludge and Wood Biomass. *Fuel* **2013**, *108*, 550–556.
- (170) Van Dyk, J. C.; Melzer, S.; Sobiecki, a. Mineral Matter Transformation during Sasol-Lurgi Fixed Bed Dry Bottom Gasification – Utilization of HT-XRD and FactSage Modelling. *Miner. Eng.* **2006**, *19*, 1126–1135.
- (171) Teixeira, P.; Lopes, H.; Gulyurtlu, I.; Lapa, N.; Abelha, P.; Ed, J. Slagging and Fouling during Coal and Biomass Cofiring: Chemical Equilibrium Model Applied to FBC. **2014**.
- (172) Elliott, D. C.; Baker, E. G. The Effect of Catalysis on Wood-Gasification Tar Composition. *Biomass* **1986**, *9*, 195–203.
- (173) Shenqi, X.; Zhijie, Z.; Jie, X.; Guangsuo, Y.; Fuchen, W. Effects of Alkaline Metal on Coal Gasification at Pyrolysis and Gasification Phases. *Fuel* **2011**, *90*, 1723–1730.
- (174) Sheth, A.; Yeboah, Y. D.; Godavarty, A.; Xu, Y.; Agrawal, P. K. Catalytic Gasification of Coal Using Eutectic Salts: Reaction Kinetics with Binary and Ternary Eutectic Catalysts. *Fuel* **2003**, *82*, 305–317.
- (175) Devi, L.; Ptasinski, K. J.; Janssen, F. J. J. G. A Review of the Primary Measures for Tar Elimination in Biomass Gasification Processes. **2003**, *24*, 125–140.
- (176) Grubor, B.; Manovic, V.; Oka, S. An Experimental and Modeling Study of the Contribution of Coal Ash to SO<sub>2</sub> Capture in Fluidized Bed Combustion. *Chem. Eng. J.* **2003**, *96*, 157–169.

- (177) Garea, A.; Herrera, J. Thermogravimetric Determination of the Influence of Water Vapour in the FGD In-duct Injection at Low Temperatures. *J. Chem. ...* **2000**, 490.
- (178) Badin, E. J.; Frazier, G. C. Sorbents for Fluidized-Bed Combustion. *Environ. Sci. Technol.* **1985**, 19, 894–901.
- (179) Adanez, J.; García-Labiano, F.; Fierro, V. Modelling for the High-Temperature Sulphation of Calcium-Based Sorbents with Cylindrical and Plate-like Pore Geometries. *Chem. Eng. Sci.* **2000**, 55, 3665–3683.
- (180) Garea, A.; Marques, J. A.; Irabien, A. Mechanistical and Non-Linear Modelling Approaches to in-Duct Desulfurization. *Chem. Eng. Process. Process Intensif.* **2005**, 44, 709–715.